3-22-2019

Multi-Sensor Data Fusion between Radio Tomographic Imaging and Noise Radar

Christopher Vergara

MULTI-SENSOR DATA FUSION BETWEEN RADIO TOMOGRAPHIC IMAGING AND NOISE RADAR

THESIS

Christopher Vergara, FLTLT, RAAF

AFIT-ENG-MS-19-M-064

DEPARTMENT OF THE AIR FORCE
AIR UNIVERSITY

AIR FORCE INSTITUTE OF TECHNOLOGY

Wright-Patterson Air Force Base, Ohio

AFIT-ENG-MS-19-M-064

MULTI-SENSOR DATA FUSION BETWEEN RADIO TOMOGRAPHIC IMAGING AND NOISE RADAR

THESIS

Presented to the Faculty

Department of Electrical and Computer Engineering

Graduate School of Engineering and Management

Air Force Institute of Technology

Air University

Air Education and Training Command

in Partial Fulfillment of the Requirements for the

Degree of Master of Science in Electrical Engineering

Christopher Vergara, B.S.E.E.

FLTLT, RAAF

March 21, 2019

AFIT-ENG-MS-19-M-064

MULTI-SENSOR DATA FUSION BETWEEN

RADIO TOMOGRAPHIC IMAGING AND NOISE RADAR

THESIS

Christopher Vergara, B.S.E.E.
FLTLT, RAAF

Committee Membership:

Dr. R. K. Martin
Chair

Dr. P. J. Collins
Member

Maj J. R. Lievsay, PhD
Member

Abstract

The lack of situational awareness within an operational environment is a problem that carries high risk and expensive consequences. Radio Tomographic Imaging (RTI) and noise radar are two proven technologies capable of through-wall imaging and foliage penetration. The intent of this thesis is to provide a proof of concept for the fusion of data from RTI and noise radar. The output of this thesis will consist of a performance comparison between the two technologies followed by the derivation of a fusion technique to produce a single image.

Proposals have been made for the integration of multiple-input multiple-output (MIMO) radar with RTI, however, no research has been done. Data fusion between RTI and noise radar has not been explored in academia. The impact of the expected results will provide the RTI and noise radar community a proof of concept for the fusion of data from two disparate sensor technologies. RTI is a tenured field of study at Air Force Institute of Technology (AFIT), whose results can be used to produce a platform for further options to be considered for military surveillance applications.

The novelty of fusing data from RTI and noise radar is achieved with the derivation of a fusion technique utilizing Tikhonov regularization. Analyzing the results of the Tikhonov influenced techniques reveals up to a 100% error decrease in target pixel location, a 75% error decrease in target centroid location, a 28% size decrease in target pixel dispersion and a 72% improvement in an ideal solution comparison. The results of the research prove that Multi-Sensor Data Fusion (MSDF) images are of greater quality than that of the images generated by the disparate sensors independently. This effectively provides the RTI and noise radar communities a proof of concept for the fusion of data from two disparate sensor technologies.

Acknowledgements

You get one opportunity. You balls it up and you are in strife.

To the students and interns in the Radar Instrumentation Laboratory (RAIL), your advice, assistance and ability to have a chin wag in the arvo will not be forgotten. Many thanks to my committee members for their availability and guidance. To the International Military Student Officer (IMSO), the students of 19M and the staff of AFIT, thank you for making my time here in the United States of America a memorable one. Cheers!

Christopher Vergara

Table of Contents

List of Figures

List of Tables

List of Abbreviations

ADF Australian Defence Force

AFIT Air Force Institute of Technology

ALPINE Air Force Institute of Technology Low Observables Radar Electromagnetics Processing INtegrated Environment

AWGN additive white Gaussian noise

dB decibels

CRLB Cramer-Rao Lower Bound

DFL device-free localization

EKF extended Kalman Filter

FLAC fuzzy logic adaptive controller

GPS Global Positioning System

GUI Graphical User Interface

IEEE Institute of Electrical and Electronics Engineers

IFA Inverted F Antenna

IMSO International Military Student Officer

INS Inertial Navigation System

ISM Industrial, Scientific and Medical

ISR intelligence, surveillance and reconnaissance

LOS line-of-sight

LPA log-periodic antenna

MAP maximum a posteriori

MHz megahertz

MIMO multiple-input multiple-output

ML maximum likelihood

MSDF Multi-Sensor Data Fusion

MSE mean squared error

MTT multiple target tracking

NaN not a number

NoNET Noise Network

NR1 Noise Radar 1

NR2 Noise Radar 2

NR3 Noise Radar 3

NRN Noise Radar Network

OS operating system

PSD power spectral density

PVC Polyvinyl Chloride

RAAF Royal Australian Air Force

RAIL Radar Instrumentation Laboratory

RAM random access memory

RF radio frequency

RMSE root-mean-square error

RSS received signal strength

RTI Radio Tomographic Imaging

SNR signal to noise ratio

SPAN Sensing and Processing Across Networks

UKF unscented Kalman Filter

USA United States of America

USB universal serial bus

UWB Ultra-wideband

VRTI Variance-based Radio Tomographic Imaging

WSN wireless sensor network

WSS wide-sense stationary

2D two-dimensional

3D three-dimensional

List of Symbols

Symbol		Page
$y_i(t)$	Received signal strength of link i at time t	12
P_i	Transmitted power in dB	12
L_i	Static losses in dB due to distance, antenna patterns, device inconsistencies, etc	12
$S_i(t)$	Shadowing loss in dB due to object/s attenuating the signal link	12
$F_i(t)$	Fading loss in dB as a result of constructive and deconstructive interference of the narrow-band signals in multipath environments	12
$v_i(t)$	Measurement noise in dB	12
N	Number of pixels	12
$x_j(t)$	The attenuation occurring in pixel j at time t	12
w_{ij}	The weighting of pixel j (of the reconstructed image) for link i	13
Δy_i	A change in RSS	13
M	The total number of unique two-way links	14
$\mathbf{n}$	RTI noise vector	14
$\mathbf{x}$	A vector of length M of all link difference RSS measurements	14
$\mathbf{y}$	Link received signal strength (RSS) difference measurements	14
$\mathbf{W}$	The Weighting Matrix	14
$\mathbf{S}$	A binary selection matrix	14
$\mathbf{\Omega}$	A real-valued matrix containing the magnitude of the weights	14
$\odot$	Hadamard operation	14

λ	A tunable parameter describing the width of the ellipse	15
$f_{n_i}(u)$	The probability density function of the noise random variable n_i	16
$\mathbf{Q}$	Tikhonov matrix	17
α	Tikhonov weight parameter	17
$\mathbf{F}_k$	The state transition model	23
$\mathbf{B}_k$	The control input model	23
$\mathbf{w}_k$	The process noise assumed to be drawn from a zero mean multivariate normal distribution with covariance $\mathbf{Q}_k$	24
$\mathbf{Q}_k$	Covariance of the process noise $\mathbf{w}_k$	24
$\mathbf{z}_k$	Observation	24
$\mathbf{H}_k$	The observation model	24
$\mathbf{v}_k$	The observation noise assumed to be zero mean Gaussian white noise with covariance $\mathbf{R}_k$	24
$\hat{\mathbf{x}}_k^-$	The *a priori* state prediction	25
$\mathbf{P}_k^-$	The *a priori* predicted error covariance	25
$\hat{\mathbf{x}}_k$	The *a posteriori* state estimate	25
$\mathbf{K}_k$	Kalman gain	25
$\mathbf{P}_k$	The *a posteriori* error covariance matrix	25
$\mathbf{x}_{\mathrm{NR}z}$	The $N \times 1$ reflection image to be estimated with N pixels from the zth NRN node	28
$\mathbf{y}_{\mathrm{NR}z}$	The $I \times 1$ vector of magnitudes in the impulse response/cross correlation magnitudes at I calibrated ranges from the zth NRN node	28
$\mathbf{W}_{\mathrm{NR}z}$	The weighting matrix with each column representing a single pixel and each row describing the weighting of each pixel for a particular range	28
$\mathbf{n}_{\mathrm{NR}z}$	The noise vector of the zth NRN node	29

x_j	The x coordinate of the jth pixel	29
h	The x coordinate of the AFIT NoNET node	30
y_j	The y coordinate of the jth pixel	30
k	The y coordinate of the AFIT NoNET node	30
$r_{\text{inner},i}$	The inner radius of the range ring	30
$r_{\text{outer},i}$	The outer radius of the range ring	30
$\mathbf{y}_{\text{RTI}}$	The calibrated RSS values from all M links in the RTI network	30
$\mathbf{y}_{\text{NRN}}$	The stacked calibrated impulse response/cross correlation magnitudes from each NRN node	31
$\mathbf{x}_{\text{FUS}}$	The fusion image of the RTI and the AFIT NoNET sensors	31
$\hat{\mathbf{x}}_{\text{KAL}}$	The RTI attenuation image using the maximum likelihood (ML) estimate with Tikhonov regularization	81
β_{RTI}	Tunable parameter to increase the influence of the RTI sensor technology in MSDF	89

MULTI-SENSOR DATA FUSION BETWEEN

RADIO TOMOGRAPHIC IMAGING AND NOISE RADAR

I. Introduction

This chapter establishes the scope of the thesis. A background is provided for the two sensor technologies involved, namely, Radio Tomographic Imaging (RTI) and noise radar, including a description of the equipment used in their construct. Motivation behind this thesis topic is reasoned, producing a final research problem statement. To finish the introduction, a mention of how the thesis document is organized is laid out.

1.1 Background

1.1.1 Radio Tomographic Imaging.

RTI is a technology that is used for imaging the attenuation created by physical objects within a radio frequency (RF) wireless sensor network (WSN). RTI has been classified as a device-free localization (DFL) system [1–3], which finds people and objects in the environment wherein the WSN is deployed, even in buildings and through walls [3]. A DFL system does not require the person or physical object to carry a wireless device, opening RTI technology to the world of security and monitoring applications.

The RTI WSN consists of a number of RF transceivers, labeled as network nodes, communicating the received signal strength (RSS) to and from every other node in the network, see Figure 1.1. When a person or physical object intersects the communication links of Figure 1.1, the reported RSS values of the affected nodes to which the intersected communication links belong to are usually, if not always, altered. The re-

porting of altered RSS values provides information that is used to detect the presence of and to estimate the location of the subject or subjects of interest.

1.1.1.1 Equipment.

Table 1.1 lists and describes the core equipment used for RTI in this thesis. Figure 1.2 displays the MEMSIC TelosB Mote TPR2420 and its functional block diagram.

1.1.2 Noise Radar.

A noise radar is a technology that uses a noise waveform as its transmitting signal. The echo detection is achieved via the reception and correlation between the transmitted signal and the received noise waveform that the radar returns. A simple simulation of the noise correlation result is shown in Figure 1.3. Noise radar differs from RTI in the sense that it does not use shadowing caused by objects, but rather, uses reflections as a basis for image reconstruction.

Categorically speaking, the noise radar for this thesis is classified as an Ultra-wideband (UWB) system. In the United States of America (USA), UWB refers to a signal or system that either has a large relative bandwidth that exceeds 20% of the arithmetic center frequency, or a large absolute bandwidth of more than 500 megahertz (MHz) [4]. The potential advantages of using UWB radars include improved range resolution, easier target information recovery from reflected signals and a lower probability of intercept compared to radars operating with narrowband signals [5, 6].

1.1.2.1 Equipment.

Table 1.2 lists and describes the core equipment used for the UWB noise radar in this thesis. Configured together, the equipment in Table 1.2 is known as an Air Force Institute of Technology (AFIT) Noise Network (NoNET) node. Figure 1.4 displays an

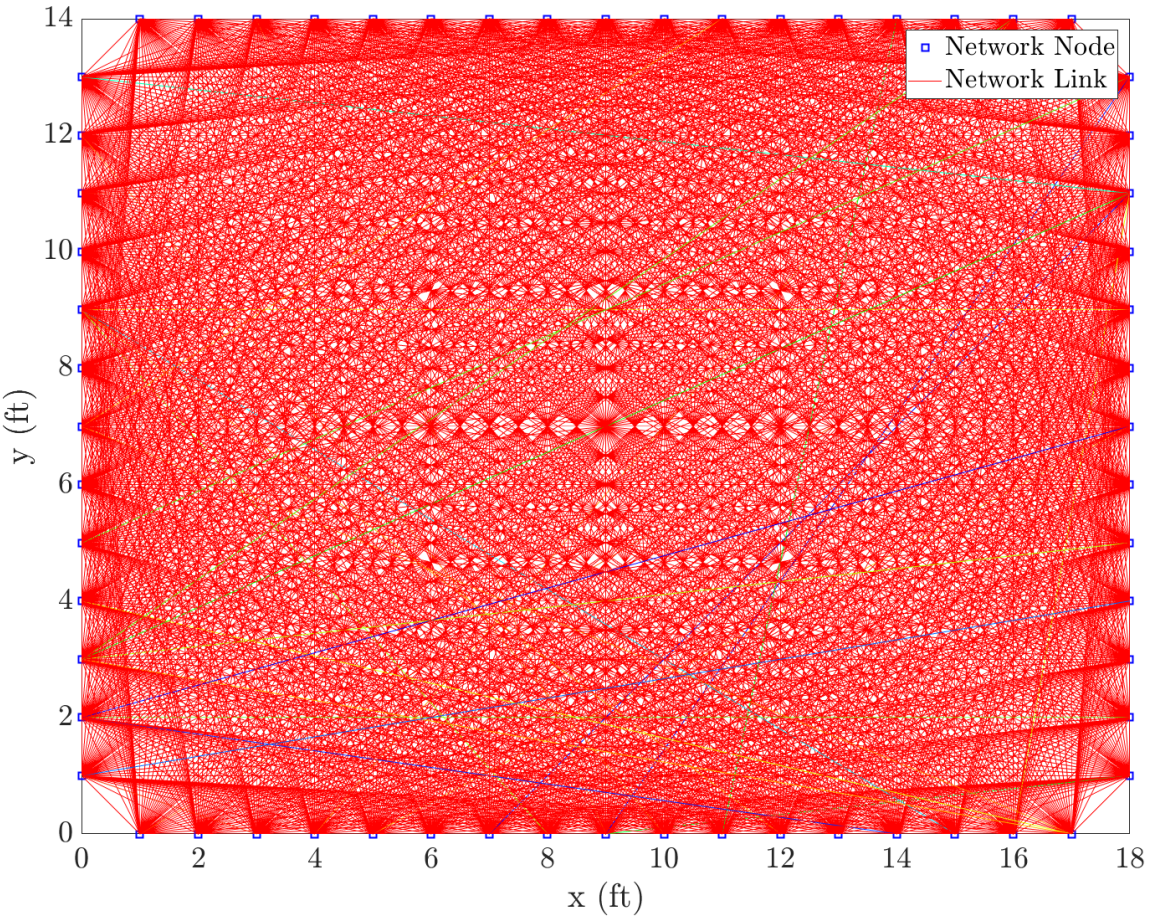

Figure 1.1. A RTI WSN with 70 nodes and their RF communication links.

AFIT NoNET node and its functional block diagram.

1.2 Motivation for Research

The lack of situational understanding within an operational environment is a problem that carries high risk and expensive consequences. In accordance with Royal Australian Air Force (RAAF) doctrine, the fundamental principles by which military forces guide their actions to achieve desired objectives, situational understanding is the awareness, analysis, knowledge, comprehension and judgment facilitating and enabling timely and accurate decision-making. The accurate interpretation of a situation and the likely

Table 1.1. Core RTI equipment.

Nomenclature	Description
MEMSIC TelosB Mote TPR2420	RTI WSN node with an integrated onboard antenna, providing data collection and programming via a universal serial bus (USB) interface using the open-source operating system, TinyOS.
Computer	Programs, collects and processes the data from the motes set up for the RTI WSN. Running on an Intel® Core© i7 2.80 GHz processor with 8 GB of random access memory (RAM) with Microsoft Windows® 7 64 bit operating system (OS).

Table 1.2. Core UWB noise radar equipment.

Nomenclature	Description
UWB noise radar	An AFIT built UWB noise radar comprising of transmit and receive antennas, a noise source, band pass filters, switches, amplifiers and attenuators.
Computer	Controls, collects and processes the data from the UWB noise radar. Running on an Intel® Core© i7 2.70 GHz processor with 32 GB of RAM with Microsoft Windows® 10 64 bit OS.

actions of groups and individuals within it is an Australian Defence Force (ADF) warfighting function to the RAAF's core air power role of intelligence, surveillance and reconnaissance (ISR) (Figure 1.5).

RTI and UWB noise radar are two proven technologies capable of through-wall imaging and foliage penetration enabling increased situational understanding [3, 6–8]. The results of this research can be used to produce a platform for further options to be considered for military ISR applications.

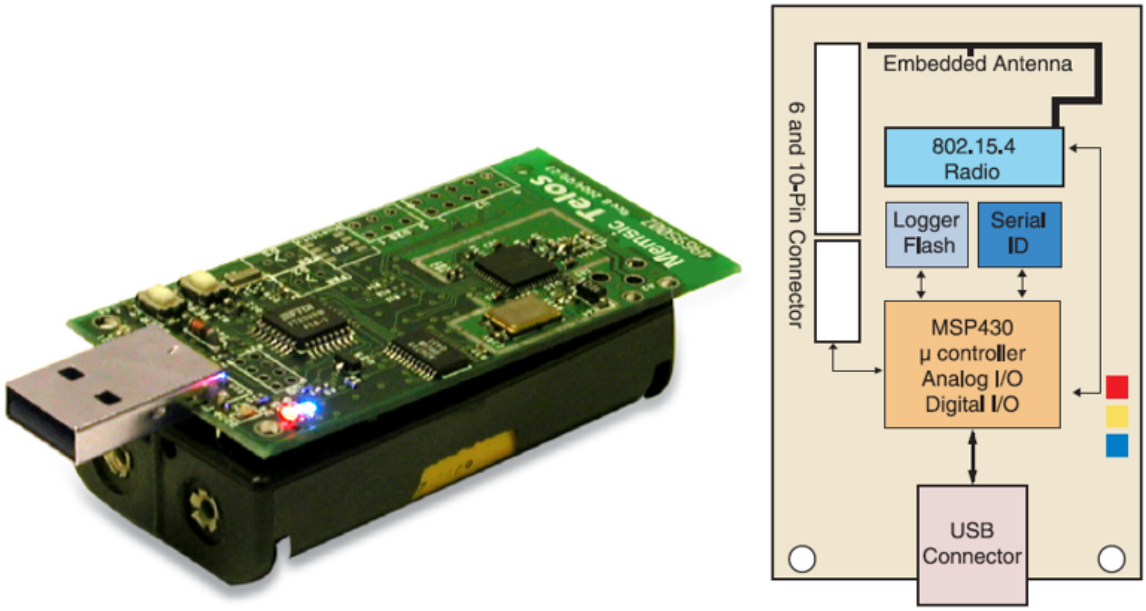

Figure 1.2. The MEMSIC TelosB Mote TPR2420 and its functional block diagram.

1.3 Research Problem Statement

Proposals have been made for the integration of multiple-input multiple-output (MIMO) radar with RTI [3], however, no research has been done. Data fusion between RTI and noise radar has not been explored in academia. The intent of this thesis is to provide a proof of concept for the fusion of data from RTI and UWB noise radar.

The nature of the expected results will be in the form of target location accuracy. Accuracy assessment of detection and estimation techniques shall be explored. This exploration involves a comparison of measured estimates of reconstructed images. Metrics on the measured estimates can outline the differences in performance and computational efficiencies of using RTI and UWB noise radar together versus using them separately.

The output of this thesis will consist of a performance comparison between the two technologies followed by the derivation of a fusion technique to produce a single image. The impact of the expected results will provide the RTI and noise radar community

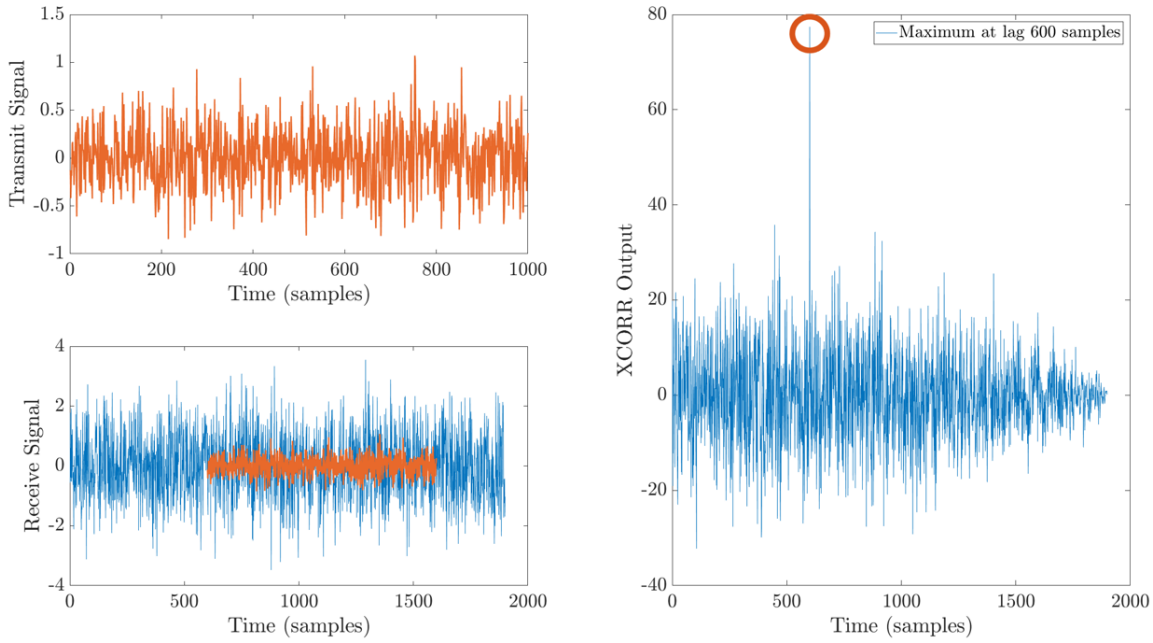

Figure 1.3. A simple simulation of the noise correlation process. Top left: Transmitted noise signal. Bottom left: Received noise signal with transmitted signal embedded in noise. Right: Correlation output between the transmitted and received signal, correctly identifying a lag of 600 samples.

a proof of concept for the fusion of data from two disparate sensor technologies.

1.4 Thesis Document Organization

This document is constructed according to a five-chapter model. Chapter I has set the scope of this thesis providing a background, motivation and problem statement involving RTI and UWB noise radar. The remainder of this document includes Chapters II through V and is organized as follows.

Chapter II contains a literature review of the academic work involving RTI target detection and location. The same follows for UWB noise radar. Chapter III details the steps taken towards addressing the problem statement involving the data fusion between two disparate sensor technologies, RTI and UWB noise radar. Chapter IV presents, analyzes and discusses the results of the data fusion following the methodology of Chapter III. Finally Chapter V draws conclusions from the discussion of the

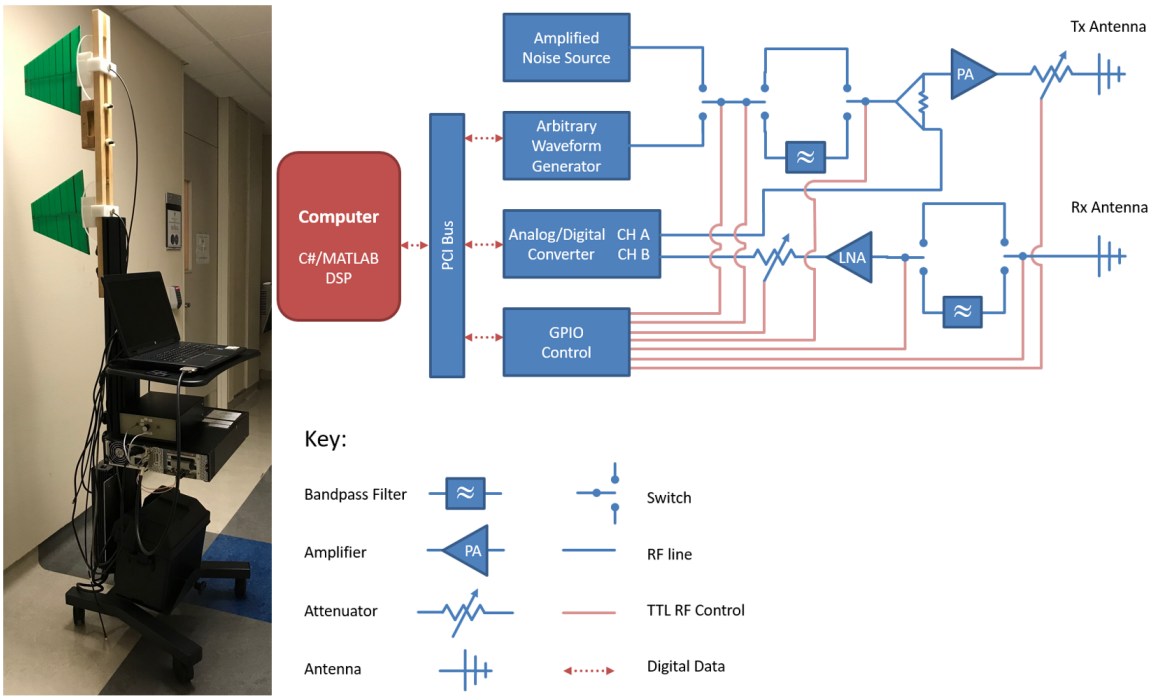

Figure 1.4. An AFIT NoNET node and its functional block diagram. (Current as of: January 2019)

data fusion results and proposes further related work that can be used to continue the research presented in this thesis.

Air Power Roles		ADF Warfighting Functions
Core	Control of the Air	Force Application
	Strike	
	Air Mobility	Force Projection
	ISR	Situational Understanding

Figure 1.5. Core air power roles and ADF warfighting functions.

II. Related Work

This chapter probes relevant academic literature that ties into the premise of Multi-Sensor Data Fusion (MSDF) of Radio Tomographic Imaging (RTI) and a Noise Radar Network (NRN). The fundamental theory of each sensor technology is explored as well as any work conducted with them within the Air Force Institute of Technology (AFIT). The chapter ends with a possible avenue for MSDF, exploring a well known method of sensor fusion, namely, the Kalman filter.

2.1 Radio Tomographic Imaging

The article in [9] created a momentum of research surrounding real world applications of RTI. Reference [9] laid the foundational theory and presented the linear model for using received signal strength (RSS) measurements for image reconstruction of an area within a wireless sensor network (WSN). As multi-sensor data fusion depends on the sensor error and noise statistics, we shall explore literature relating to this.

Reference [9] derives a lower bound on the estimation error for the linear and noise models. The theoretical lower bound is obtained through the use of a Fisher information matrix that contains information obtained from RSS data measurements of each node in the RTI WSN.

It is determined that node locations affect which pixels are accurately estimated. More precisely, it is shown in [9] that pixels which are crossed by many links are more likely to have a higher accuracy than those that are rarely or are never crossed. In addition to node location affecting accuracy, [9] demonstrates a relationship between node density and the lower bound on the average mean squared error (MSE). Also, the choice of RTI parameters

- Regularization parameter α

- Ellipse parameter λ,

affect image accuracy [3, 9]. If the regularization parameter, α, is set too high, the resultant images are too smooth to provide definitive obstruction boundaries. However, if α is set too low, noise corrupts the image, making it more difficult to set a detection threshold. If the width of the ellipse, λ, is too wide, detail of where the attenuation is occurring will be obscured. If λ is set too narrow, pixels that do in fact attenuate a link's signal may not be captured by the model resulting in lost information.

In an attempt to resolve this balancing act, [9] provides graphs depicting average MSE using combinations of regularization and ellipse parameters. Also, research in [10] provides a method of theoretically deriving a value for α. This works on the premise that regularization is known as being equivalent to assuming a Bayesian prior on the RSS measurements, $\mathbf{x}$. Thus, given a Bayesian prior $f(\mathbf{x})$, a maximum a posteriori (MAP) estimate can be computed. This is followed by further derivations leading to a theoretical equation for the regularization parameter [10]

$$\alpha = \frac{\sigma_n^2}{\sigma_x^2} \cdot \frac{1}{1-c^2} \approx \frac{\sigma_n^2}{\sigma_x^2} \frac{\delta_c}{2\delta}, \tag{2.1}$$

where σ_x^2/σ_n^2 is a signal to noise ratio (SNR), δ_c/δ is the number of pixels of separation required for 63% decorrelation and $c = e^{-\delta/\delta_c}$.

Work in [11] provides an analytic expression for the image accuracy for five RTI weight models. The derivation shows the effect of weight model choice, pixel size, number of nodes and choice of regularization α. Comparison between weight model choice was achieved via various forms of normalization and was necessary as the original forms would have produced scene estimates orders of magnitude different from each other.

References [9, 11] model the noise, $\mathbf{n}$, as Gaussian, with [11] settling for an additive white Gaussian noise (AWGN) error model with standard deviation, σ_n between 4 dB

and 6 dB. The decision to use the Cramer-Rao Lower Bound (CRLB) to analyze the variance of RTI in [11] was reasonable because for a linear model with AWGN (which RTI is), the variance of the maximum likelihood (ML) estimate equals the CRLB.

The Kalman filter has been used in RTI work [3]. With respect to the observation equation, $\mathbf{z} = \mathbf{H}\mathbf{x} + \mathbf{v}$, the experiments in [3] assumed the measurement/observation noise, $\mathbf{v}$, as Gaussian and found that it was effective for tracking the location of movement with $\mathbf{H}$ being the observation model. In order to implement their Kalman filter, empirical observations were used, i.e. knowing the true path of the target, a "test and adjust" approach was taken to determine the process noise. Process noise is a parameter required when defining the true state $\mathbf{x}$. To quantify the accuracy of their location coordinate estimate, the average error was defined as

$$\epsilon = \frac{1}{L}\sum_{k=1}^{L}\sqrt{\big(u_x[k]-p_x[k]\big)^2+\big(u_y[k]-p_y[k]\big)^2}, \tag{2.2}$$

where L is the total number of samples, $u_x[k]$ and $u_y[k]$ are the estimated x and y coordinates at sample time k, and $p_x[k]$ and $p_y[k]$ are the known coordinates. Using (2.2), [3] concluded that their Variance-based Radio Tomographic Imaging (VRTI) configured setup could locate an object moving in place with approximately 1.5 ft average error.

We now begin an encapsulation of the theory heavily used in literature for the implementation of RTI.

2.1.1 Fundamental Theory.

2.1.1.1 Linear Formation.

The RSS, $y_i(t)$ of link i at time t is mathematically represented by

$$y_i(t) = P_i - L_i - S_i(t) - F_i(t) - v_i(t), \tag{2.3}$$

where

- P_i is the transmitted power in decibels (dB)
- L_i are the static losses in dB due to distance, antenna patterns, device inconsistencies, etc.
- $S_i(t)$ is the shadowing loss in dB due to object/s attenuating the signal link
- $F_i(t)$ is the fading loss in dB as a result of constructive and deconstructive interference of the narrow-band signals in multipath environments
- $v_i(t)$ is the measurement noise in dB.

A WSN is made up of N pixels. The number of pixels come into play when defining the shadowing loss, $S_i(t)$ mathematically. Qualitatively, the shadowing loss is approximated as the sum of attenuation that occurs in each pixel. However, since the contribution of all N pixels would be different for each link, weighting is applied. Quantitatively, shadowing loss described for link i is

$$S_i(t) = \sum_{j=1}^{N} w_{ij} x_j(t), \tag{2.4}$$

where

- $x_j(t)$ is the attenuation occurring in pixel j at time t

- w_{ij} is the weighting of pixel j (of the reconstructed image) for link i.

Simplification of image reconstruction is achieved by imaging the *changing* attenuation over time. This approach removes the static loss terms, P_i and L_i, in (2.3), resulting in a change in RSS Δy_i from time t_1 to t_2, i.e.

$$\begin{aligned}\Delta y_i &\equiv y_i(t_2) - y_i(t_1) \\ &= S_i(t_2) - S_i(t_1) + F_i(t_2) - F_i(t_1) + v_i(t_2) - v_i(t_1) \\ &= \sum_{j=1}^{N} w_{ij}\Delta x_j + n_i, \end{aligned} \tag{2.5}$$

where

$$n_i = F_i(t_2) - F_i(t_1) + v_i(t_2) - v_i(t_1)$$

is the grouping of fading and measurement noise and

$$\Delta x_j = x_j(t_2) - x_j(t_1)$$

is the difference in attenuation at pixel j from time t_1 to t_2.

The system of RSS equations in (2.5) put into a linear matrix form as

$$\Delta \mathbf{y} = \mathbf{W}\Delta \mathbf{x} + \mathbf{n}, \tag{2.6}$$

where

$$\Delta \mathbf{y} = [\Delta y_1, \Delta y_2, \ldots, \Delta y_M]^T$$
$$\Delta \mathbf{x} = [\Delta x_1, \Delta x_2, \ldots, \Delta x_N]^T$$
$$\mathbf{n} = [n_1, n_2, \cdots, n_M]^T$$
$$[\mathbf{W}]_{i,j} = w_{ij}. \tag{2.7}$$

To summarize (2.6), $\Delta \mathbf{y}$ is a vector of all link RSS difference measurements of length M, where M is the total number of unique two-way links, K, and is a function of the number of nodes used to create the WSN, i.e. $M = (K^2 - K)/2$. The RSS noise is captured in the vector, $\mathbf{n}$, and $\Delta \mathbf{x}$ is the attenuation image to be estimated. The weighting matrix, $\mathbf{W}$, is of dimension $M \times N$. Each variable is measured in dB. A majority of the literature simplify the notation of (2.6) and use $\mathbf{x}$ and $\mathbf{y}$ in place of $\Delta \mathbf{x}$ and $\Delta \mathbf{y}$, respectively.

2.1.1.2 Weight Models.

There have been a number of weight models that have been tried and tested within the literature. Reference [11] conveniently identifies five different published weight models, stating that in all cases, the weighting matrix $\mathbf{W}$ can be decomposed as

$$\mathbf{W} = \mathbf{S} \odot \mathbf{\Omega}, \tag{2.8}$$

where $\mathbf{S}$ is a binary selection matrix, $\mathbf{\Omega}$ is a real-valued matrix containing the magnitude of the weights and $\odot$ is the Hadamard product.

Binary selection matrices include

$$\mathbf{S}_{i,j}^{\text{Ellipse}} = \begin{cases} 1, & \text{if } d_{1,ij} + d_{2,ij} < d_i + \lambda \\ 0, & \text{otherwise} \end{cases} \tag{2.9}$$

$$\mathbf{S}_{i,j}^{\text{Line}} = \begin{cases} 1, & \text{if link } i \text{ traverses pixel } j \\ 0, & \text{otherwise} \end{cases} \tag{2.10}$$

$$\mathbf{S}_{i,j}^{\text{All}} = 1 \tag{2.11}$$

where d_i is the distance between two nodes, $d_{1,ij}$ and $d_{2,ij}$ are the distances from the center of pixel j to the two node locations for link i, and λ is a tunable parameter describing the width of the ellipse. Equation (2.9), suggested in [9] is the prevailing selection matrix throughout the literature.

As per [11], the magnitudes of the weights, $\mathbf{\Omega}$ include

$$\mathbf{\Omega}_{i,j}^{\text{NeSh}} = \frac{1}{\sqrt{d_i}} \tag{2.12}$$

$$\mathbf{\Omega}_{i,j}^{\text{Line}} = L_{i,j} \tag{2.13}$$

$$\mathbf{\Omega}_{i,j}^{\text{NeShLine}} = \frac{L_{i,j}}{\sqrt{d_i}} \tag{2.14}$$

$$\mathbf{\Omega}_{i,j}^{\text{Exp}} = \exp\left(\frac{-\lambda_{i,j}}{2\sigma_w}\right) \tag{2.15}$$

$$\mathbf{\Omega}_{i,j}^{\text{InvArea}} = \begin{cases} A^{-1}(d_i, \lambda_{min}), & \lambda_{i,j} < \lambda_{min} \\ A^{-1}(d_i, \lambda_{i,j}), & \lambda_{i,j} \geq \lambda_{min} \end{cases} \tag{2.16}$$

where $L_{i,j}$ is the length of the segment of link i inside pixel j, $\lambda_{i,j}$ is the value of λ that makes the ellipse defined by link i pass exactly through the center of pixel j, σ_w and λ_{min} are tunable parameters. Equation (2.12), suggested by [9] and justified by [12] is

the prevailing choice throughout the literature.

2.1.1.3 Noise Models.

Equation (2.6) would not be complete without determining the statistics of the noise vector **n**. Reference [9] finds that the RSS on a fixed link showed a two-part mixture distribution, attributing this to the time varying nature of RSS investigated in [13], categorized as being in either a fading or a non-fading interval. The literature shows that the noise vector could be modeled as a mixture of two Rician distributions in [13].

Reference [14] was used by [9] to suggest that the distribution could be log-normal, and this was the approach taken for the reason of simplicity. However, the model used by [9] for the noise vector **n** is a two part Gaussian mixture model

$$f_{n_i}(u) = \sum_{k\in\{1,2\}} \frac{p_k}{\sqrt{2\pi\sigma_k^2}} \exp\left[-\frac{u^2}{2\sigma_k^2}\right], \tag{2.17}$$

where p_k is the probability of part k, $p_2 = 1-p_1$, σ_k^2 is the variance of part k, and $f_{n_i}(u)$ is the probability density function of the noise random variable n_i. An assumption was made where $\sigma_2 > \sigma_1$ so that part 2 is the higher variance component of the mixture. Reference [11] models the noise, **n**, as Gaussian, which will be the model used for the work in this research.

2.1.2 Radio Tomographic Imaging Image Reconstruction.

Image reconstruction in RTI involves solving (2.6) for $\Delta\mathbf{x}$, i.e. $\mathbf{x}$. To minimize the noise vector, **n**, required to fit the measured RSS data, **y**, to the model, **Wx**, requires

searching for a least-squares solution

$$\begin{aligned}\mathbf{x}_{\mathrm{LS}} &= \arg\min_{\mathbf{x}} \|\mathbf{W}\mathbf{x}-\mathbf{y}\|_2^2 \\ &= (\mathbf{W}^T\mathbf{W})^{-1}\mathbf{W}^T\mathbf{y}. \end{aligned} \tag{2.18}$$

Equation (2.18) is only valid if $\mathbf{W}$ is full rank which is unfortunately not the case with RTI [11]. Labeled as an ill-posed inverse problem, this is addressed by [9] with additive Tikhonov regularization terms producing

$$\begin{aligned}\mathbf{x}_{\mathrm{LS}} &= \arg\min_{\mathbf{x}} \|\mathbf{W}\mathbf{x}-\mathbf{y}\|_2^2 + \alpha\mathbf{x}^T\mathbf{Q}\mathbf{x} \\ &= (\mathbf{W}^T\mathbf{W}+\alpha\mathbf{Q})^{-1}\mathbf{W}^T\mathbf{y} \end{aligned} \tag{2.19}$$

$$\mathbf{Q} \triangleq \mathbf{D}_{\boldsymbol{H}}^T\mathbf{D}_{\boldsymbol{H}} + \mathbf{D}_{\boldsymbol{V}}^T\mathbf{D}_{\boldsymbol{V}}, \tag{2.20}$$

where $\mathbf{Q}$ is the Tikhonov matrix, $\mathbf{D}_d$ computes the derivative in the d direction (i.e. Horizontal or Vertical) and α is an adjustable weight parameter where small values lead to solutions that favor the data and large values favor prior information.

A ML derivation is another method for arriving at (2.18), i.e.

$$\begin{aligned}\hat{\mathbf{x}}_{\mathrm{ML}}(\mathbf{y}) &= \arg\max_{\hat{\mathbf{x}}} \ln \wp(\mathbf{y}|\mathbf{x}) \\ &= \arg\max_{\hat{\mathbf{x}}} \mathscr{L}, \end{aligned} \tag{2.21}$$

where $\mathscr{L}$ is known as the log likelihood function. Assuming the noise vector $\mathbf{n} \sim \mathscr{N}(\mathbf{0}, \mathbf{C})$,

where $\mathbf{C} \approx \sigma^2\mathbf{I}$, therefore $\mathbf{y} \sim \mathcal{N}(\mathbf{Wx}, \sigma^2\mathbf{I})$. Hence,

$$\begin{aligned}
\mathscr{L} &= \ln\left[\left(\frac{1}{\sqrt{2\pi}^N|\mathbf{C}|}\right)\exp\left(-\frac{(\mathbf{y}-\mathbf{Wx})^T(\mathbf{C})^{-1}(\mathbf{y}-\mathbf{Wx})}{2}\right)\right] && (2.22)\\
&= -\mathrm{N}\ln\left(\sqrt{2\pi}\right) - \ln(|\mathbf{C}|) - \frac{1}{2}\left(\mathbf{y}-\mathbf{Wx}\right)^T(\mathbf{C})^{-1}\left(\mathbf{y}-\mathbf{Wx}\right)\\
&= -\mathrm{N}\ln\left(\sqrt{2\pi}\right) - \ln(|\mathbf{C}|) - \frac{1}{2}\left(\mathbf{y^T}-\mathbf{x^T}\mathbf{W^T}\right)\left(\sigma^2\mathbf{I}\right)^{-1}\left(\mathbf{y}-\mathbf{Wx}\right)\\
&= -\mathrm{N}\ln\left(\sqrt{2\pi}\right) - \ln(|\mathbf{C}|) - \frac{1}{2\sigma^2}\left(\mathbf{y^T}\mathbf{y}-\mathbf{y^T}\mathbf{Wx}-\mathbf{x^T}\mathbf{W^T}\mathbf{y}+\mathbf{x^T}\mathbf{W^T}\mathbf{Wx}\right)\\
&= -\mathrm{N}\ln\left(\sqrt{2\pi}\right) - \ln(|\mathbf{C}|) - \frac{1}{2\sigma^2}\left(\mathbf{y^T}\mathbf{y}-\left[\mathbf{y^T}\mathbf{Wx}\right]^\mathbf{T}-\mathbf{x^T}\mathbf{W^T}\mathbf{y}+\mathbf{x^T}\mathbf{W^T}\mathbf{Wx}\right)\\
&= -\mathrm{N}\ln\left(\sqrt{2\pi}\right) - \ln(|\mathbf{C}|) - \frac{1}{2\sigma^2}\left(\mathbf{y^T}\mathbf{y}-\mathbf{x^T}\mathbf{W^T}\mathbf{y}-\mathbf{x^T}\mathbf{W^T}\mathbf{y}+\mathbf{x^T}\mathbf{W^T}\mathbf{Wx}\right)\\
&= -\mathrm{N}\ln\left(\sqrt{2\pi}\right) - \ln(|\mathbf{C}|) - \frac{1}{2\sigma^2}\left(\mathbf{y^T}\mathbf{y}-\mathbf{2x^T}\mathbf{W^T}\mathbf{y}+\mathbf{x^T}\mathbf{W^T}\mathbf{Wx}\right) && (2.23)\\
&= -\mathrm{N}\ln\left(\sqrt{2\pi}\right) - \ln(|\mathbf{C}|) + f(\mathbf{x}). && (2.24)
\end{aligned}$$

Note that we want the arg max of $\mathscr{L}$, but due to the $-1/2\sigma^2$ term in (2.23), this implies that we should solve for $f(\mathbf{x})$ in (2.24).

$$\begin{aligned}
\arg\max_{\hat{\mathbf{x}}}\ \mathscr{L} = \nabla_{\mathbf{x}}\mathscr{L} \equiv \mathbf{0} && (2.25)\\
\mathbf{0}-\mathbf{0}-\frac{1}{2\sigma^2}\left(\mathbf{0}-\mathbf{2W^T}\mathbf{y}+\mathbf{2W^T}\mathbf{W}\hat{\mathbf{x}}\right) \equiv \mathbf{0} && (2.26)\\
\mathbf{W^T}\mathbf{y}-\mathbf{W^T}\mathbf{W}\hat{\mathbf{x}} \equiv \mathbf{0}\\
\mathbf{W^T}\mathbf{W}\hat{\mathbf{x}} \equiv \mathbf{W^T}\mathbf{y}\\
\hat{\mathbf{x}}(\mathbf{y}) = \left(\mathbf{W^T}\mathbf{W}\right)^{-\mathbf{1}}\mathbf{W^T}\mathbf{y}. && (2.27)
\end{aligned}$$

For (2.26), the following vector calculus identities were used,

$$\nabla_{\mathbf{x}}\left(\mathbf{V^T}\mathbf{x}\right) = \nabla_{\mathbf{x}}\left(\mathbf{x^T}\mathbf{V}\right) = \mathbf{V}, \tag{2.28}$$

where $\mathbf{V} = \mathbf{W^T y}$, and

$$\begin{aligned}\nabla_{\mathbf{x}}\left(\mathbf{x^T M x}\right) &= (\mathbf{M} + \mathbf{M^T})\mathbf{x} \\ &= 2\mathbf{M x} \quad \text{(if } \mathbf{M} \text{ is symmetric)},\end{aligned} \tag{2.29}$$

where $\mathbf{M} = \mathbf{W^T W}$.

Identical to the situation faced at (2.18), (2.27) is only valid if $\left(\mathbf{W^T W}\right)$ is invertible. Thus Tikhonov regularization can also be implemented when finding the ML solution. Injecting $\alpha\|\mathbf{Qx}\|^2$ into $f(\mathbf{x})$ in (2.24) introduces an artificial/penalty term governed by the derivative of the image defined by (2.20). The impact of $\alpha\|\mathbf{Qx}\|^2$ is such that it penalizes “rough" images thereby “smoothing" the image out.

$$f(\mathbf{x}) = -\frac{1}{2\sigma^2}\left(\mathbf{y^T y} - \mathbf{2x^T W^T y} + \mathbf{x^T W^T W x} + \alpha\|\mathbf{Qx}\|^2\right). \tag{2.30}$$

Since the image will be two-dimensional (2D) for this thesis, Tikhonov regularization calls for including derivatives in both the horizontal and vertical dimensions, i.e.

$$\begin{aligned}f(\mathbf{x}) &= -\frac{1}{2\sigma^2}\left(\mathbf{y^T y} - \mathbf{2x^T W^T y} + \mathbf{x^T W^T W x} + \alpha\left(\|\mathbf{D}_H\mathbf{x}\|^2 + \|\mathbf{D}_V\mathbf{x}\|^2\right)\right) \\ &= -\frac{1}{2\sigma^2}\left(\mathbf{y^T y} - \mathbf{2x^T W^T y} + \mathbf{x^T W^T W x} + \alpha\left([\mathbf{D}_H\mathbf{x}]^T[\mathbf{D}_H\mathbf{x}] + [\mathbf{D}_V\mathbf{x}]^T[\mathbf{D}_V\mathbf{x}]\right)\right) \\ &= -\frac{1}{2\sigma^2}\left(\mathbf{y^T y} - \mathbf{2x^T W^T y} + \mathbf{x^T W^T W x} + \alpha\left(\mathbf{x}^T\mathbf{D}_H^T\mathbf{D}_H\mathbf{x} + \mathbf{x}^T\mathbf{D}_V^T\mathbf{D}_V\mathbf{x}\right)\right).\end{aligned} \tag{2.31}$$

Equation (2.25) now becomes

$$\begin{aligned}
\underset{\hat{\mathbf{x}}}{\arg\max}\ \mathscr{L} &= \nabla_{\mathbf{x}}\mathscr{L} \equiv \mathbf{0} \\
-\frac{1}{2\sigma^2}\left(-\mathbf{2W^T y} + \mathbf{2W^T W}\hat{\mathbf{x}} + \alpha\left[2\mathbf{D}_H^T\mathbf{D}_H\hat{\mathbf{x}} + 2\mathbf{D}_V^T\mathbf{D}_V\hat{\mathbf{x}}\right]\right) &\equiv \mathbf{0} \qquad (2.32) \\
\mathbf{W^T y} - \mathbf{W^T W}\hat{\mathbf{x}} - \alpha\left[\mathbf{D}_H^T\mathbf{D}_H\hat{\mathbf{x}} + \mathbf{D}_V^T\mathbf{D}_V\hat{\mathbf{x}}\right] &\equiv \mathbf{0} \\
\mathbf{W^T W}\hat{\mathbf{x}} + \alpha\left[\mathbf{D}_H^T\mathbf{D}_H\hat{\mathbf{x}} + \mathbf{D}_V^T\mathbf{D}_V\hat{\mathbf{x}}\right] &= \mathbf{W^T y} \\
\left(\mathbf{W}^T\mathbf{W} + \alpha\left[\mathbf{D}_H^T\mathbf{D}_H + \mathbf{D}_V^T\mathbf{D}_V\right]\right)\hat{\mathbf{x}} &= \mathbf{W^T y} \\
\hat{\mathbf{x}} &= \underbrace{\left(\mathbf{W}^T\mathbf{W} + \alpha\left[\mathbf{D}_H^T\mathbf{D}_H + \mathbf{D}_V^T\mathbf{D}_V\right]\right)^{-1}\mathbf{W^T}}_{\mathbf{\Pi}}\mathbf{y}. \qquad (2.33)
\end{aligned}$$

Again, (2.32) utilizes the vector calculus identities of (2.28) and (2.29) which also deals with the injected Tikhonov related matrices and vectors.

2.2 Noise Radar

Similar to the approach taken for the RTI literature review section prior, we shall explore error statistics related to the use of Ultra-wideband (UWB) noise radar for target identification and location. As a reminder, determining the noise and/or error statistics will help build an appropriate system model for the purpose of implementation in multi-sensor data fusion techniques.

One of the boasted features of a noise radar is its attribute of utilizing a waveform with an ideal “thumbtack" ambiguity function, providing unambiguous high resolution imaging at any distance [6]. According to the mathematical relationship [15]

$$\Delta R = \gamma\frac{c}{2B}, \qquad (2.34)$$

Equation (2.34) quantitatively describes the amount of separation required to resolve

two targets in range, using the speed of light, c, and the waveform bandwidth, B. The factor, γ, in the range $1 \leq \gamma < 2$, represents the degradation in range resolution resulting from system errors or range sidelobe reduction techniques such as windowing. Given a UWB noise radar operating between the frequencies of 500 MHz and 1000 MHz with $\gamma = 2$, the theoretical range resolution of the UWB noise radar can range from 0.6 m down to 0.3 m respectively.

Early work in [16] suggests an estimation of the measurement error for radar is generally impossible. The argument used for this is that the measurements include errors which are dependent on the SNR and the equipment. Further, the echo power is generally unknown to the radar since the target reflection varies not only from target to target but also with time for each target. Reference [16] proposes that the reasons stated prior are why a fixed standard deviation of measurement error is used (in the context of tracking). The suggested assumption for the fixed standard deviation of monostatic and bistatic radar measurement range error, σ_ρ was given as

$$\sigma_\rho = 0.1 \frac{c}{\tau}, \tag{2.35}$$

where τ is the transmitted pulse length.

The AFIT Noise Network (NoNET) came into fruition with the work started in [17]. Simulation, design and implementation of a network of three digital noise radars was performed to triangulate the coordinates of a target within a room. Given the experimental setups in [17], in nine out of ten cases the stationary targets were detected with eight out of ten located within the range resolution of the system of 0.375 m. There were no significant error/accuracy analysis of the noise radar apart from acknowledging that the sampling frequency is a limitation to range accuracy, i.e. using a sampling frequency of 1.5 GHz, the resulting range increment is 0.1 m.

Follow on work from [17] was conducted in [18] where the AFIT NoNET was utilized

under a multistatic configuration. Theoretical as well as experimental error analysis was conducted on the AFIT NoNET in monostatic and multistatic configurations. For the monostatic case, the one dimensional theoretical range accuracy was calculated from the CRLB using the two way time delay to target, τ, which is assumed to be a measurement parameter of an unbiased estimator. It was determined that the theoretical lower bound of the standard deviation time delay error, σ_t, was 0.302 ns (0.0453 m). The measured standard deviation time delay was found to be 0.319 ns (0.0478 m), a reasonable result compared to the theoretical.

However, for the multistatic case, [18] did not provide two dimensional, theoretical range and cross-range accuracy estimates. Rather, accuracies for the multistatic configuration were found through analysis of experimental results. The average localization error was assessed to be 0.077 m with a standard deviation of 0.031 m.

The research effort in [19] explored simultaneous range and velocity detection in one dimension with the AFIT NoNET. The method of measuring the internal noise of the system was to transmit and receive without any antennas. The numerical results showed approximately equal variances but non-zero and non-equal means, conflicting with the initial assumption of AWGN. The non-zero and non-equal means were attributed to the fact that the internal noise collections were sampled after the bandpass filter, causing the power spectral density (PSD) of the internal noise to be no longer uniform across the frequency spectrum. Reference [19] concludes with an experimental range error of 1 m, justified by the comparison against the theoretical calculation and plot of a range ambiguity function for the AFIT NoNET.

2.3 Data Fusion

2.3.1 Kalman Filter.

The Kalman filter is a common and widely used fusion algorithm that is utilized whenever the state of a system can be estimated from multiple sources of noisy sensor information. Two methods for Kalman-filter-based data fusion include state-vector fusion and measurement fusion whose differences are illustrated in Figure 2.1.

References [20–22] state that measurement fusion is preferable to state-vector fusion in practical situations, implying that the state-vector fusion method is only effective when Kalman filters are consistent. Consistency is in reference to when the underlying process of the state model is linear, i.e., when forced to deal with non-linear models, inconsistencies may arise due to the linearization process. However, [23] states that the measurement fusion approach is optimal but not computationally efficient.

The key set of equations used for the Kalman filter can be separated into three categories: the dynamic system model, the predict equations and the update equations.

2.3.1.1 Dynamic System Model.

Assuming the true state, $\mathbf{x}_k$ at time k is evolved from the state at time $(k-1)$, Kalman filters are based on linear models discretized in the time domain according to

$$\mathbf{x}_k = \mathbf{F}_k \mathbf{x}_{k-1} + \mathbf{B}_k \mathbf{u}_k + \mathbf{w}_k, \tag{2.36}$$

where

- $\mathbf{F}_k$ is the state transition model applied to the previous state $\mathbf{x}_{k-1}$
- $\mathbf{B}_k$ is the control input model applied to the control vector $\mathbf{u}_k$

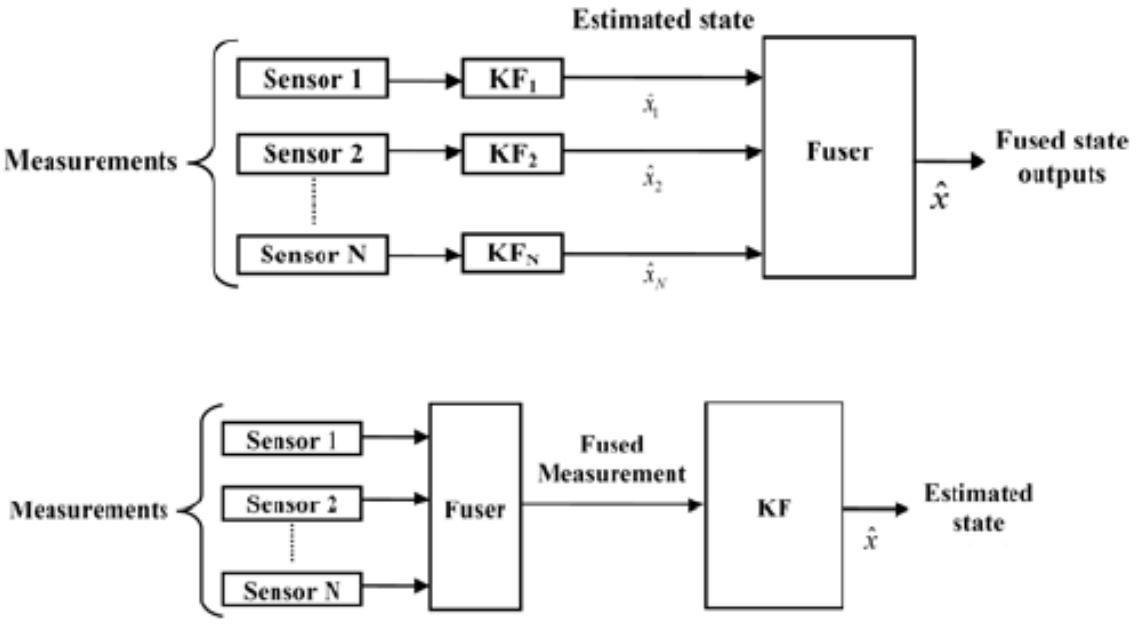

Figure 2.1. Kalman-filter-based data fusion methods. Top: State-vector fusion. Bottom: Measurement fusion.

- $\mathbf{w}_k$ is the process noise assumed to be drawn from a zero mean multivariate normal distribution with covariance $\mathbf{Q}_k$.

In order to have states there needs to be an observation, $\mathbf{z}_k$ of the true state $\mathbf{x}_k$

$$\mathbf{z}_k = \mathbf{H}_k \mathbf{x}_k + \mathbf{v}_k \tag{2.37}$$

where

- $\mathbf{H}_k$ is the observation model mapping the true state space into the observed space
- $\mathbf{v}_k$ is the observation noise assumed to be zero mean Gaussian white noise with covariance $\mathbf{R}_k$.

2.3.1.2 Prediction.

The prediction equation uses the state estimate from the previous time step, $\hat{\mathbf{x}}_{k-1}$ to produce an estimate of the state at the current time step, $\hat{\mathbf{x}}_k^-$ i.e.

$$\hat{\mathbf{x}}_k^- = \mathbf{F}_k \hat{\mathbf{x}}_{k-1} + \mathbf{B}_k \mathbf{u}_k, \tag{2.38}$$

with its predicted error covariance, $\mathbf{P}_k^-$ given by

$$\mathbf{P}_k^- = \mathbf{F}_k \mathbf{P}_{k-1} \mathbf{F}_k^T + \mathbf{Q}_k. \tag{2.39}$$

Equations (2.38) and (2.39) are respectively referred as the *a priori* state estimate and error covariance as they do not include observation information, (2.37) from the current time step.

2.3.1.3 Update.

The update equation uses the *a priori* prediction state estimate (2.38) with the current observation information (2.37) to update the state estimate, $\hat{\mathbf{x}}_k$

$$\hat{\mathbf{x}}_k = \hat{\mathbf{x}}_k^- + \mathbf{K}_k(\mathbf{z}_k - \mathbf{H}_k \hat{\mathbf{x}}_k^-) \tag{2.40}$$

where $\mathbf{K}_k$ is the Kalman gain given by

$$\mathbf{K}_k = \mathbf{P}_k \mathbf{H}_k^T (\mathbf{R}_k + \mathbf{H}_k \mathbf{P}_k^- \mathbf{H}_k^T)^{-1}. \tag{2.41}$$

The updated error covariance matrix, $\mathbf{P}_k$ is

$$\mathbf{P}_k = (\mathbf{I} - \mathbf{K}_k \mathbf{H}) \mathbf{P}_k^-. \tag{2.42}$$

Note that (2.40) and (2.42) are respectively known as the *a posteriori* state estimate and the *a posteriori* error covariance matrix to differentiate them from (2.38) and (2.39).

2.3.1.4 State-vector Fusion.

Introduced by [24], an advantage of using state-vector fusion is that it can be implemented without a central processor [22]. In addition, state-vector fusion is shown to have the advantages of parallel implementation and fault-tolerance [25]. References [21, 23] identify three approaches to state-vector fusion:

1. weighted covariance
2. information matrix
3. pseudomeasurement.

The focus of the work in [23] was solely on the information matrix approach, providing an evaluation methodology for comparing the performance of several fusion algorithms with the information matrix.

2.3.1.5 Measurement Fusion.

There are two commonly used methods of measurement fusion referred as Method I and Method II [20, 21]. Method I simply merges the multisensor data increasing the dimension of the observation vector $\mathbf{z}$ (2.37) whereas Method II combines the multisensor data based on minimum-mean-square-error estimates without affecting the dimension of $\mathbf{z}$. Derivations and simulations in [20] shows that if the observation matrix, $\mathbf{H}$ are not the same for each sensor, Method II is preferred. However, Method I is shown to be more flexible and will become more efficient in the sense of computational cost.

2.3.1.6 Noise Statistics.

In many practical applications, the noise statistics are partially unknown. Reference [21] derives, simulates and analyzes “on-line" self-tuning Kalman filters for multisensor systems with unknown variance matrices, **Q** and **R** (“on-line" refers to the act of tuning whilst the system is operational). Self-tuning filters are based on a recursion of noise statistics, and [21] utilizes this in conjunction with a correlation method to present a self-tuning Kalman filter for systems with identical or different observation matrices, **H**.

Reference [26] expresses the fact that the **Q** and **R** matrices do not always contain white error sources and refers to the use of a Schmidt-Kalman filter under those circumstances. Besides using the “on-line" method of calculating **Q** and **R**, [26] highlights the availability of an “off-line" procedure using Powell’s method on prerecorded data sets. Ultimately, the work in [26] was to integrate data from gyroscopic orientation sensors and gravimetric inclinometers to create an inertial system, and the route taken to calculate the noise statistics was to take a simpler but crude approach, ignoring the unmodeled states and "bumping” up the **Q** and **R** matrices to account for the noises in the states being discarded.

Ultimately, the availability of *a priori* noise statistics is often unavailable and is especially true if changes in the environment occur and/or if it has a complex structure [27]. However, poor estimates/assumptions of the noise statistics risk serious degradation of the Kalman filter to the point of divergence. This is what has fueled the research into “adaptive/self-tuning" filters.

III. Methodology

This chapter details the steps taken to explore the proof of concept of Multi-Sensor Data Fusion (MSDF) between the two disparate sensor technologies of Radio Tomographic Imaging (RTI) and a Noise Radar Network (NRN). A system model definition is proposed, acting as the foundation on what mathematically ties the sensor technologies together. The experimental procedure follows this, presenting the steps taken to collect and process the raw data captured by each sensor.

3.1 Linearizing Trilateration for Image Construction

In order to fuse two disparate sensor technologies, considerations were made into the underlying equations that could best facilitate multi-sensor data fusion. As the linear formulation was already well established with RTI, an attempt to linearize trilateration using a single Air Force Institute of Technology (AFIT) Noise Network (NoNET) node was made with the following equation:

$$\begin{aligned} \mathbf{y}_{\mathrm{NR}z} &= \mathbf{W}_{\mathrm{NR}z}\mathbf{x}_{\mathrm{NR}z} + \mathbf{n}_{\mathrm{NR}z} \\ \mathbf{n}_{\mathrm{NR}z} &\sim \mathcal{N}(\mathbf{0}, \mathbf{C}_{\mathrm{NR}z}), \end{aligned} \tag{3.1}$$

where

- $\mathbf{x}_{\mathrm{NR}z}$ is the $N \times 1$ reflection image to be estimated with N pixels from the zth NRN node.
- $\mathbf{y}_{\mathrm{NR}z}$ is the $I \times 1$ vector of magnitudes in the impulse response/cross correlation magnitudes at I calibrated ranges from the zth NRN node.
- $\mathbf{W}_{\mathrm{NR}z}$ is the weighting matrix with each column representing a single pixel and each row describing the weighting of each pixel for a particular range.

- $\mathbf{n}_{\mathrm{NR}z}$ is the noise vector of the zth NRN node.

Thus, when employing more than one AFIT NoNET node, or as was limited to in this thesis, transmitting and receiving from three locations using just one AFIT NoNET node, it is proposed that (3.1) can be generalized into

$$\begin{bmatrix} \mathbf{y}_{\mathrm{NR1}} \\ \mathbf{y}_{\mathrm{NR2}} \\ \mathbf{y}_{\mathrm{NR3}} \end{bmatrix} = \begin{bmatrix} \mathbf{W}_{\mathrm{NR1}} \\ \mathbf{W}_{\mathrm{NR2}} \\ \mathbf{W}_{\mathrm{NR3}} \end{bmatrix} \mathbf{x}_{\mathrm{NRN}} + \begin{bmatrix} \mathbf{n}_{\mathrm{NR1}} \\ \mathbf{n}_{\mathrm{NR2}} \\ \mathbf{n}_{\mathrm{NR3}} \end{bmatrix} \tag{3.2}$$

$$\mathbf{y}_{\mathrm{NRN}} = \mathbf{W}_{\mathrm{NRN}}\mathbf{x}_{\mathrm{NRN}} + \mathbf{n}_{\mathrm{NRN}} \quad \mathbf{n}_{\mathrm{NRN}} \sim \mathcal{N}\left(\begin{bmatrix} \mathbf{0} \\ \mathbf{0} \\ \mathbf{0} \end{bmatrix}, \mathbf{C}_{\mathrm{NRN}} = \begin{bmatrix} \mathbf{C}_{\mathrm{NR1}} & \mathbf{0} & \mathbf{0} \\ \mathbf{0} & \mathbf{C}_{\mathrm{NR2}} & \mathbf{0} \\ \mathbf{0} & \mathbf{0} & \mathbf{C}_{\mathrm{NR3}} \end{bmatrix} \right).$$

This leaves the question of what the weighting matrix, $\mathbf{W}_{\mathrm{NR}z}$, needs to be.

3.2 Weight Model for Trilateration

This thesis works on the concept of trilateration by taking an AFIT NoNET node to three known locations to transmit and receive. The transmit and receive signals are assumed to be omnidirectional allowing the concept of range rings to be made use of in image reconstruction. Therefore, the proposed weight model for trilateration is mathematically described as

$$\mathrm{w}_{i,j}^{\mathrm{Trilateration}} = \begin{cases} 1, & \text{if } \left(x_j - h\right)^2 + \left(y_j - k\right)^2 \geq r_{\mathrm{inner},i}^2 \ \mathbf{\&} \ \left(x_j - h\right)^2 + \left(y_j - k\right)^2 \leq r_{\mathrm{outer},i}^2 \\ 0, & \text{otherwise} \end{cases} \tag{3.3}$$

where,

- x_j is the x coordinate of the jth pixel

- h is the x coordinate of the AFIT NoNET node
- y_j is the y coordinate of the jth pixel
- k is the y coordinate of the AFIT NoNET node
- $r_{\text{inner},i}$ is the inner radius of the range ring which equals the ith range $-$ range resolution/2
- $r_{\text{outer},i}$ is the outer radius of the range ring which equals the ith range + range resolution/2.

Qualitatively, (3.3) is the equation for an annulus, i.e. a ring-shaped object, centered at the AFIT NoNET node's known coordinates (h,k) who's region is bounded by the sensor's empirical range resolution.

3.3 Multi-Sensor Data Fusion Image Reconstruction

Following the linear dynamic system model format of (2.6), a preliminary MSDF model is presented as

$$\begin{bmatrix} \mathbf{y}_{\text{RTI}} \\ \mathbf{y}_{\text{NRN}} \end{bmatrix} = \begin{bmatrix} \mathbf{W}_{\text{RTI}} \\ \mathbf{W}_{\text{NRN}} \end{bmatrix} \mathbf{x}_{\text{FUS}} + \begin{bmatrix} \mathbf{n}_{\text{RTI}} \\ \mathbf{n}_{\text{NRN}} \end{bmatrix} \tag{3.4}$$

$$\mathbf{y}_{\text{FUS}} = \mathbf{W}_{\text{FUS}}\mathbf{x}_{\text{FUS}} + \mathbf{n}_{\text{FUS}} \tag{3.5}$$

$$\mathbf{n}_{\text{FUS}} \sim \mathcal{N}\left(\begin{bmatrix} \mathbf{0} \\ \mathbf{0} \end{bmatrix}, \mathbf{C}_{\text{FUS}} = \begin{bmatrix} \mathbf{C}_{\text{RTI}} & \mathbf{0} \\ \mathbf{0} & \mathbf{C}_{\text{NRN}} \end{bmatrix} \right),$$

where

- $\mathbf{y}_{\text{RTI}}$ is the calibrated received signal strength (RSS) values from all M links in the RTI network

- $\mathbf{y}_{\text{NRN}}$ is the stacked calibrated impulse response/cross correlation magnitudes from each NRN node.

- $\mathbf{x}_{\text{FUS}}$ is the fusion image of the RTI and the AFIT NoNET sensors.

Image reconstruction for MSDF involves solving for $\mathbf{x}_{\text{FUS}}$ in (3.5). This will be achieved by taking the maximum likelihood (ML) derivation similar to Subsection 2.1.2, i.e.

$$\begin{aligned}\hat{\mathbf{x}}_{\text{FUS,ML}}(\mathbf{y}) &= \underset{\hat{\mathbf{x}}_{\text{FUS}}}{\arg\max}\ \ln \wp(\mathbf{y}_{\text{FUS}}|\mathbf{x}_{\text{FUS}}) \\ &= \underset{\hat{\mathbf{x}}_{\text{FUS}}}{\arg\max}\ \mathscr{L},\end{aligned} \tag{3.6}$$

where $\mathscr{L}$ is known as the log likelihood function. Assuming the noise vector $\mathbf{n}_{\text{FUS}} \sim \mathscr{N}(\mathbf{0}, \mathbf{C}_{\text{FUS}})$, therefore $\mathbf{y} \sim \mathscr{N}(\mathbf{W}_{\text{FUS}}\mathbf{x}_{\text{FUS}}, \mathbf{C}_{\text{FUS}})$. Hence,

$$\mathscr{L} = \ln\left[\left(\frac{1}{\sqrt{2\pi}^N |\mathbf{C}_{\text{FUS}}|}\right)\exp\left(-\frac{(\mathbf{y}_{\text{FUS}} - \mathbf{W}_{\text{FUS}}\mathbf{x}_{\text{FUS}})^T (\mathbf{C}_{\text{FUS}})^{-1}(\mathbf{y}_{\text{FUS}} - \mathbf{W}_{\text{FUS}}\mathbf{x}_{\text{FUS}})}{2}\right)\right] \tag{3.7}$$

$$\begin{aligned}
&= -\text{N}\ln\left(\sqrt{2\pi}\right) - \ln\left(|\mathbf{C}_{\text{FUS}}|\right) - \frac{1}{2}\left(\mathbf{y}_{\text{FUS}} - \mathbf{W}_{\text{FUS}}\mathbf{x}_{\text{FUS}}\right)^T (\mathbf{C}_{\text{FUS}})^{-1}\left(\mathbf{y}_{\text{FUS}} - \mathbf{W}_{\text{FUS}}\mathbf{x}_{\text{FUS}}\right) \\
&= -\text{N}\ln\left(\sqrt{2\pi}\right) - \ln\left(|\mathbf{C}_{\text{FUS}}|\right) - \frac{1}{2}\left(\mathbf{y}_{\text{FUS}}^T - \mathbf{x}_{\text{FUS}}^T\mathbf{W}_{\text{FUS}}^T\right)(\mathbf{C}_{\text{FUS}})^{-1}\left(\mathbf{y}_{\text{FUS}} - \mathbf{W}_{\text{FUS}}\mathbf{x}_{\text{FUS}}\right) \\
&= -\text{N}\ln\left(\sqrt{2\pi}\right) - \ln\left(|\mathbf{C}_{\text{FUS}}|\right) - \frac{1}{2}\left(\mathbf{y}_{\text{FUS}}^T\mathbf{C}_{\text{FUS}}^{-1} - \mathbf{x}_{\text{FUS}}^T\mathbf{W}_{\text{FUS}}^T\mathbf{C}_{\text{FUS}}^{-1}\right)\left(\mathbf{y}_{\text{FUS}} - \mathbf{W}_{\text{FUS}}\mathbf{x}_{\text{FUS}}\right) \\
&= -\text{N}\ln\left(\sqrt{2\pi}\right) - \ln\left(|\mathbf{C}_{\text{FUS}}|\right) - \frac{1}{2}\big(\mathbf{y}_{\text{FUS}}^T\mathbf{C}_{\text{FUS}}^{-1}\mathbf{y}_{\text{FUS}} - \mathbf{y}_{\text{FUS}}^T\mathbf{C}_{\text{FUS}}^{-1}\mathbf{W}_{\text{FUS}}\mathbf{x}_{\text{FUS}} \cdots \\
&\qquad\qquad - \mathbf{x}_{\text{FUS}}^T\mathbf{W}_{\text{FUS}}^T\mathbf{C}_{\text{FUS}}^{-1}\mathbf{y}_{\text{FUS}} + \mathbf{x}_{\text{FUS}}^T\mathbf{W}_{\text{FUS}}^T\mathbf{C}_{\text{FUS}}^{-1}\mathbf{W}_{\text{FUS}}\mathbf{x}_{\text{FUS}}\big) \\
&= -\text{N}\ln\left(\sqrt{2\pi}\right) - \ln\left(|\mathbf{C}_{\text{FUS}}|\right) - \frac{1}{2}\big(\mathbf{y}_{\text{FUS}}^T\mathbf{C}_{\text{FUS}}^{-1}\mathbf{y}_{\text{FUS}} - \left[\mathbf{y}_{\text{FUS}}^T\mathbf{C}_{\text{FUS}}^{-1}\mathbf{W}_{\text{FUS}}\mathbf{x}_{\text{FUS}}\right]^T \cdots \\
&\qquad\qquad - \mathbf{x}_{\text{FUS}}^T\mathbf{W}_{\text{FUS}}^T\mathbf{C}_{\text{FUS}}^{-1}\mathbf{y}_{\text{FUS}} + \mathbf{x}_{\text{FUS}}^T\mathbf{W}_{\text{FUS}}^T\mathbf{C}_{\text{FUS}}^{-1}\mathbf{W}_{\text{FUS}}\mathbf{x}_{\text{FUS}}\big) \\
&= -\text{N}\ln\left(\sqrt{2\pi}\right) - \ln\left(|\mathbf{C}_{\text{FUS}}|\right) - \frac{1}{2}\big(\mathbf{y}_{\text{FUS}}^T\mathbf{C}_{\text{FUS}}^{-1}\mathbf{y}_{\text{FUS}} - \mathbf{x}_{\text{FUS}}^T\mathbf{W}_{\text{FUS}}^T\mathbf{C}_{\text{FUS}}^{-1}\mathbf{y}_{\text{FUS}} \cdots \\
&\qquad\qquad - \mathbf{x}_{\text{FUS}}^T\mathbf{W}_{\text{FUS}}^T\mathbf{C}_{\text{FUS}}^{-1}\mathbf{y}_{\text{FUS}} + \mathbf{x}_{\text{FUS}}^T\mathbf{W}_{\text{FUS}}^T\mathbf{C}_{\text{FUS}}^{-1}\mathbf{W}_{\text{FUS}}\mathbf{x}_{\text{FUS}}\big)
\end{aligned} \tag{3.8}$$

$$= -\text{N}\ln\left(\sqrt{2\pi}\right) - \ln\left(|\mathbf{C}_{\text{FUS}}|\right) + f(\mathbf{x}_{\text{FUS}}). \tag{3.9}$$

Note that we want the arg max of $\mathscr{L}$, but due to the $-1/2$ term in (3.8), this implies that we should solve for $f(\mathbf{x})$ in (3.9).

$$\arg\max_{\hat{\mathbf{x}}} \mathscr{L} = \nabla_{\mathbf{x}} \mathscr{L} \equiv \mathbf{0} \tag{3.10}$$

$$\begin{aligned}
\mathbf{0} - \mathbf{0} - \frac{1}{2}\Big(\mathbf{0} - \mathbf{W}_{\text{FUS}}^T \mathbf{C}_{\text{FUS}}^{-1} \mathbf{y}_{\text{FUS}} - \mathbf{W}_{\text{FUS}}^T \mathbf{C}_{\text{FUS}}^{-1} \mathbf{y}_{\text{FUS}} + \cdots \\
\Big[\big(\mathbf{W}_{\text{FUS}}^T \mathbf{C}_{\text{FUS}}^{-1} \mathbf{W}_{\text{FUS}} \big) + \big(\mathbf{W}_{\text{FUS}}^T \mathbf{C}_{\text{FUS}}^{-1} \mathbf{W}_{\text{FUS}} \big)^T \Big] \hat{\mathbf{x}}_{\text{FUS}} \Big) \equiv \mathbf{0} \\
-\frac{1}{2} \big(-2\mathbf{W}_{\text{FUS}}^T \mathbf{C}_{\text{FUS}}^{-1} \mathbf{y}_{\text{FUS}} + \big[2\mathbf{W}_{\text{FUS}}^T \mathbf{C}_{\text{FUS}}^{-1} \mathbf{W}_{\text{FUS}} \big] \hat{\mathbf{x}}_{\text{FUS}} \big) \equiv \mathbf{0} \\
\mathbf{W}_{\text{FUS}}^T \mathbf{C}_{\text{FUS}}^{-1} \mathbf{y}_{\text{FUS}} - \mathbf{W}_{\text{FUS}}^T \mathbf{C}_{\text{FUS}}^{-1} \mathbf{W}_{\text{FUS}} \hat{\mathbf{x}}_{\text{FUS}} \equiv \mathbf{0} \\
\mathbf{W}_{\text{FUS}}^T \mathbf{C}_{\text{FUS}}^{-1} \mathbf{W}_{\text{FUS}} \hat{\mathbf{x}}_{\text{FUS}} = \mathbf{W}_{\text{FUS}}^T \mathbf{C}_{\text{FUS}}^{-1} \mathbf{y}_{\text{FUS}} \\
\hat{\mathbf{x}}_{\text{FUS}} = \big(\mathbf{W}_{\text{FUS}}^T \mathbf{C}_{\text{FUS}}^{-1} \mathbf{W}_{\text{FUS}} \big)^{-1} \mathbf{W}_{\text{FUS}}^T \mathbf{C}_{\text{FUS}}^{-1} \mathbf{y}_{\text{FUS}}.
\end{aligned} \tag{3.11, 3.12}$$

For (3.11), the vector calculus identities of (2.28) and (2.29) were used.

Since $\big(\mathbf{W}_{\text{FUS}}^T \mathbf{C}_{\text{FUS}}^{-1} \mathbf{W}_{\text{FUS}} \big)$ in (3.12) is not invertible, we now apply Tikhonov regularization by injecting $\alpha_{\text{FUS}} \|\mathbf{Q}\mathbf{x}_{\text{FUS}}\|^2$ into $f(\mathbf{x}_{\text{FUS}})$ in (3.9) to create certain desired properties that enforces a solution. α_{FUS} is a tunable weight parameter where small values lead to solutions that fit the data and large values favor prior information.

$$\begin{aligned}
f(\mathbf{x}) = -\frac{1}{2} \big(\mathbf{y}_{\text{FUS}}^T \mathbf{C}_{\text{FUS}}^{-1} \mathbf{y}_{\text{FUS}} - \mathbf{x}_{\text{FUS}}^T \mathbf{W}_{\text{FUS}}^T \big[\mathbf{C}_{\text{FUS}}^{-1} \big]^T \mathbf{y}_{\text{FUS}} - \mathbf{x}_{\text{FUS}}^T \mathbf{W}_{\text{FUS}}^T \mathbf{C}_{\text{FUS}}^{-1} \mathbf{y}_{\text{FUS}} + \cdots \\
\mathbf{x}_{\text{FUS}}^T \mathbf{W}_{\text{FUS}}^T \mathbf{C}_{\text{FUS}}^{-1} \mathbf{W}_{\text{FUS}} \mathbf{x}_{\text{FUS}} + \alpha \|\mathbf{Q}\mathbf{x}_{\text{FUS}}\|^2 \big).
\end{aligned} \tag{3.13}$$

Since the image will be two-dimensional (2D) for this thesis, Tikhonov regularization

calls for including derivatives in both the horizontal and vertical dimensions, i.e.

$$f(\mathbf{x}) = -\frac{1}{2}\Big(\mathbf{y}_{\text{FUS}}^T\mathbf{C}_{\text{FUS}}^{-1}\mathbf{y}_{\text{FUS}} - \mathbf{x}_{\text{FUS}}^T\mathbf{W}_{\text{FUS}}^T\left[\mathbf{C}_{\text{FUS}}^{-1}\right]^T\mathbf{y}_{\text{FUS}} - \mathbf{x}_{\text{FUS}}^T\mathbf{W}_{\text{FUS}}^T\mathbf{C}_{\text{FUS}}^{-1}\mathbf{y}_{\text{FUS}} + \cdots$$
$$\mathbf{x}_{\text{FUS}}^T\mathbf{W}_{\text{FUS}}^T\mathbf{C}_{\text{FUS}}^{-1}\mathbf{W}_{\text{FUS}}\mathbf{x}_{\text{FUS}} + \alpha_{\text{FUS}}\left(\|\mathbf{D}_H\mathbf{x}_{\text{FUS}}\|^2 + \|\mathbf{D}_V\mathbf{x}_{\text{FUS}}\|^2\right)\Big) \tag{3.14}$$

$$f(\mathbf{x}) = -\frac{1}{2}\Big(\mathbf{y}_{\text{FUS}}^T\mathbf{C}_{\text{FUS}}^{-1}\mathbf{y}_{\text{FUS}} - \mathbf{x}_{\text{FUS}}^T\mathbf{W}_{\text{FUS}}^T\left[\mathbf{C}_{\text{FUS}}^{-1}\right]^T\mathbf{y}_{\text{FUS}} - \mathbf{x}_{\text{FUS}}^T\mathbf{W}_{\text{FUS}}^T\mathbf{C}_{\text{FUS}}^{-1}\mathbf{y}_{\text{FUS}} + \cdots$$
$$\mathbf{x}_{\text{FUS}}^T\mathbf{W}_{\text{FUS}}^T\mathbf{C}_{\text{FUS}}^{-1}\mathbf{W}_{\text{FUS}}\mathbf{x}_{\text{FUS}} + \alpha_{\text{FUS}}\left(\left[\mathbf{D}_H\mathbf{x}_{\text{FUS}}\right]^T\left[\mathbf{D}_H\mathbf{x}_{\text{FUS}}\right] + \left[\mathbf{D}_V\mathbf{x}_{\text{FUS}}\right]^T\left[\mathbf{D}_V\mathbf{x}_{\text{FUS}}\right]\right)\Big) \tag{3.15}$$

$$f(\mathbf{x}) = -\frac{1}{2}\Big(\mathbf{y}_{\text{FUS}}^T\mathbf{C}_{\text{FUS}}^{-1}\mathbf{y}_{\text{FUS}} - \mathbf{x}_{\text{FUS}}^T\mathbf{W}_{\text{FUS}}^T\left[\mathbf{C}_{\text{FUS}}^{-1}\right]^T\mathbf{y}_{\text{FUS}} - \mathbf{x}_{\text{FUS}}^T\mathbf{W}_{\text{FUS}}^T\mathbf{C}_{\text{FUS}}^{-1}\mathbf{y}_{\text{FUS}} + \cdots$$
$$\mathbf{x}_{\text{FUS}}^T\mathbf{W}_{\text{FUS}}^T\mathbf{C}_{\text{FUS}}^{-1}\mathbf{W}_{\text{FUS}}\mathbf{x}_{\text{FUS}} + \alpha_{\text{FUS}}\left(\mathbf{x}_{\text{FUS}}^T\mathbf{D}_H^T\mathbf{D}_H\mathbf{x}_{\text{FUS}} + \mathbf{x}_{\text{FUS}}^T\mathbf{D}_V^T\mathbf{D}_V\mathbf{x}_{\text{FUS}}\right)\Big) \tag{3.16}$$

(3.10) now becomes

$$\underset{\hat{\mathbf{x}}}{\arg\max}\ \mathscr{L} = \nabla_{\mathbf{x}}\mathscr{L} \equiv \mathbf{0} \tag{3.17}$$

$$-\frac{1}{2}\Bigg(\mathbf{0} - \mathbf{W}_{\text{FUS}}^T\left[\mathbf{C}_{\text{FUS}}^{-1}\right]^T\mathbf{y}_{\text{FUS}} - \mathbf{W}_{\text{FUS}}^T\mathbf{C}_{\text{FUS}}^{-1}\mathbf{y}_{\text{FUS}} + \Bigg[\left(\mathbf{W}_{\text{FUS}}^T\mathbf{C}_{\text{FUS}}^{-1}\mathbf{W}_{\text{FUS}}\right) + \cdots$$
$$\left(\mathbf{W}_{\text{FUS}}^T\mathbf{C}_{\text{FUS}}^{-1}\mathbf{W}_{\text{FUS}}\right)^T\Bigg]\hat{\mathbf{x}}_{\text{FUS}} + \alpha_{\text{FUS}}\left[2\mathbf{D}_H^T\mathbf{D}_H\hat{\mathbf{x}}_{\text{FUS}} + 2\mathbf{D}_V^T\mathbf{D}_V\hat{\mathbf{x}}_{\text{FUS}}\right]\Bigg) \equiv \mathbf{0} \tag{3.18}$$

$$-\frac{1}{2}\left(-2\mathbf{W}_{\text{FUS}}^T\mathbf{C}_{\text{FUS}}^{-1}\mathbf{y}_{\text{FUS}} + \left[2\mathbf{W}_{\text{FUS}}^T\mathbf{C}_{\text{FUS}}^{-1}\mathbf{W}_{\text{FUS}}\right]\hat{\mathbf{x}}_{\text{FUS}} + 2\alpha_{\text{FUS}}\left[\mathbf{D}_H^T\mathbf{D}_H\hat{\mathbf{x}}_{\text{FUS}} + 2\mathbf{D}_V^T\mathbf{D}_V\hat{\mathbf{x}}_{\text{FUS}}\right]\right) \equiv \mathbf{0} \tag{3.19}$$

$$\mathbf{W}_{\text{FUS}}^T\mathbf{C}_{\text{FUS}}^{-1}\mathbf{y}_{\text{FUS}} - \mathbf{W}_{\text{FUS}}^T\mathbf{C}_{\text{FUS}}^{-1}\mathbf{W}_{\text{FUS}}\hat{\mathbf{x}}_{\text{FUS}} + \alpha_{\text{FUS}}\left[\mathbf{D}_H^T\mathbf{D}_H\hat{\mathbf{x}}_{\text{FUS}} + 2\mathbf{D}_V^T\mathbf{D}_V\hat{\mathbf{x}}_{\text{FUS}}\right] \equiv \mathbf{0} \tag{3.20}$$

$$\mathbf{W}_{\text{FUS}}^T\mathbf{C}_{\text{FUS}}^{-1}\mathbf{W}_{\text{FUS}}\hat{\mathbf{x}}_{\text{FUS}} + \alpha_{\text{FUS}}\left[\mathbf{D}_H^T\mathbf{D}_H + 2\mathbf{D}_V^T\mathbf{D}_V\right]\hat{\mathbf{x}}_{\text{FUS}} = \mathbf{W}_{\text{FUS}}^T\mathbf{C}_{\text{FUS}}^{-1}\mathbf{y}_{\text{FUS}}$$

$$\hat{\mathbf{x}}_{\text{FUS}} = \left(\mathbf{W}_{\text{FUS}}^T\mathbf{C}_{\text{FUS}}^{-1}\mathbf{W}_{\text{FUS}} + \alpha_{\text{FUS}}\left[\mathbf{D}_H^T\mathbf{D}_H + \mathbf{D}_V^T\mathbf{D}_V\right]\right)^{-1}\mathbf{W}_{\text{FUS}}^T\mathbf{C}_{\text{FUS}}^{-1}\mathbf{y}_{\text{FUS}} \tag{3.21}$$

$$\hat{\mathbf{x}}_{\text{FUS}} = \underbrace{\left(\mathbf{W}_{\text{FUS}}^T\mathbf{C}_{\text{FUS}}^{-1}\mathbf{W}_{\text{FUS}} + \alpha_{\text{FUS}}\mathbf{Q}\right)^{-1}\mathbf{W}_{\text{FUS}}^T\mathbf{C}_{\text{FUS}}^{-1}}_{\mathbf{\Pi}_{\text{FUS}}}\mathbf{y}_{\text{FUS}} \tag{3.22}$$

For (3.18), the vector calculus identities of (2.28) and (2.29) were used which also handles the injected Tikhonov related matrices and vectors.

3.4 Experimental Procedure

The experimental procedure consists of three parts:

1. Collecting data, i.e. $\mathbf{y}_{\text{RTI}}$ with an RTI system.

2. Collecting data, i.e. $\mathbf{y}_{\text{NRN}}$ with an AFIT NoNET node.

3. Processing the collected data to form a fused image, i.e. $\mathbf{x}_{\text{FUS}}$.

The scenes of which these two sensor technologies will be collecting for are kept roughly the same, even though simultaneous operation is not conducted. The scene will be a 252 ft^2 (18 ft by 14 ft, i.e. x ft by y ft) rectangular area within AFIT, Building 640 Laboratory 333. Conveniently, the tiles within the laboratory are squares whose sides are 1 ft, and therefore were used as a template for the construction of the rectangular area. The following subsections detail the general steps taken to set up and collect data from the two disparate sensor technologies.

3.4.1 Radio Tomographic Imaging.

3.4.1.1 Laboratory Setup.

The physical makeup of the RTI system setup for this thesis consists of 60 MEMSIC TelosB motes each spaced 1 ft apart from each other and at a height of 4 ft 5 in. An aerial view of the position of each node is shown in Figure 3.1. To achieve the desired spacing and height, each RTI node is attached to a standing structure composed of multiple 1/2 in Polyvinyl Chloride (PVC) pipes with the use of velcro straps.

Physical orientation of each TelosB mote was considered based on past work [28], [29]. Referring to the specifications [30] for the Inverted F Antenna (IFA) in the TelosB mote, orienting the motes horizontally versus vertically results in differing antenna gain patterns. However, since the premise of RTI is based on the difference in RSS,

physical orientation of the TelosB mote was not considered critical. Rather, consistency in the orientation of all TelosB motes was the imperative, with a horizontal orientation being the choice for the work in this thesis.

3.4.1.2 Software Setup.

The RTI nodes are powered and programmed through varying lengths of universal serial bus (USB) cables as shown in Figure 3.2. Programming is accomplished using Cygwin installed on a Microsoft Windows® 7 laptop. Cygwin allows programs of Unix-like systems to be recompiled and run natively on Microsoft Windows®. Each TelosB mote has the TinyOS operating system installed, providing interfaces and components for packet communication, routing, sensing and storage. For the 60 RTI nodes that make up the WSN, a TinyOS program called Spin is installed on each of them. Spin is open source program created by the Sensing and Processing Across Networks (SPAN) laboratory at the Department of Electrical Engineering in the University of Utah. Spin transmits RSS information from a WSN using a token passing protocol. With the token passing protocol, RTI nodes transmit sequentially rather than at the same time, reducing the amount of lost information packets transmitted within the WSN.

In order to receive and process the RSS data packets being transmitted from the WSN, a TinyOS program called BaseStation is installed on a single TelosB mote to be connected to the laptop. Technically, BaseStation acts as a bridge between the serial port of the laptop and the WSN, allowing a TelosB mote to listen to all the RTI nodes. Institute of Electrical and Electronics Engineers (IEEE) 802.15.14 specifies 16 channels within the 2.4 GHz unlicensed Industrial, Scientific and Medical (ISM) band [31], in 5 MHz steps, numbered 11 through 26. For this thesis, all TelosB motes are programmed to transmit and receive on channel 26, i.e. at a frequency of 2.48 GHz.

Collection and saving of the raw RSS links was done through a MATLAB® program

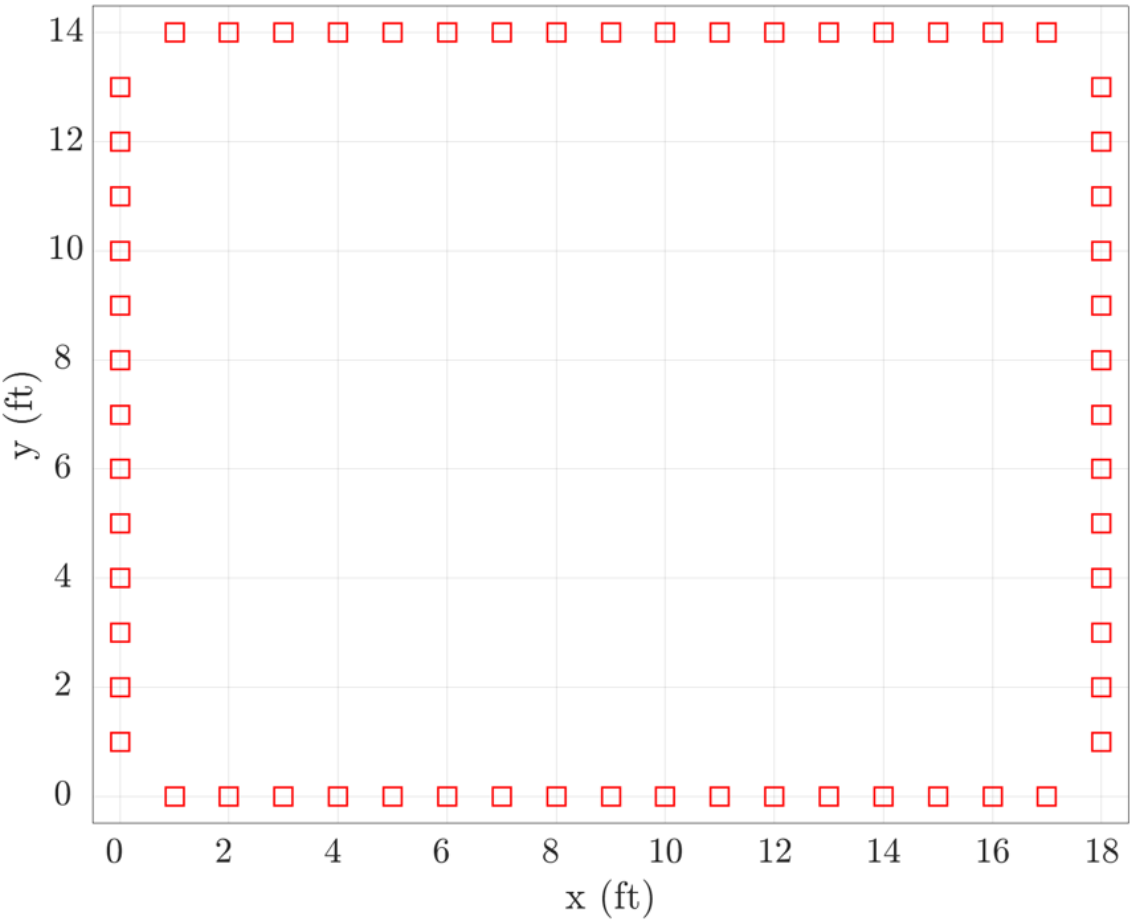

Figure 3.1. The locations of the 60 nodes shown as red boxes within the RTI WSN.

named RTI LINK Graphical User Interface (GUI) v3.1. RTI LINK GUI is a collaborative AFIT initiative designed to also display attenuation images in near-real time, parsing raw hexadecimal data from the TelosB motes, converting it to a signed integer form of link RSS. RTI LINK GUI also provides the user with options of RTI weight models and parameters, providing flexibility in comparing the impacts of Tikhonov regularization and pixel size/image resolution.

As discussed in Subsubsection 2.1.1.2, the RTI weight model and associated parameters used for this research are organized in Table 3.1.

Figure 3.2. The RTI setup used for this thesis located at AFIT, Building 640 Laboratory 333.

3.4.1.3 Calibration.

Calibration of the RTI WSN is accomplished by accumulating at least 50 frames of RSS links, or in other words, waiting until the token has passed through the entirety of the WSN at least 50 times. Calibration is taken with no targets within the WSN, with the final calibration vector being the average of the collected frames. It is this calibration vector which is used to calculate the change in RSS, i.e. $\Delta\mathbf{y}$ or $\mathbf{y}$ in (2.6).

3.4.1.4 Target Collect.

Following calibration, targets are then introduced into the WSN in which collection of frames is once again commenced. In the event of information packet loss from an

Table 3.1. RTI weight model and associated parameters.

Parameter	Choice
Binary selection matrix	$\mathbf{S}_{i,j}^{\text{Ellipse}}$
Distance between two nodes d	11.74 ft
Width of the ellipse λ	0.03 ft
Magnitude of the weights	$\mathbf{\Omega}_{i,j}^{\text{NeSh}}$
Pixel size/image resolution	1 ft

RTI node, the BaseStation records its value as not a number (NaN). As MATLAB® does not perform calculations with NaN variables, they are manually turned to a value of 0, qualitatively representing an absence of RSS.

In calculation of the final RTI attenuation image $\mathbf{x}$ in (2.6), negative values are a possible result. As negative values are not understood by MATLAB® in an image context, they are set to 0, qualitatively representing no change in RSS, or synonymously, no detection in attenuation. Finally, $\mathbf{y}_{\text{RTI}}$, i.e. the collected raw link RSS vector, is saved for later use in MSDF.

3.4.2 Noise Radar.

3.4.2.1 Software Setup.

Collection of radar data is accomplished through the use of a computer program called NoNET MKIIa installed on a Microsoft Windows® 10 laptop. NoNET MKIIa is a collaborative AFIT initiative built to interface with AFIT's noise radar hardware, allowing the user to select and specify desired parameters for transmission and reception of Ultra-wideband (UWB) signals. The parameters set for the noise radar work in this thesis are organized in Table 3.2.

Transmit and receive signals are able to be previewed and saved, allowing for post processing in MATLAB®. Post processing of the raw noise radar in MATLAB® is carried

out using a library of scripts collectively known as Air Force Institute of Technology Low Observables Radar Electromagnetics Processing INtegrated Environment (ALPINE)©. The ALPINE© MATLAB® toolbox provides both plotting and processing functions tailored to the data generated in AFIT's laboratories. The script used from ALPINE© for the work conducted in this thesis is known as "readNoNET.m". The "readNoNET.m" script essentially takes the transmit and receive waveforms and returns the impulse response, $\mathbf{y}_{\mathrm{NR}z}$ by cross correlating the two waveforms. Given the known sampling rate, capture time and the propagation speed of the signal (i.e. assumed to be the speed of light), target range estimations can then be made, influenced by the magnitude of the cross correlation.

3.4.2.2 Calibration.

All previous work with the AFIT NoNET required some form of calibration [17–19, 32–36]. Figure 3.3 highlights the amount of calibration required when using an AFIT NoNET node to take range measurements. The graph displays the measured target range made by the noise radar as the target was moved away at 5 ft increments whilst being in line-of-sight (LOS). The target used was a hollow metal cylinder 5 ft tall and 7 in in diameter. What can be inferred from Figure 3.3 is that raw range measurements are relatively linear from a true range of 0 ft to 20 ft. To explain the results for ranges greater than 20 ft, a three-dimensional (3D) plot of the measured impulse responses with background subtraction at each target range is displayed in Figure 3.4. What can be deduced from Figure 3.4 is that under the current specifications (the time at which this thesis was written) of the AFIT NoNET node, the noise radar simply cannot confidently detect and range targets of interests beyond 20 ft in a cluttered environment. The positive aspect that can be taken from these results is that a calibration procedure can be made to correct for the 23 ft error.

Table 3.2. NoNET MKIIa parameters.

Parameter	**Choice**
Transmit Input Range	2000 mV
Receive Input Range	2000 mV
Sampling Rate	3000 MHz
Capture Time	1μs
Samples per Trigger	3000
Transmit 3 dB filter	ON
Receive 3 dB filter	ON

The calibration procedure adopted for correcting the range measurements of the AFIT NoNET is called two point calibration. This calibration technique, also employed by [18], essentially rescales raw measurements and is capable of correcting both slope and offset errors. To perform two point calibration [37]:

1. Take two measurements with the noise radar using the hollow metal cylinder: One near the low end of the measurement range and one near the high end of the measurement range. Record these readings as “RawLow" and “RawHigh".

2. Repeat these measurements with a reference instrument, recording these readings as "ReferenceLow" and "ReferenceHigh". A measuring wheel was used in this instance.

3. Calculate “RawRange" as RawHigh - RawLow.

4. Calculate “ReferenceRange" as ReferenceHigh - ReferenceLow.

5. Calculate the corrected value as $\left(\frac{\left((\text{RawValue}-\text{RawLow})\times\text{ReferenceRange}\right)}{\text{RawRange}}\right)+\text{ReferenceLow}$.

Figure 3.5 displays the result of performing two point calibration on the raw range measurements collected in Figure 3.3. Thus, we are now able to employ a method of correcting range measurements for the AFIT NoNET over a reasonably linear region.

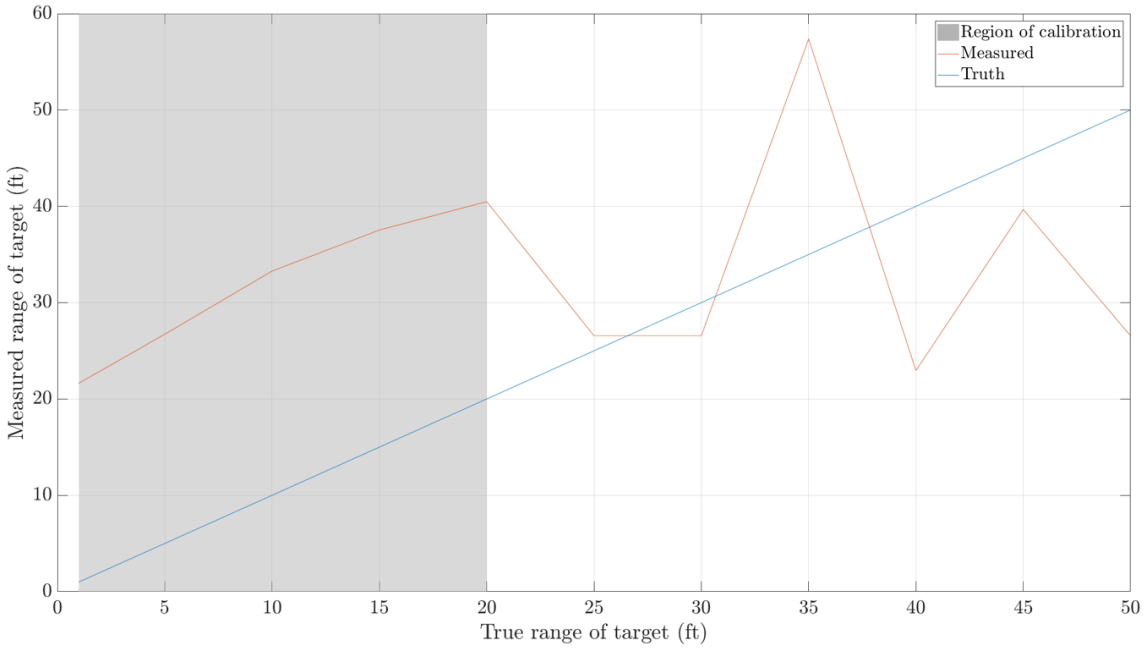

Figure 3.3. Raw AFIT NoNET node range measurements.

3.4.2.3 Polarization.

Orientation of the transmit and receive log-periodic antennas (LPAs) must be decided upon. Prior work in [17–19, 32] considered the best orientation of the LPAs for the conduct of their respective research. Figure 3.6 and 3.7 displays the various configurations of the LPAs for this thesis. The differing configurations relate to either a horizontal (HH) or vertical (VV) polarization which in turn results in different return echoes due to the antenna patterns of the LPAs. In the horizontal configuration, the receive antenna will have less cross-talk (or coupling) from the transmit antenna due to the null in the antenna pattern where the receive antenna is located [32]. However, much more energy is returned from the floor in this configuration. With the vertical polarization configuration, the antenna pattern null is pointed at the floor, minimizing returns from the floor. However, there is no null in the direction of the receive antenna, providing significant cross-talk that must be accounted for. Based on an examination

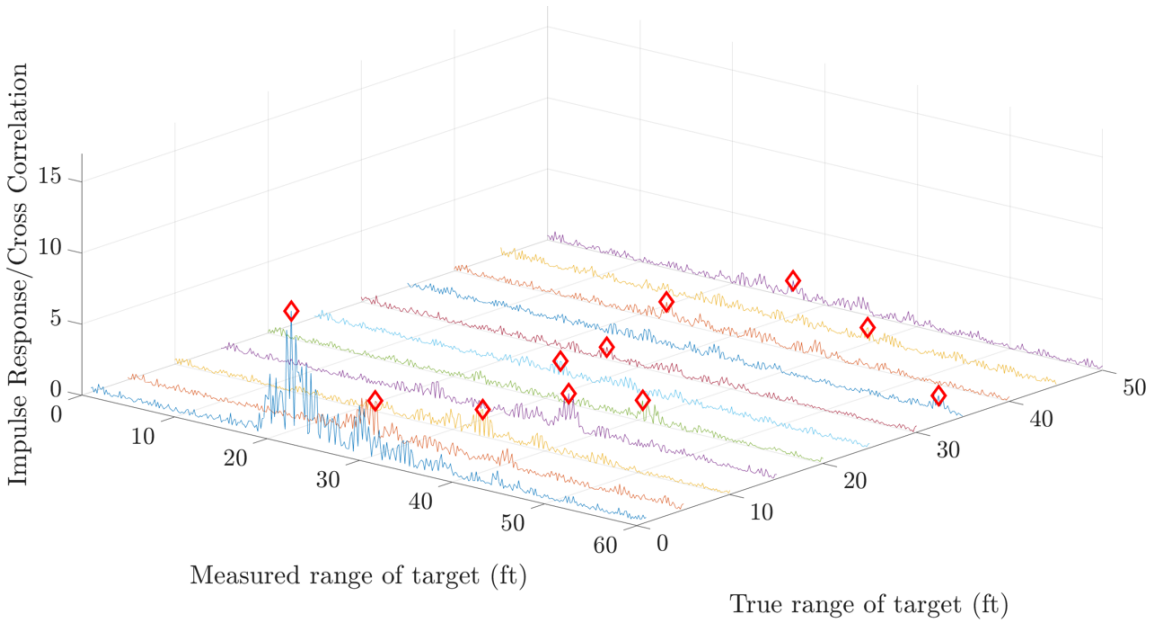

Figure 3.4. 3D plot of raw AFIT NoNET impulse responses with node range measurements.

of multiple trial experiments, maximum separation in azimuth between horizontally polarized transmit and receive LPAs was the configuration that returned correct detections from the furthest distance within the laboratory and is therefore used when collecting radar data to build $\mathbf{y}_{\mathrm{NR}z}$.

3.4.2.4 Target Collect.

With only one AFIT NoNET node available for use, data collection involved physically moving the noise radar to predetermined locations around the scene to be imaged. Trilateration is performed by transmitting and receiving from three locations as organized in Table 3.3 and shown in Figures 3.8 and 3.9.

At each location four collections will need to be made:

1. A background scene collect, absent of any targets.

2. A “RawLow" scene collect using the hollow metal cylinder, in following the instructions for two point calibration.

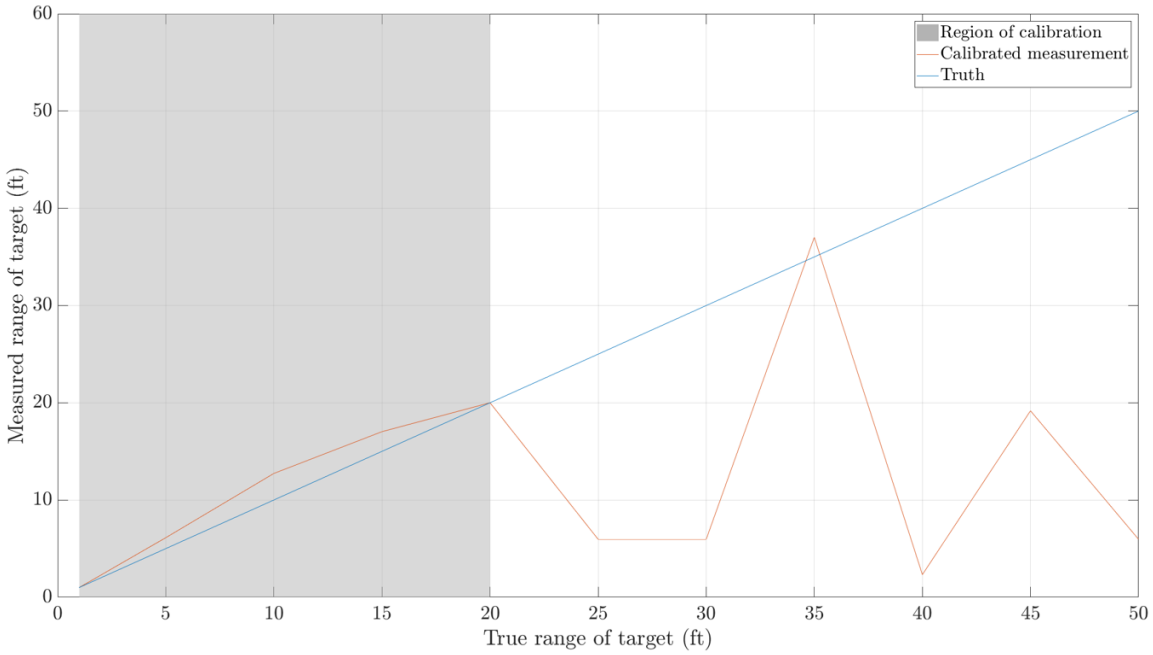

Figure 3.5. Calibrated AFIT NoNET node range measurements.

3. A “RawHigh" scene collect using the hollow metal cylinder, in following the instructions for two point calibration.

4. A target scene collect.

The purpose of the background scene collect is an effort to remove noise/clutter from the final result by subtracting it from the target scene collect. Hence, the intent is that only target information is left remaining after the expected range errors have been calibrated out. Finally, $\mathbf{y}_{\mathrm{NR}z}$, i.e. the calculated impulse response vector, is saved for later use in MSDF.

3.4.3 Multi-Sensor Data Fusion.

The final part of the experimental procedure for this thesis involves processing the saved collected data, i.e. $\mathbf{y}_{\mathrm{RTI}}$ and $\mathbf{y}_{\mathrm{NR}z}$ to form a final fused image, $\mathbf{x}_{\mathrm{FUS}}$. This is achieved with the execution of various MATLAB® scripts written using the system model defini-

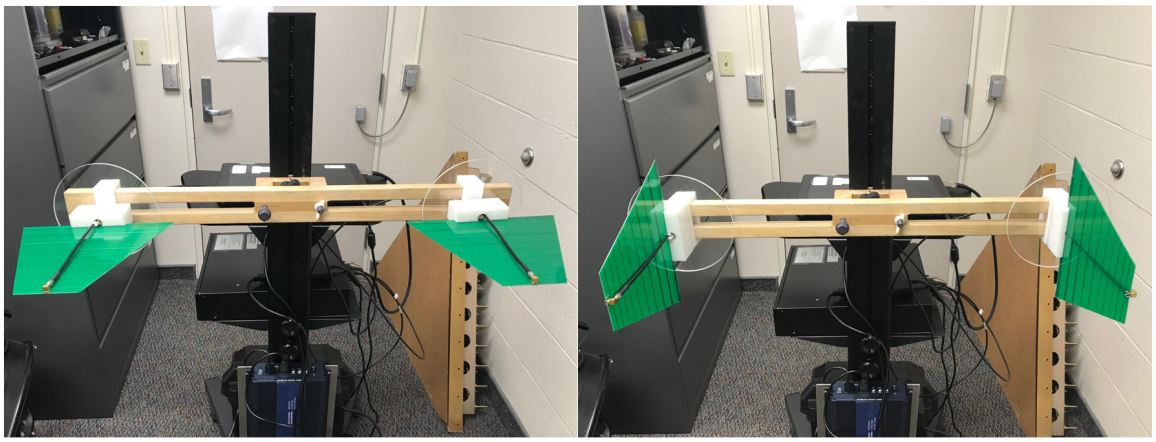

Figure 3.6. Left: Maximum separated azimuth between horizontally polarized transmit and receive (HH) LPAs. Right: Maximum separated azimuth between vertically polarized transmit and receive (VV) LPAs.

Table 3.3. NRz locations.

Coordinate Location	**Description**
(0,0)	Denoted as Noise Radar 1 (NR1)
(9,0)	Denoted as Noise Radar 2 (NR2)
(18,0)	Denoted as Noise Radar 3 (NR3)

tion proposed in Section 3.3 and solving for $\mathbf{x}_{\text{FUS}}$ using (3.22).

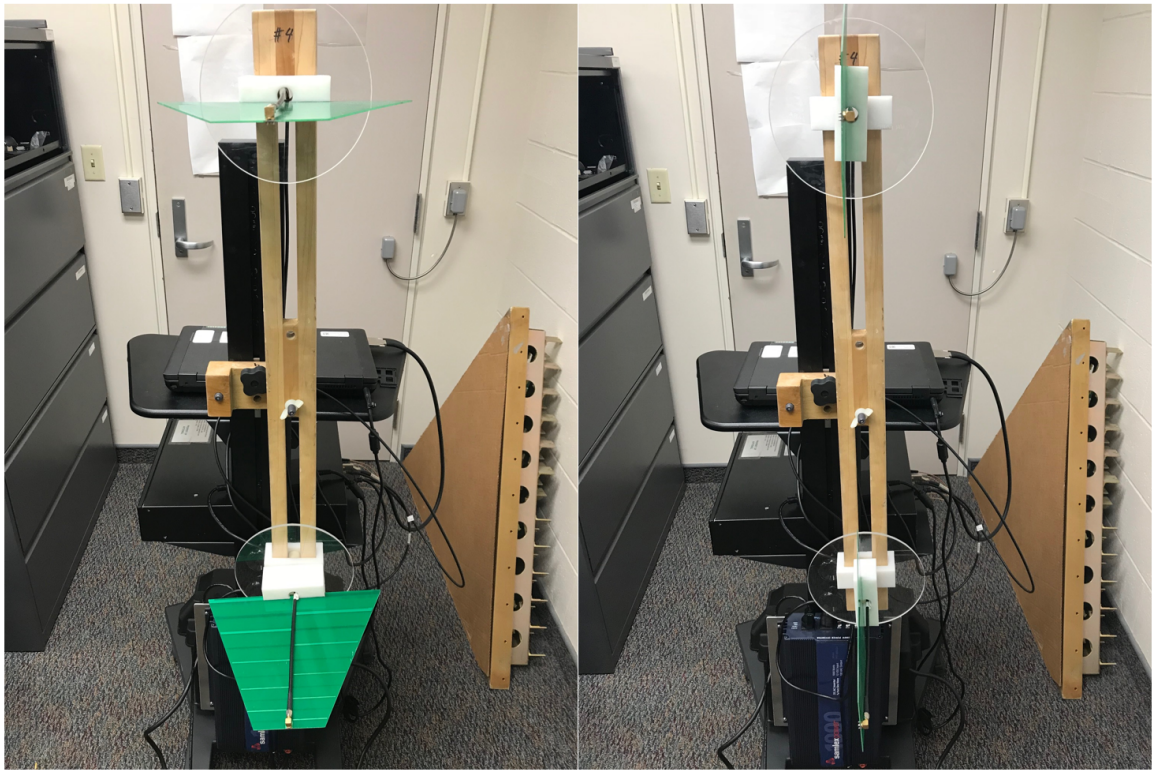

Figure 3.7. Left: Zero azimuth separation between horizontally polarized transmit and receive (HH) LPAs. Right: Zero azimuth separation between vertically polarized transmit and receive (VV) LPAs.

Figure 3.8. Left: Location of NR1. Middle: Location of NR2. Right: Location of NR3.

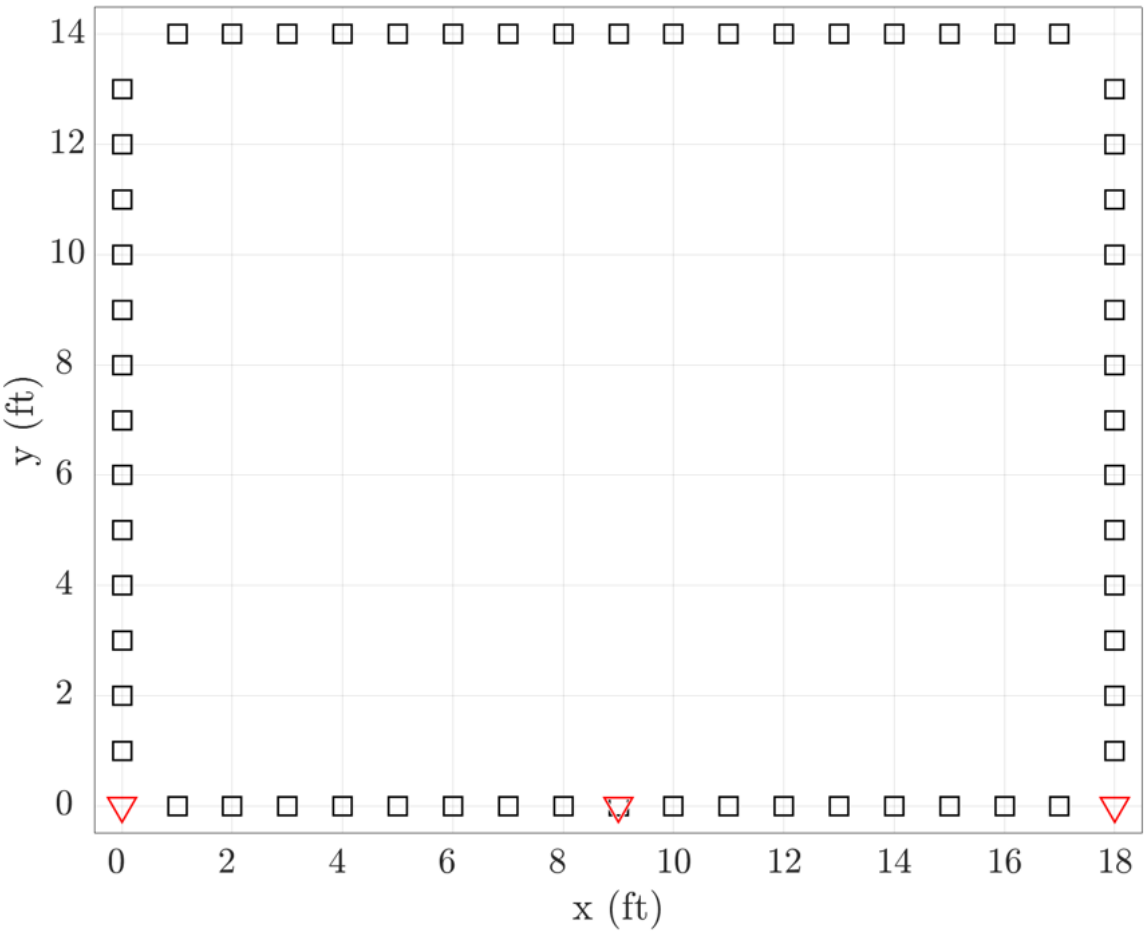

Figure 3.9. The locations of the 3 noise radars shown as red triangles amongst the RTI nodes shown as black boxes.

IV. Results & Discussion

This chapter analyzes the results obtained from following the methodology and the assumptions made in Chapter III. A 6 ft, 210 lb human target was positioned at three different locations within the scene, namely, coordinates (9,7), (4,10) and (14,4). Multiple figures and tables are created to aid in providing a full perspective on the outcome of the Multi-Sensor Data Fusion (MSDF) process. As a precursor to the upcoming sections of the chapter, the following performance metrics will be provided with each solution for $\hat{\mathbf{x}}$:

1. A maximum a posteriori (MAP) estimation.

2. K-means clustering.

3. Dispersion.

4. Comparison to a model solution.

MAP estimation, for a single target application, is a Bayesian statistic on the estimated scene $\hat{\mathbf{x}}$ which can be applied to estimate the location of the target [38]. The mathematical notation for this estimate is

$$\hat{u} = \arg\max_{n} \wp(u = n|\hat{\mathbf{x}}), \tag{4.1}$$

where $\hat{u}$ is the estimated location of the target and $\hat{\mathbf{x}}$ is the image estimate. Qualitatively, (4.1) is the pixel with the maximum intensity value. The root-mean-square error (RMSE), ϵ_{MAP}, will accompany the MAP estimation using the formula of (2.2), i.e.:

$$\epsilon_{\text{MAP}} = \frac{1}{L}\sum_{k=1}^{L}\sqrt{\left(\hat{u}_x[k]-p_x[k]\right)^2+\left(\hat{u}_y[k]-p_y[k]\right)^2}, \tag{4.2}$$

where L is the total number of samples, $\hat{u}_x[k]$ and $\hat{u}_y[k]$ are the estimated x and y coordinates at sample time k, and $p_x[k]$ and $p_y[k]$ are the known coordinates.

K-means clustering is an algorithm used by Nishida [39] to estimate single and multiple target locations with Radio Tomographic Imaging (RTI) wireless sensor networks (WSNs). K-means clustering is popular among machine learning applications, pattern recognition, hyper-spectral imagery, artificial intelligence, crowd analysis, and multiple target tracking (MTT) [40–42]. K-means clustering, or Lloyd's algorithm [43], is an iterative, data-partitioning algorithm that assigns n observations to exactly one of the k clusters defined by centroids where k is chosen before the algorithm starts. The algorithm can be summarized as follows [44]:

1. Place k cluster centers (centroids) into the spatial area represented by the pixels that are being clustered.

2. Compute point-to-cluster-centroid distances of all observations to each centroid.

3. Assign each observation to the cluster with the closest centroid.

4. Compute the average of the observations in each cluster to obtain k new centroid locations.

5. Repeat steps 2-4 until the centroid locations converge.

Separation of all points in the data set is obtained when all objects are assigned to a cluster by minimizing the euclidean distance of all the points in the data set to the centroid. Again, the RMSE, $\epsilon_{\text{Centroid}}$, will accompany the target location of the k-means clustering algorithm.

The purpose of dispersion is to find out how spread out the “target pixels" are on the two dimensional image of $\hat{\mathbf{x}}$. Another term for this statistic is a measure of spread. The “target pixels" will be revealed from the effects of thresholding and filtering $\hat{\mathbf{x}}$ when

determining the k-means performance metric. The standard deviation, σ_{Centroid}, will be the performance metric used to measure dispersion,

$$\sigma_{\text{Centroid}} = \sqrt{\frac{\sum_{j=1}^{\text{N}} \left|\kappa_j - \nu\right|^2 \cdot \hat{\chi}_j}{\sum_{j=1}^{\text{N}} \hat{\chi}_j}} \tag{4.3}$$

where N is the number of pixels in the image, κ_j is the coordinate of the jth pixel, ν are the centroid's coordinates and $\hat{\chi}_j$ is the intensity of the jth pixel of the estimated centroid filtered image. Hence σ_{Centroid} is not only a function of distance, but is also weighted by pixel intensity.

A quantitative comparison to an ideal model solution, presented in Figure 4.1, will be used to provide a fourth dimension for determining the image quality for $\hat{\mathbf{x}}$. Since imaging the location of humans is a primary goal, a model for the size, shape, and attenuation of the human body at the frequencies of interest would be required. This information is difficult to model, since it is dependent on body types, the plane of intersection, and other variables. Following [9], a human is modeled as a uniformly attenuating cylinder with radius R_{H}. In this case, the "true normalized" image $\mathbf{x}$ for a human positioned at location c_{H} can be described as

$$\mathbf{x}_{c,j} = \begin{cases} 1, & \text{if } \left\| x_j - c_{\text{H}} \right\|^2 < R_{\text{H}} \\ 0, & \text{otherwise} \end{cases} \tag{4.4}$$

where $x_{c,j}$ is the center location of pixel j. By scaling the image such that the maximum equals one, resulting in the normalized image $\hat{\mathbf{x}}_{\text{Norm}}$, we can define the RMSE of the normalized image with respect to pixel intensity to be,

$$\Psi_{\text{Ideal}} = \frac{1}{N} \sum_{j=1}^{N} \sqrt{\left|\chi_j - \hat{\chi}_{\text{Norm},j}\right|^2} \tag{4.5}$$

where N is the number of pixels in the image, χ_j is the jth pixel intensity of the truth image and $\hat{\chi}_{\text{Norm},j}$ is the jth pixel intensity of the estimated, normalized image. Figures A.1 and B.1 display the two other model solutions for the various target locations undertaken in this research.

4.1 Radio Tomographic Imaging

This section explores the results of the collections taken with the RTI sensor following the methodology laid out in Subsection 3.4.1.

4.1.1 Empirical Covariance.

In accordance with (3.5), a covariance matrix, $\mathbf{C}_{\text{RTI}}$, for the RTI sensor technology needs to be determined. $\mathbf{C}_{\text{RTI}}$ is a matrix whose element in the i,j position is the covariance of between the i-th and j-th element of the RTI noise vector, $\mathbf{n}_{\text{RTI}}$. For the sake of transparency, if the entries in the column vector

$$\mathbf{n}_{\text{RTI}} = \begin{bmatrix} y_{1,\text{No Targets}} - y_{1,\text{Calibration}} \\ \vdots \\ y_{M,\text{No Targets}} - y_{M,\text{Calibration}} \end{bmatrix} = \begin{bmatrix} n_{\text{RTI},1} \\ \vdots \\ n_{\text{RTI},M} \end{bmatrix},$$

then the covariance matrix is

$$\begin{aligned}
[\mathbf{C}_{\text{RTI}}]_{i,j} &= \mathbb{E}\big[\big(n_{\text{RTI},i} - \mu_i\big)\big(n_{\text{RTI},j} - \mu_j\big)\big] \\
&= \mathbb{E}\big[\mathrm{n}_{\text{RTI},i}\mathrm{n}_{\text{RTI},j} - \mathrm{n}_{\text{RTI},i}\mu_j - \mu_i\mathrm{n}_{\text{RTI},j} + \mu_i\mu_j\big] \\
&= \mathbb{E}\big[\mathrm{n}_{\text{RTI},i}\mathrm{n}_{\text{RTI},j}\big] - \mathbb{E}\big[\mathrm{n}_{\text{RTI},i}\mu_j\big] - \mathbb{E}\big[\mu_i\mathrm{n}_{\text{RTI},j}\big] + \mathbb{E}\big[\mu_i\mu_j\big] \\
&= \mathbb{E}\big[\mathrm{n}_{\text{RTI},i}\mathrm{n}_{\text{RTI},j}\big] - \mu_i\mu_j - \mu_i\mu_j + \mu_i\mu_j \\
&= \mathbb{E}\big[n_{\text{RTI},i}n_{\text{RTI},j}\big] - \mu_i\mu_j,
\end{aligned}$$

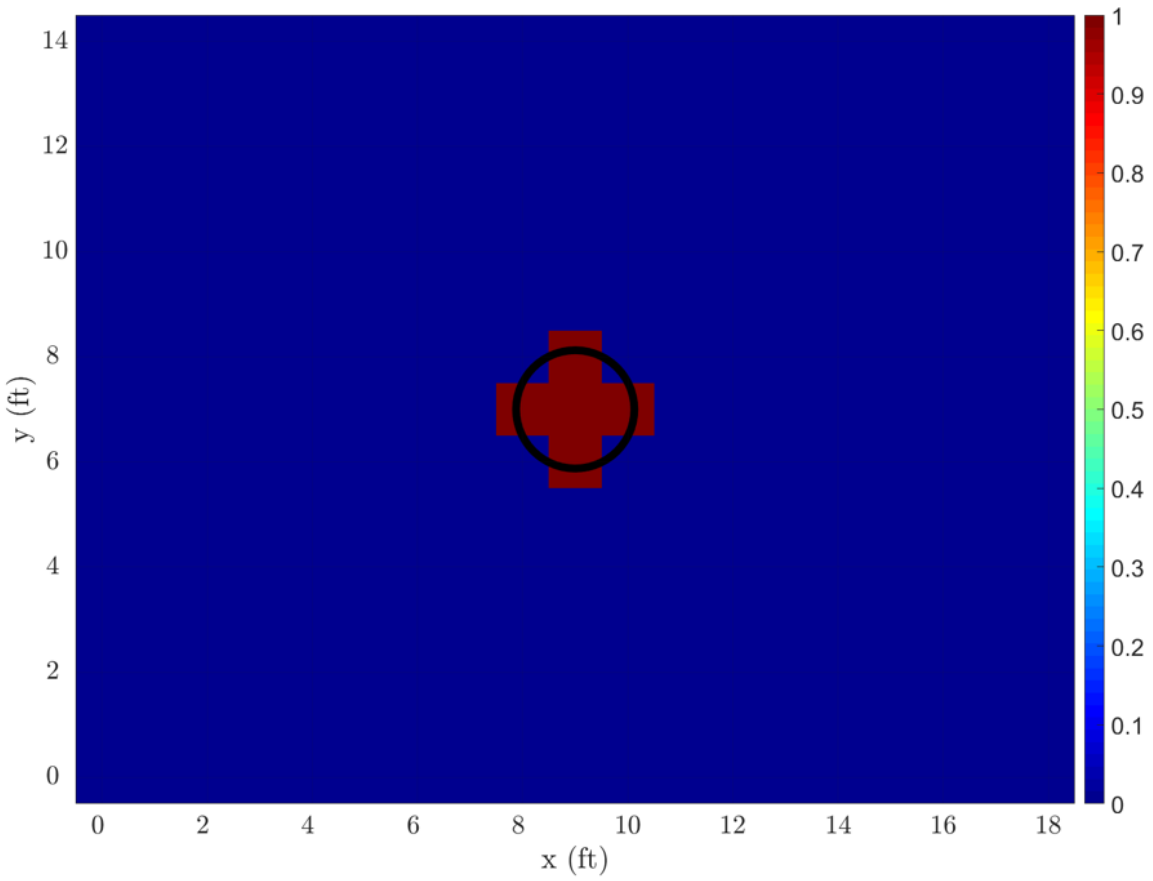

Figure 4.1. A model solution to be used for the performance metric, Ψ_{Ideal}, with target at (9,7).

where the operator $\mathbb{E}$ denotes the expected value or mean of its argument, and

$$\mu_i = \mathbb{E}\left(n_{\text{RTI},i}\right),$$

is the expected value of the i-th entry in the vector $\mathbf{n}_{\text{RTI}}$.

Up to 300 frames of link received signal strength (RSS) data of an empty scene were collected in order to calculate an empirical $\mathbf{C}_{\text{RTI}}$. Using the MATLAB® function "cov()" an empirical RTI covariance matrix was produced as shown on the left in Figure 4.2. As $\mathbf{C}_{\text{RTI}}$ will need to be inverted for the calculation of the final attenuation image, the empirical covariance matrix was not. Thus an approximation was made for it to be invertible. As displayed in Figure 4.3, inspection of a histogram of the off-diagonal

elements of the empirical matrix revealed that they were close to 0, and as such were reset to 0. Similarly, a histogram of the diagonal elements is also displayed in Figure 4.3, and were all reset to the average of the diagonal elements in the empirical covariance matrix. This approximation results in an approximated empirical covariance matrix expressed in the form of a constant multiplied against an identity matrix, i.e. $\sigma^2\mathbf{I}$. The result is shown on the right in Figure 4.2. Notice that a covariance matrix of the form $\sigma^2\mathbf{I}$ effectively cancels itself out in the final solution for $\hat{\mathbf{x}}_{\text{RTI}}$ as assumed and derived in Subsection 2.1.2.

4.1.2 Tikhonov Regularized Solution.

For a human target at coordinate (9,7), Figure 4.4 displays the Tikhonov regularized solution for $\hat{\mathbf{x}}_{\text{RTI}}$ following the procedure laid out in Subsection 3.4.1. For the sake of simplicity, the Tikhonov regularization parameter $\alpha = 8$ was subjectively chosen to create the image. The white and black overlapping squares on the edge of the scene are the locations of individual RTI nodes with the human target represented by the black circle. Indeed, RTI as a sensor technology was able to detect the target as well as display its darkest pixel at the correct coordinate, however there is obvious uncertainty represented by the spread of dense pixel shading covering a relatively larger area than what the human target actually would.

4.1.2.1 Performance Metrics.

In the left of Figure 4.5 is a histogram with 30 bins containing the pixel intensities in the RTI Tikhonov regularized solution of Figure 4.4. A normal distribution is able to be fit around the data. In order to identify a cluster of pixels, a threshold on the pixels of a solution for $\hat{\mathbf{x}}$ is subjectively determined. Qualitatively, the threshold represents the intensity required by any pixels to retain its value in the image. If a pixel's inten-

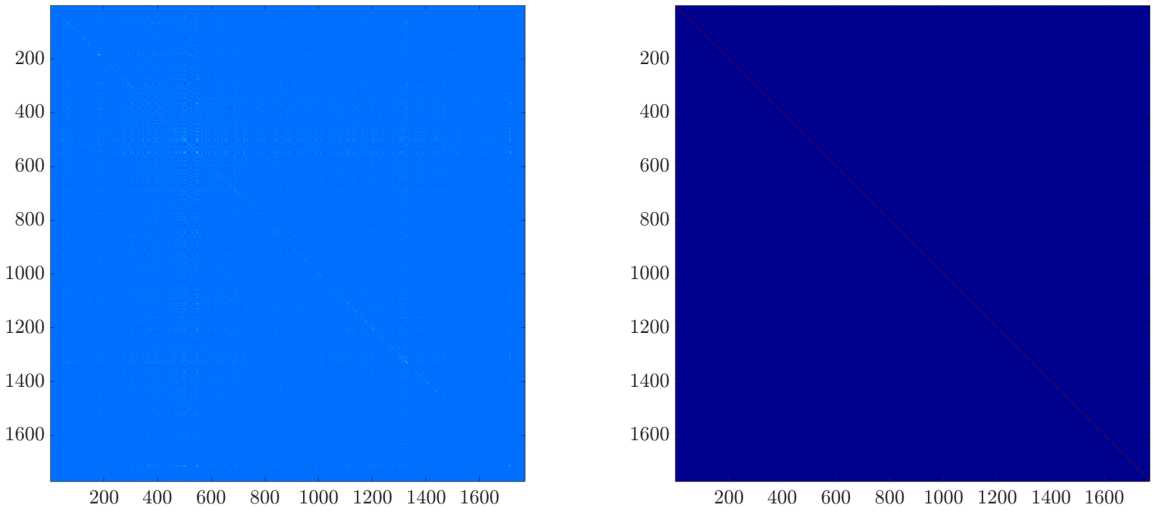

Figure 4.2. Left: The raw empirical RTI covariance matrix. Right: The approximated empirical RTI covariance matrix.

sity falls below the threshold, the pixel is considered insignificant and is consequently nulled. Work done by Nishida [39] utilized a cluster threshold, T_C, of 3σ, where σ is the standard deviation of the pixel intensities in the image solution $\hat{\mathbf{x}}$. This threshold is dependent on the Tikhonov regularization parameter, α and the pixel size/image resolution; both different to that used in this thesis work.

As a result, in the context of statistics, following the 68-95-99.7 rule (also known as the empirical rule) a threshold of, $T_C = \mu + \sigma$ was used, whose effect on the original solution of $\hat{\mathbf{x}}_{RTI}$ is shown on the top right of Figure 4.5. A threshold of $T_C = \mu + \sigma$ statistically represents one standard deviation away from the mean, quantitatively removing 68% of the pixel intensities, leaving the remaining 32% of the pixels to be assigned to k centroid/s.

K-means clustering is performed using the MATLAB® function “kmeans()" by providing the x and y coordinates of the pixels intensities above the threshold, T_C as well as the number of clusters, k. In this case, $k = 1$. The MATLAB® function “kmeans()" uses the squared Euclidean distance measure with the k-means++ algorithm [45] for

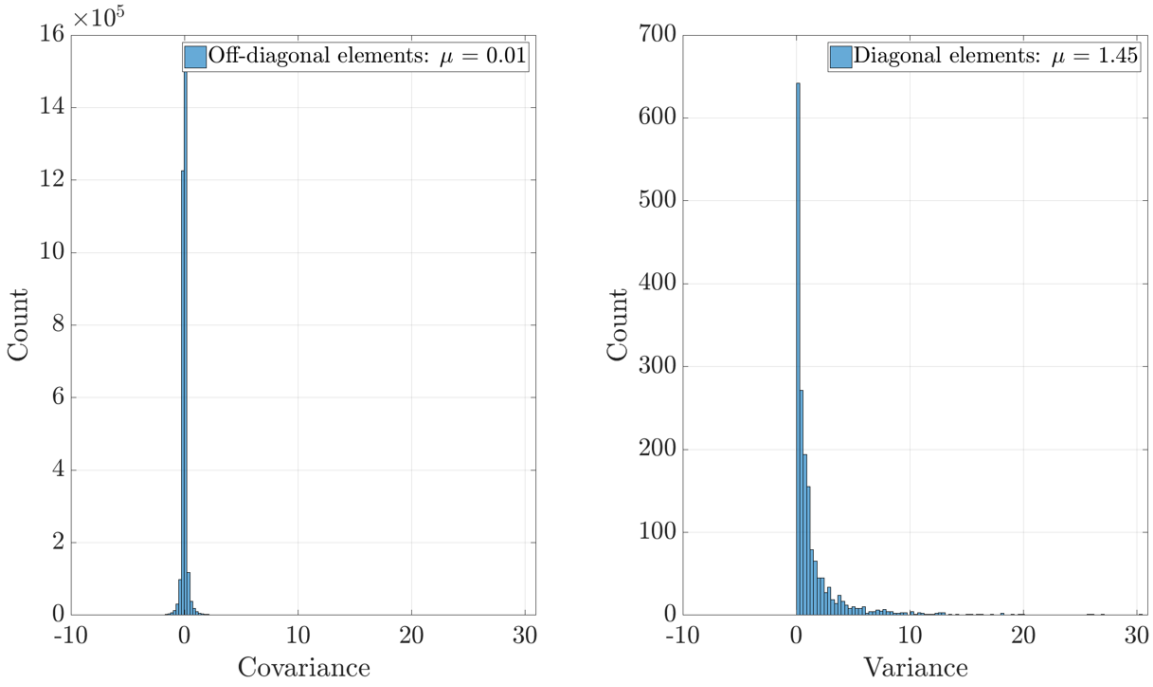

Figure 4.3. Left: Histogram of the off-diagonals in the raw empirical RTI covariance matrix. Right: Histogram of the diagonal in the raw empirical RTI covariance matrix.

cluster center initialization. In short, the k-means++ algorithm selects a pixel coordinate uniformly at random, identifying it as a possible centroid. Its distance from every other provided pixel coordinate is then computed. This process repeats itself, until all pixel coordinates serve as a possible centroid, with the best centroid being chosen on the grounds of shortest distance measurements. As can be seen from the top right of Figure 4.5, the centroid location represented by the asterisk, was computed to be at coordinate (9.25,5.14).

To avoid the bias presented by pixels that identify as outliers, a 3 ft radius is set around the initial centroid location as shown in the top right of Figure 4.5. The white dashed circle acts as a filter, filtering out any pixels outside the circumference of the circle. The k-means algorithm is again applied on the remaining pixels, with the new, filtered centroid location at coordinate (9.41,5.28).

Figures A.2 and B.2 display the results of the human target at (4,10) and (14,4) re-

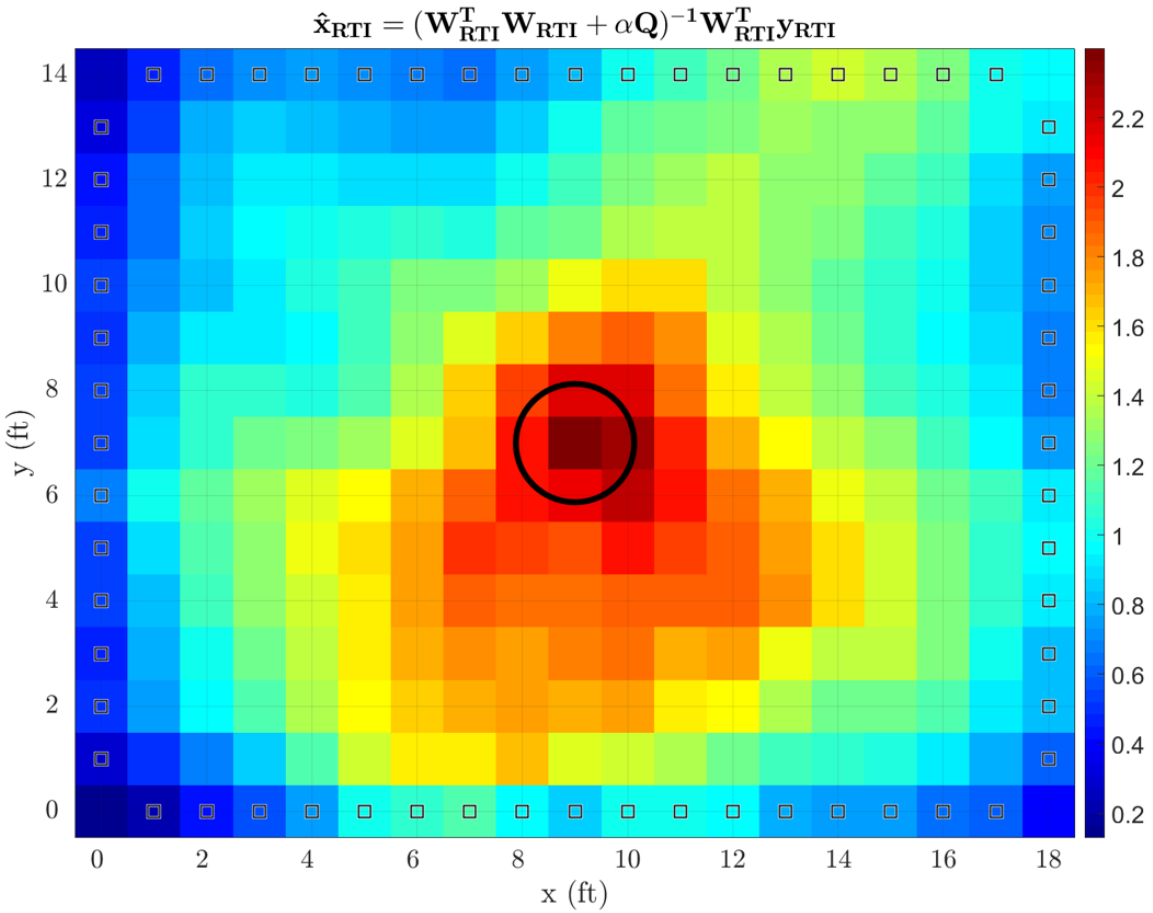

Figure 4.4. The AFIT RTI image with target at coordinate (9,7). The regularization parameter α has subjectively been set to 8.

spectively. The performance metrics for all the RTI Tikhonov regularized solutions are organized in Table 4.1.

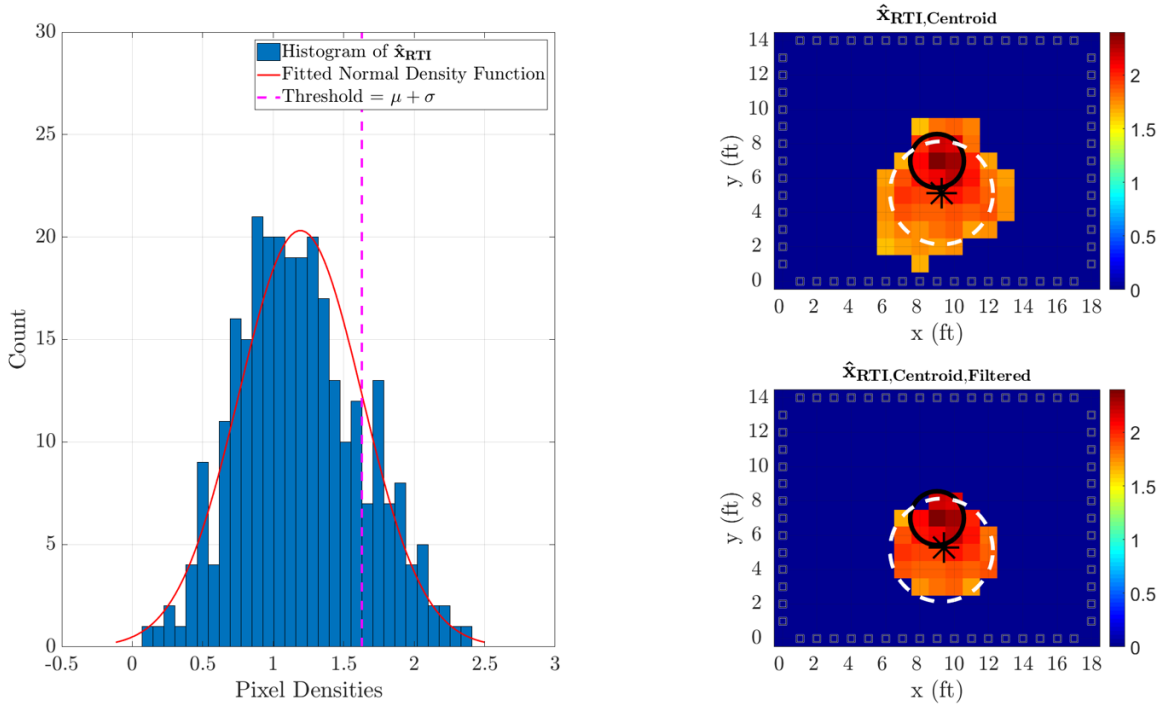

Figure 4.5. Left: Histogram of the pixel densities in $\hat{\mathbf{x}}_{\text{RTI}}$ from Figure 4.4. Right: Top - The resultant image from thresholding $\hat{\mathbf{x}}_{\text{RTI}}$ and the location of the centroid; Bottom - Filtering $\hat{\mathbf{x}}_{\text{RTI,Centroid}}$ by keeping the pixels inside the circumference of the dotted circle and reapplying the k-means algorithm.

Table 4.1. Performance metrics for the RTI Tikhonov regularized solution with targets at (9,7), (4,10) and (14,4).

Target Location	Performance Metric	Description	Result
(9,7)	MAP estimate	Coordinates of the most intense pixel.	(9,7) $\epsilon_{\text{MAP}} = 0$ ft
	K-means clustering	Coordinates of the centroid.	*Unfiltered* (9.25,5.14) $\epsilon_{\text{Centroid}} = 0.83$ ft
			Filtered (9.41,5.28) $\epsilon_{\text{Centroid,Filt}} = 0.83$ ft
	Dispersion	Pixel spread about the filtered centroid.	$\sigma_{\text{Centroid}} = 2.09$ ft
	Model solution	Compared to Figure 4.1.	$\Psi_{\text{Ideal}} = 0.53$
(4,10)	MAP estimate	Coordinates of the most intense pixel.	(4,10) $\epsilon_{\text{MAP}} = 0$ ft
	K-means clustering	Coordinates of the centroid.	*Unfiltered* (4.67,10.49) $\epsilon_{\text{Centroid}} = 1.88$ ft
			Filtered (4.72,10.41) $\epsilon_{\text{Centroid,Filt}} = 1.77$ ft
	Dispersion	Pixel spread about the filtered centroid.	$\sigma_{\text{Centroid}} = 2.12$ ft
	Model solution	Compared to Figure 4.1.	$\Psi_{\text{Ideal}} = 0.92$
(14,4)	MAP estimate	Coordinates of the most intense pixel.	(14,5) $\epsilon_{\text{MAP}} = 1$ ft
	K-means clustering	Coordinates of the centroid.	*Unfiltered* (12.81,3.94) $\epsilon_{\text{Centroid}} = 1.19$ ft
			Filtered (12.77,3.69) $\epsilon_{\text{Centroid,Filt}} = 1.27$ ft
	Dispersion	Pixel spread about the filtered centroid.	$\sigma_{\text{Centroid}} = 1.99$ ft
	Model solution	Compared to Figure 4.1.	$\Psi_{\text{Ideal}} = 0.99$

4.2 Noise Radar

This section reveals and discusses the various AFIT Noise Network (NoNET) measurements made in order to arrive at the final backscatter/reflection image, $\hat{\mathbf{x}}_{\text{NRN}}$, following the methodology laid out in Subsection 3.4.2.

4.2.1 Range Resolution.

In order to construct the weight model for trilateration (3.3), as derived in Section 3.2, the range resolution of an AFIT NoNET node needs to be determined. To accomplish this, the noise radar was configured in accordance with Table 3.2, transmitting and collecting for 20 triggers. The 20 triggers were averaged in the time domain with the result examined in the frequency domain as shown in Figure 4.6. The gray section of the graph highlights the 3 dB bandwidth of the noise radar's averaged transmit waveform, evaluated as 374 MHz. The 3 dB bandwidth was determined by following a few steps. First, the peak magnitude in the frequency domain was identified. This peak magnitude was then used to determine the upper and lower limits of the bandwidth. The upper limit of the bandwidth was found by starting at the end of the frequency spectrum (1500 MHz) and sweeping to the left towards the peak until the desired magnitude was flagged for the first time. The frequency at which the desired magnitude was located at, was denoted as the upper limit. The process of finding the lower limit of the bandwidth was identical to finding the upper limit, with the exception that the search started at the beginning of the frequency spectrum (0 MHz), sweeping to the right towards the peak until the desired magnitude was flagged for the first time.

Using (2.34), the range resolution used for the creation of the following backscat-

ter/reflection images was calculated to be

$$\begin{aligned}\Delta R &= \gamma \frac{c}{2B} \\ &= (1)\frac{c}{2(374\times 10^6)} \\ &= 0.4008 \text{ m} \\ &= 1.3149 \text{ ft.}\end{aligned} \tag{4.6}$$

4.2.2 Impulse Responses (Cross Correlations).

To justify the assumption for a normal distribution of the impulse response/cross correlation vectors, $\mathbf{y}_{\mathrm{NR}z}$ as per (3.1), a histogram of $\mathbf{y}_{\mathrm{NR1}}$ is displayed in Figure 4.7. As can be concluded, a normal distribution is a sufficient fit for the data contained within $\mathbf{y}_{\mathrm{NR1}}$ with similar results found for $\mathbf{y}_{\mathrm{NR2}}$ and $\mathbf{y}_{\mathrm{NR3}}$.

Figure 4.8 is one example of the many impulse responses/cross correlations calculated from the various transmit and receive locations for the noise radar as planned in Table 3.3. In the instance of Figure 4.8, the noise radar was situated at coordinate (18,0). Referring to the experimental procedure outlined in Subsubsection 3.4.2.4, a background collect and a target collect are shown on the right and left, respectively, of Figure 4.8.

Impulse responses were generated by using the “readNoNET.m" script from the Air Force Institute of Technology Low Observables Radar Electromagnetics Processing INtegrated Environment (ALPINE)© MATLAB® toolbox as instructed in Subsubsection 3.4.2.1. In detail, “readNoNET.m" takes the however many raw transmitted signal triggers, x_n, and cross correlates them with the corresponding amount of raw received

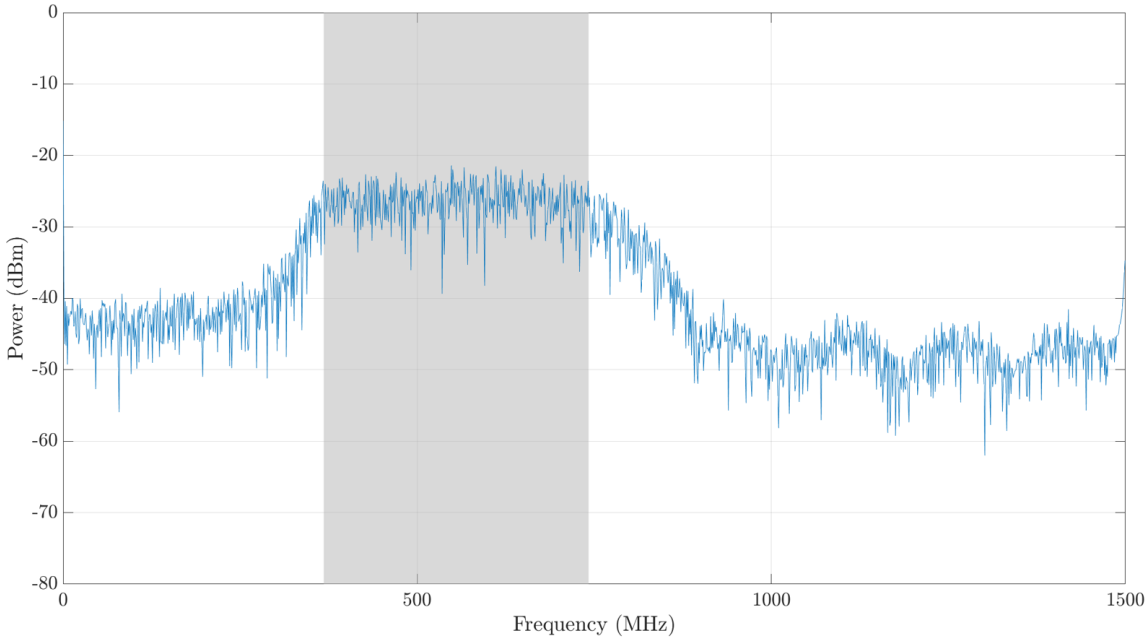

Figure 4.6. An AFIT NoNET node's transmit frequency spectrum whose 3dB bandwidth is shaded in gray. The 3dB bandwidth was found to be 374MHz.

signal triggers, y_n, using the MATLAB® function "xcorr", i.e.

$$R_{xy}(m) = \frac{1}{N} \sum_{n=0}^{N-m-1} x_{n+m} y_n^* \quad m \geq 0, \tag{4.7}$$

where N is the number of samples per trigger as indicated in Table 3.2 and the asterisk in y_n^* denotes the complex conjugation. Note that correlation requires normalization to produce an accurate estimate, and thus "readNoNET.m" accounts for this by including the $1/N$ term in (4.7).

In an effort to reduce the presence of irregular results, the output of the however many cross correlated triggers are averaged, and its absolute value is taken, with final results being displayed in a similar fashion to Figures 4.8 and 4.9. Finally, as discussed in Subsubsection 3.4.2.4, the impulse response of the background collect is subtracted from the impulse response of the target collect shown in Figure 4.9. A dominant peak can be clearly distinguished in Figure 4.9 which does in fact indicate an uncalibrated

distance of a target away from the noise radar. Following the appropriate application of two point calibration outlined in Subsubsection 3.4.2.2, the calibrated, target impulse responses will be used to create the backscatter/reflection images.

4.2.3 Trilateration Solution.

The results of this section utilizes the the impulse responses calculated back in Subsection 4.2.2 to overlay numerous “range rings" in order to form backscatter/reflection images such as those displayed in Figures 4.10 and 4.11. As discussed in Section 3.1, this concept of “range rings" works on a geometric process called trilateration, using the geometry of circles to determine relative locations of points. As there is an associated range resolution when using an AFIT NoNET node, the circles are treated as rings, where the thickness of the ring is bounded by the empirical range resolution (4.6). It is the magnitudes of the impulse response that determine the pixel shading intensity of the ring. The equation

$$\hat{\mathbf{x}}_{\mathrm{NR}z} = \mathbf{W}_{\mathrm{NR}z}^{\mathrm{T}} \mathbf{y}_{\mathrm{NR}z}, \tag{4.8}$$

represents this notion of overlaying “range rings", with the matrix $\mathbf{W}_{\mathrm{NR}z}^{\mathrm{T}}$ being the key enabler for trilateration as derived in (3.3). Given the system model definition of (3.5), (4.8) crudely assumes $\mathbf{W}_{\mathrm{NR}z}^{\mathrm{T}} \mathbf{W}_{\mathrm{NR}z}$ results in an identity matrix $\mathbf{I}$, i.e.

$$\begin{aligned}
\mathbf{y}_{\mathrm{NR}z} &= \mathbf{W}_{\mathrm{NR}z} \mathbf{x}_{\mathrm{NR}z} + \mathbf{n}_{\mathrm{NR}z} \\
\mathbf{W}_{\mathrm{NR}z}^{\mathrm{T}} \mathbf{y}_{\mathrm{NR}z} &= \mathbf{W}_{\mathrm{NR}z}^{\mathrm{T}} \mathbf{W}_{\mathrm{NR}z} \mathbf{x}_{\mathrm{NR}z} + \mathbf{W}_{\mathrm{NR}z}^{\mathrm{T}} \mathbf{n}_{\mathrm{NR}z} \\
\mathbf{W}_{\mathrm{NR}z}^{\mathrm{T}} \mathbf{y}_{\mathrm{NR}z} &\approx (\mathbf{I}) \mathbf{x}_{\mathrm{NR}z} \qquad (4.9) \\
\hat{\mathbf{x}}_{\mathrm{NR}z} &= \mathbf{W}_{\mathrm{NR}z}^{\mathrm{T}} \mathbf{y}_{\mathrm{NR}z}, \qquad (4.10)
\end{aligned}$$

which is technically not the case.

Note that by using range rings, the assumption is made that the transmitter/re-

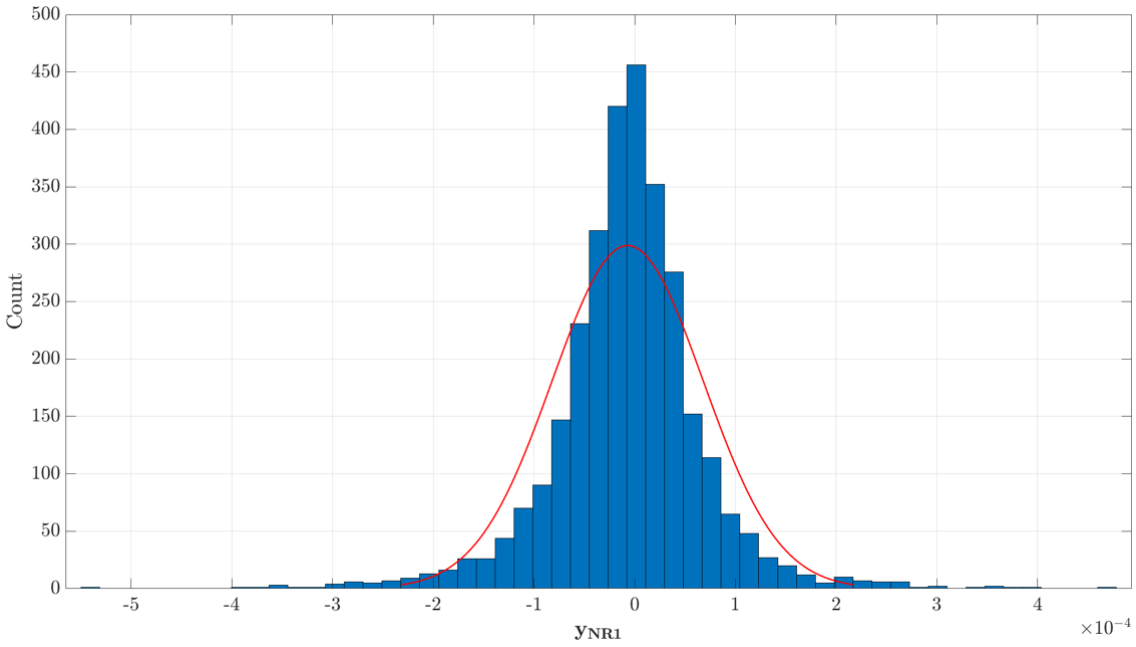

Figure 4.7. Histogram of $\mathbf{y}_{NR1}$.

ceiver are omnidirectional given that the antenna's used in this thesis are log-periodic antennas (LPAs). Figure 4.10 displays an AFIT NoNET node, i.e. Noise Radar 1 (NR1), as a black and white triangle at (0,0) with the target symbolized by the black circle at (9,7). Judging from the pixel density of the range rings, a target detection is declared close to the target. We can also declare the effects of multipath by the presence of less intense range rings in Figure 4.10, meaning that not all reflections off the target take the path directly back to the receiver. The same procedure is applied for Noise Radar 2 (NR2) and Noise Radar 3 (NR3) with the results shown in Figure 4.11.

What can be considered as a prelude to MSDF, a primitive method of fusing the three noise radars to effectively represent the final AFIT NoNET image is obtained by mathematically "stacking" the $\mathbf{W}_{NRz}$ matrices to create a Noise Radar Network (NRN) matrix, $\mathbf{W}_{NRN}$; as well as stacking the $\mathbf{y}_{NRz}$ impulse response vectors to create a NRN vector, $\mathbf{y}_{NRN}$ as planned in (3.2). The result is shown in Figure 4.12 with the most intense pixel shading appearing near the target's coordinates. Remnants of the range rings

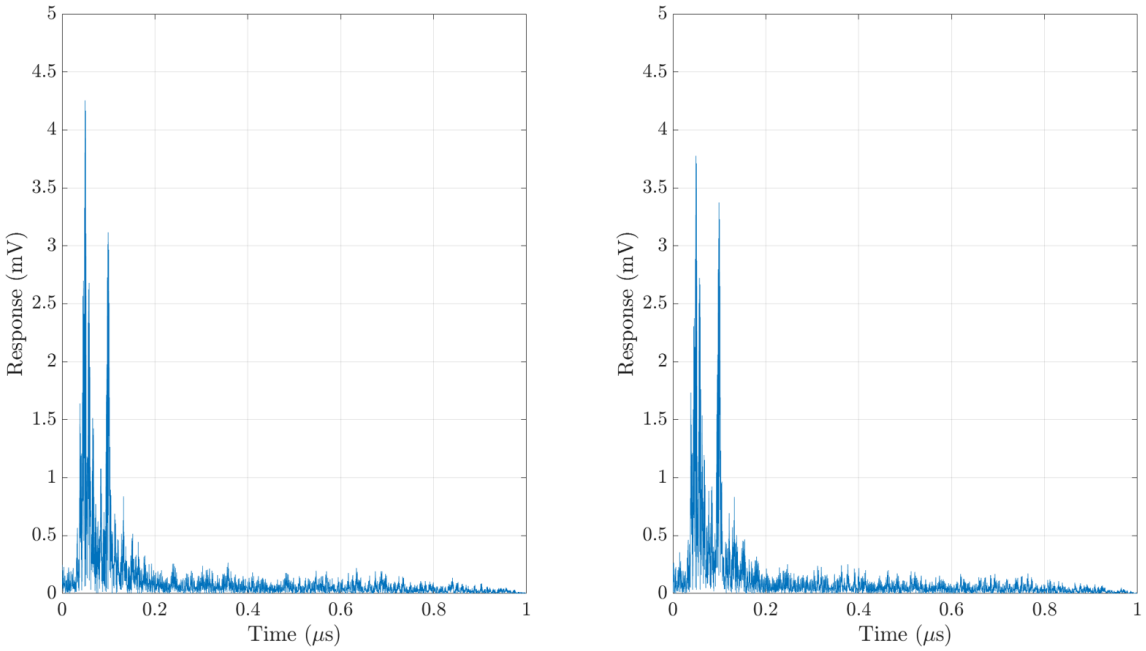

Figure 4.8. Left: The absolute value of the average impulse response/cross correlation with a target approximately 11.4 ft away from the AFIT NoNET node. Right: The absolute value of the average impulse response/cross correlation of the background scene (i.e. no target present).

produced by NR2 are present in Figure 4.12 due to the fact that this particular AFIT NoNET node was closest to the target and returned a relatively larger impulse response in magnitude compared to that of NR1 and NR3.

4.2.3.1 Performance Metrics.

Figure 4.13 displays a 30 bin histogram of the AFIT NoNET trilateration solution of Figure 4.12 as well as the location of the centroid. Figures A.3 and B.3 display the results of the human target at (4,10) and (14,4) respectively. The performance metrics for all the NRN trilateration solutions are organized in Table 4.2.

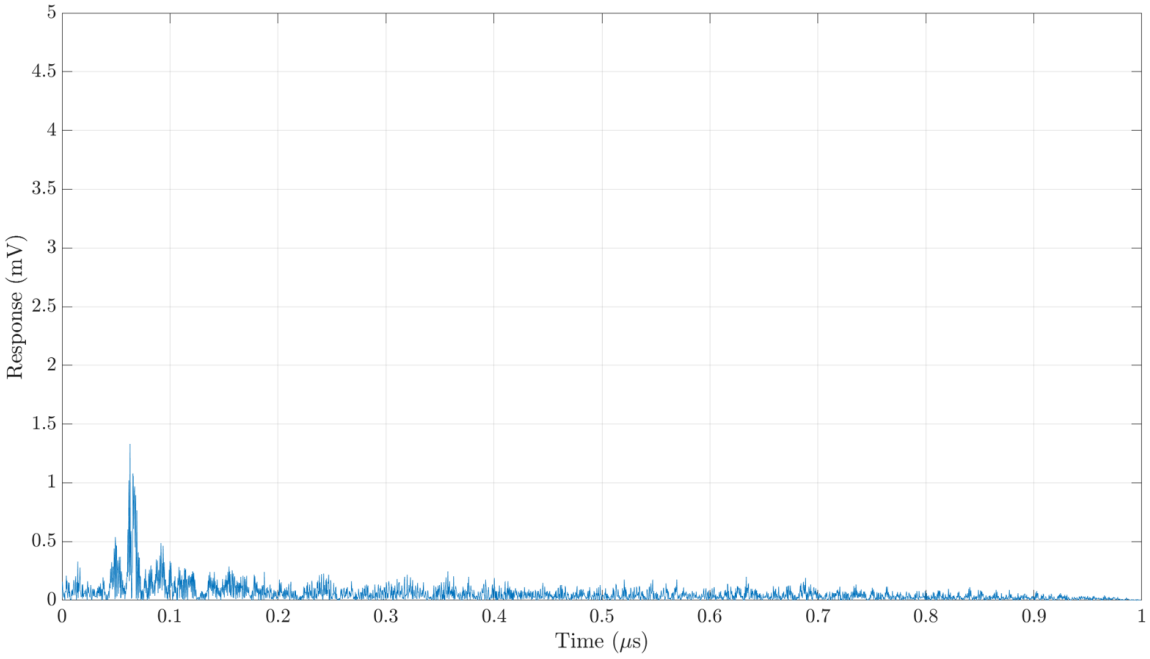

Figure 4.9. The absolute value of the average impulse response/cross correlation with a target approximately 11.4 ft away from the AFIT NoNET node with background subtraction.

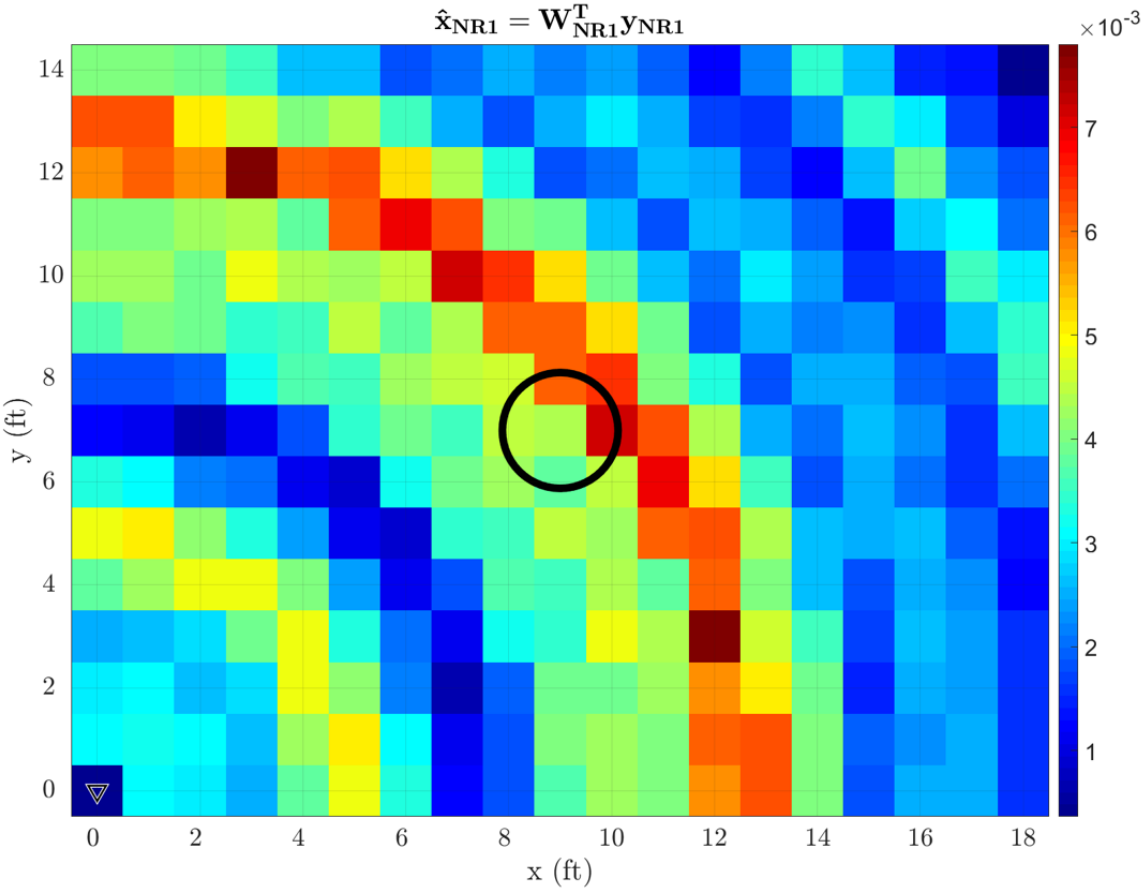

Figure 4.10. NR1 transmitting/receiving from coordinate (0,0) with target at coordinate (9,7).

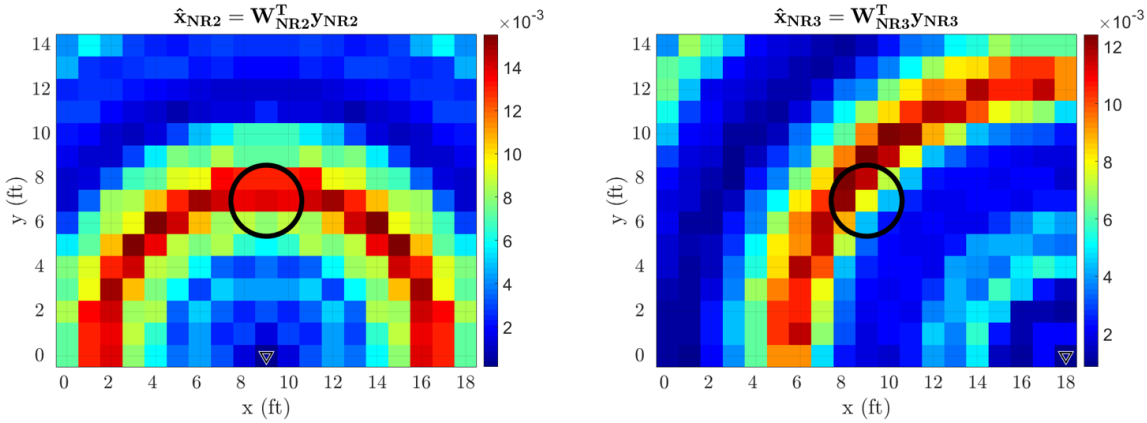

Figure 4.11. NR2 (left) and NR3 (right) transmitting/receiving from coordinates (9,0) and (18,0) respectively with target at coordinate (9,7).

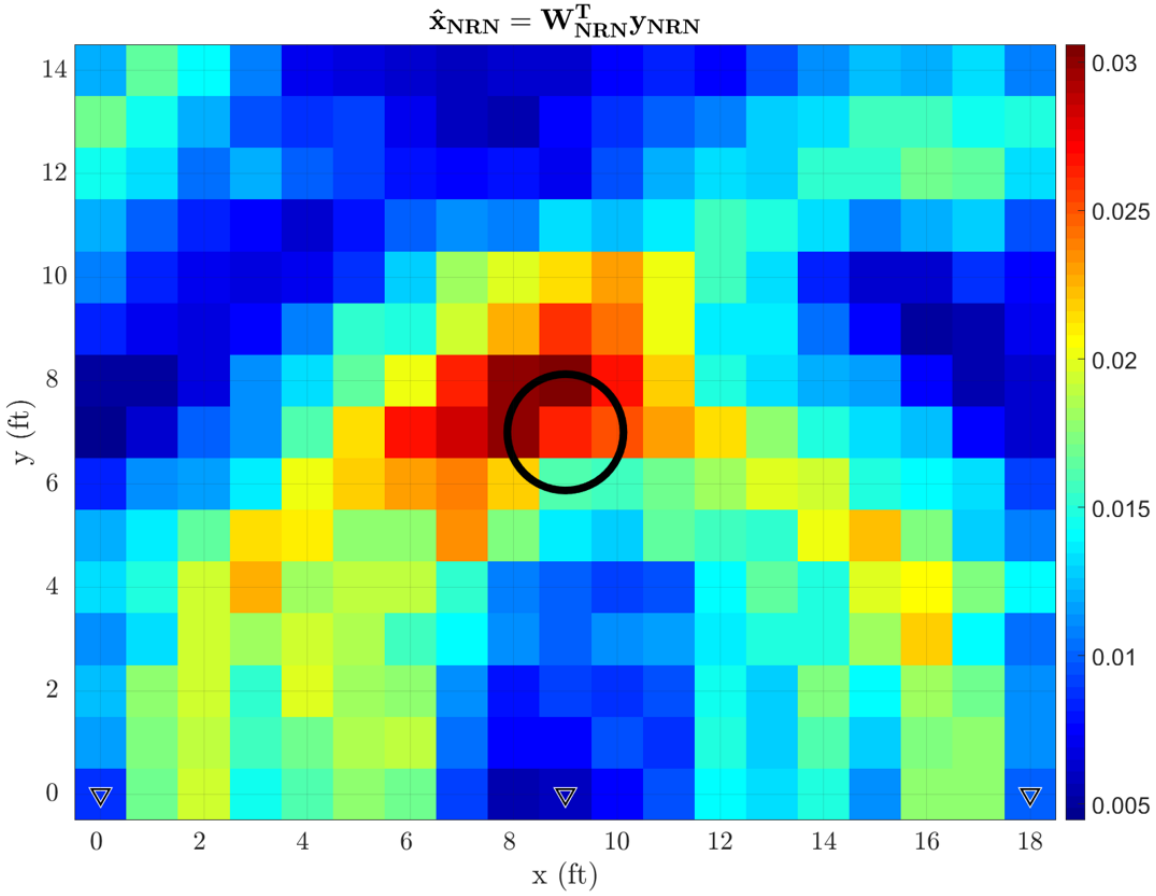

Figure 4.12. NRN transmitting/receiving from coordinates (0,0), (9,0) and (18,0) with target at coordinate (9,7).

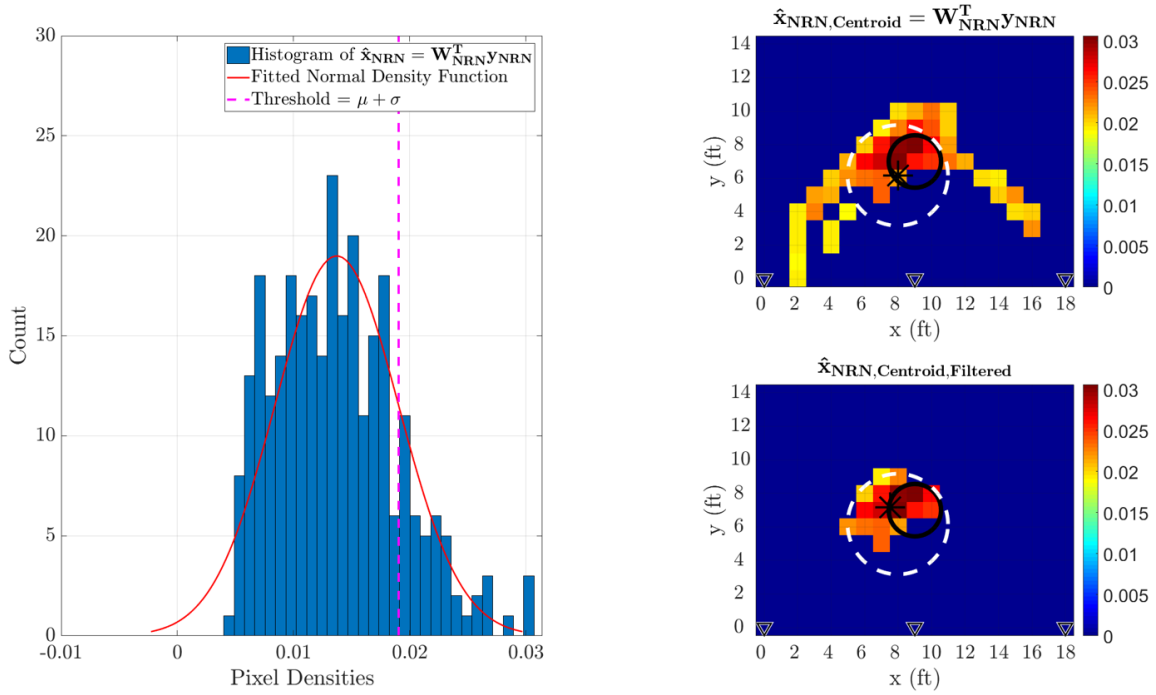

Figure 4.13. Left: Histogram of the pixel densities in $\hat{\mathbf{x}}_{\text{NRN}} = \mathbf{W}_{\text{NRN}}^{T}\mathbf{y}_{\text{NRN}}$ from Figure 4.12. Right: Top - The resultant image from thresholding $\hat{\mathbf{x}}_{\text{NRN}} = \mathbf{W}_{\text{NRN}}^{T}\mathbf{y}_{\text{NRN}}$ and the location of the centroid; Bottom - Filtering $\hat{\mathbf{x}}_{\text{NRN,Centroid}}$ by keeping the pixels inside the circumference of the dotted circle and reapplying the k-means algorithm.

Table 4.2. Performance metrics for the NRN trilateration solution with with targets at (9,7), (4,10) and (14,4).

Target Location	**Performance Metric**	**Description**	**Result**
(9,7)	MAP estimate	Coordinates of the most intense pixel.	(9,8) $\epsilon_{\text{MAP}} = 1$ ft
	K-means clustering	Coordinates of the centroid.	*Unfiltered* (7.98,6.17) $\epsilon_{\text{Centroid}} = 1.32$ ft
			Filtered (7.53,7.18) $\epsilon_{\text{Centroid,Filt}} = 1.48$ ft
	Dispersion	Pixel spread about the filtered centroid.	$\sigma_{\text{Centroid}} = 1.73$ ft
	Model solution	Compared to Figure 4.1.	$\Psi_{\text{Ideal}} = 0.47$
(4,10)	MAP estimate	Coordinates of the most intense pixel.	(7,11) $\epsilon_{\text{MAP}} = 3.16$ ft
	K-means clustering	Coordinates of the centroid.	*Unfiltered* (6.00,10.11) $\epsilon_{\text{Centroid}} = 2.00$ ft
			Filtered (5.86,10.27) $\epsilon_{\text{Centroid,Filt}} = 1.88$ ft
	Dispersion	Pixel spread about the filtered centroid.	$\sigma_{\text{Centroid}} = 1.85$ ft
	Model solution	Compared to Figure 4.1.	$\Psi_{\text{Ideal}} = 0.13$
(14,4)	MAP estimate	Coordinates of the most intense pixel.	(14,4) $\epsilon_{\text{MAP}} = 0$ ft
	K-means clustering	Coordinates of the centroid.	*Unfiltered* (13.85,3.79) $\epsilon_{\text{Centroid}} = 0.26$ ft
			Filtered (14.16,3.26) $\epsilon_{\text{Centroid,Filt}} = 0.75$ ft
	Dispersion	Pixel spread about the filtered centroid.	$\sigma_{\text{Centroid}} = 1.78$ ft
	Model solution	Compared to Figure 4.1.	$\Psi_{\text{Ideal}} = 0.13$

4.2.4 Tikhonov Regularized Solution.

4.2.4.1 Derivation.

Image reconstruction for a NRz Tikhonov regularized solution involves solving for $\mathbf{x}_{\text{NR}z}$ in (3.1). This will be achieved by taking the maximum likelihood (ML) derivation similar to Section 3.3, i.e.

$$\begin{aligned}\hat{\mathbf{x}}_{\text{NR}z,\text{ML}}(\mathbf{y}) &= \underset{\hat{\mathbf{x}}_{\text{NR}z}}{\arg\max}\ \ln \wp(\mathbf{y}_{\text{NR}z}|\mathbf{x}_{\text{NR}z}) \\ &= \underset{\hat{\mathbf{x}}_{\text{NR}z}}{\arg\max}\ \mathscr{L},\end{aligned} \tag{4.11}$$

where $\mathscr{L}$ is the log likelihood function. Assuming the noise vector $\mathbf{n}_{\text{NR}z} \sim \mathscr{N}(\mathbf{0}, \mathbf{C}_{\text{NR}z})$, therefore $\mathbf{y} \sim \mathscr{N}(\mathbf{W}_{\text{NR}z}\mathbf{x}_{\text{NR}z}, \mathbf{C}_{\text{NR}z})$. Hence,

$$\mathscr{L} = \ln\left[\left(\frac{1}{\sqrt{2\pi}^N |\mathbf{C}_{\text{NR}z}|}\right)\exp\left(-\frac{(\mathbf{y}_{\text{NR}z}-\mathbf{W}_{\text{NR}z}\mathbf{x}_{\text{NR}z})^T(\mathbf{C}_{\text{NR}z})^{-1}(\mathbf{y}_{\text{NR}z}-\mathbf{W}_{\text{NR}z}\mathbf{x}_{\text{NR}z})}{2}\right)\right] \tag{4.12}$$

$$\vdots$$

$$\begin{aligned}=& -\text{N}\ln\left(\sqrt{2\pi}\right) - \ln(|\mathbf{C}_{\text{NR}z}|) - \frac{1}{2}\big(\mathbf{y}_{\text{NR}z}^T\mathbf{C}_{\text{NR}z}^{-1}\mathbf{y}_{\text{NR}z} - \mathbf{x}_{\text{NR}z}^T\mathbf{W}_{\text{NR}z}^T\mathbf{C}_{\text{NR}z}^{-1}\mathbf{y}_{\text{NR}z} \cdots \\ & \qquad -\mathbf{x}_{\text{NR}z}^T\mathbf{W}_{\text{NR}z}^T\mathbf{C}_{\text{NR}z}^{-1}\mathbf{y}_{\text{NR}z} + \mathbf{x}_{\text{NR}z}^T\mathbf{W}_{\text{NR}z}^T\mathbf{C}_{\text{NR}z}^{-1}\mathbf{W}_{\text{NR}z}\mathbf{x}_{\text{NR}z}\big)\end{aligned}$$

$$= -\text{N}\ln\left(\sqrt{2\pi}\right) - \ln(|\mathbf{C}_{\text{NR}z}|) + f(\mathbf{x}_{\text{NR}z}). \tag{4.13}$$

Note that we want the arg max of $\mathscr{L}$ implying that we should solve for $f(\mathbf{x})$ in (4.13).

$$\arg\max_{\hat{\mathbf{x}}} \mathscr{L} = \nabla_{\mathbf{x}} \mathscr{L} \equiv \mathbf{0} \tag{4.14}$$

$$\begin{aligned}\mathbf{0}-\mathbf{0}-\frac{1}{2}\Big(\mathbf{0}-\mathbf{W}_{\mathrm{NR}z}^{T}\mathbf{C}_{\mathrm{NR}z}^{-1}\mathbf{y}_{\mathrm{NR}z}-\mathbf{W}_{\mathrm{NR}z}^{T}\mathbf{C}_{\mathrm{NR}z}^{-1}\mathbf{y}_{\mathrm{NR}z}+\cdots \\ \Big[\big(\mathbf{W}_{\mathrm{NR}z}^{T}\mathbf{C}_{\mathrm{NR}z}^{-1}\mathbf{W}_{\mathrm{NR}z}\big)+\big(\mathbf{W}_{\mathrm{NR}z}^{T}\mathbf{C}_{\mathrm{NR}z}^{-1}\mathbf{W}_{\mathrm{NR}z}\big)^{T}\Big]\hat{\mathbf{x}}_{\mathrm{NR}z}\Big)\equiv\mathbf{0}\end{aligned} \tag{4.15}$$

$$\vdots$$

$$\begin{aligned}\mathbf{W}_{\mathrm{NR}z}^{T}\mathbf{C}_{\mathrm{NR}z}^{-1}\mathbf{y}_{\mathrm{NR}z}-\mathbf{W}_{\mathrm{NR}z}^{T}\mathbf{C}_{\mathrm{NR}z}^{-1}\mathbf{W}_{\mathrm{NR}z}\hat{\mathbf{x}}_{\mathrm{NR}z}\equiv\mathbf{0} \\ \hat{\mathbf{x}}_{\mathrm{NR}z}=\big(\mathbf{W}_{\mathrm{NR}z}^{T}\mathbf{C}_{\mathrm{NR}z}^{-1}\mathbf{W}_{\mathrm{NR}z}\big)^{-1}\mathbf{W}_{\mathrm{NR}z}^{T}\mathbf{C}_{\mathrm{NR}z}^{-1}\mathbf{y}_{\mathrm{NR}z}.\end{aligned} \tag{4.16}$$

For (4.15), the vector calculus identities of (2.28) and (2.29) were used.

Since $\big(\mathbf{W}_{\mathrm{NR}z}^{T}\mathbf{C}_{\mathrm{NR}z}^{-1}\mathbf{W}_{\mathrm{NR}z}\big)$ in (3.12) is not invertible, we now apply Tikhonov regularization by injecting $\alpha_{\mathrm{NR}z}\|\mathbf{Q}\mathbf{x}_{\mathrm{NR}z}\|^2$ into $f(\mathbf{x}_{\mathrm{NR}z})$ in (4.13) to create certain desired properties that enforces a solution. $\alpha_{\mathrm{NR}z}$ is a tunable weight parameter where small values lead to solutions that fit the data and large values favor prior information.

$$\begin{aligned}f(\mathbf{x})=-\frac{1}{2}\big(\mathbf{y}_{\mathrm{NR}z}^{T}\mathbf{C}_{\mathrm{NR}z}^{-1}\mathbf{y}_{\mathrm{NR}z}-\mathbf{x}_{\mathrm{NR}z}^{T}\mathbf{W}_{\mathrm{NR}z}^{T}\mathbf{C}_{\mathrm{NR}z}^{-1}\mathbf{y}_{\mathrm{NR}z}-\mathbf{x}_{\mathrm{NR}z}^{T}\mathbf{W}_{\mathrm{NR}z}^{T}\mathbf{C}_{\mathrm{NR}z}^{-1}\mathbf{y}_{\mathrm{NR}z}+\cdots \\ \mathbf{x}_{\mathrm{FUS}}^{T}\mathbf{W}_{\mathrm{FUS}}^{T}\mathbf{C}_{\mathrm{FUS}}^{-1}\mathbf{W}_{\mathrm{FUS}}\mathbf{x}_{\mathrm{FUS}}+\alpha\|\mathbf{Q}\mathbf{x}_{\mathrm{FUS}}\|^{2}\big).\end{aligned} \tag{4.17}$$

Since the image will be two-dimensional (2D) for this thesis, Tikhonov regularization

calls for including derivatives in both the horizontal and vertical dimensions, i.e.

$$f(\mathbf{x}) = -\frac{1}{2}\Big(\mathbf{y}_{\mathrm{NR}z}^T\mathbf{C}_{\mathrm{NR}z}^{-1}\mathbf{y}_{\mathrm{NR}z} - \mathbf{x}_{\mathrm{NR}z}^T\mathbf{W}_{\mathrm{NR}z}^T\mathbf{C}_{\mathrm{NR}z}^{-1}\mathbf{y}_{\mathrm{NR}z} - \mathbf{x}_{\mathrm{NR}z}^T\mathbf{W}_{\mathrm{NR}z}^T\mathbf{C}_{\mathrm{NR}z}^{-1}\mathbf{y}_{\mathrm{NR}z} + \cdots$$
$$\mathbf{x}_{\mathrm{NR}z}^T\mathbf{W}_{\mathrm{NR}z}^T\mathbf{C}_{\mathrm{NR}z}^{-1}\mathbf{W}_{\mathrm{NR}z}\mathbf{x}_{\mathrm{NR}z} + \alpha_{\mathrm{NR}z}\left(\|\mathbf{D}_H\mathbf{x}_{\mathrm{NR}z}\|^2 + \|\mathbf{D}_V\mathbf{x}_{\mathrm{NR}z}\|^2\right)\Big) \tag{4.18}$$

$$\vdots$$

$$f(\mathbf{x}) = -\frac{1}{2}\Big(\mathbf{y}_{\mathrm{NR}z}^T\mathbf{C}_{\mathrm{NR}z}^{-1}\mathbf{y}_{\mathrm{NR}z} - \mathbf{x}_{\mathrm{NR}z}^T\mathbf{W}_{\mathrm{NR}z}^T\mathbf{C}_{\mathrm{NR}z}^{-1}\mathbf{y}_{\mathrm{NR}z} - \mathbf{x}_{\mathrm{NR}z}^T\mathbf{W}_{\mathrm{NR}z}^T\mathbf{C}_{\mathrm{NR}z}^{-1}\mathbf{y}_{\mathrm{NR}z} + \cdots$$
$$\mathbf{x}_{\mathrm{NR}z}^T\mathbf{W}_{\mathrm{NR}z}^T\mathbf{C}_{\mathrm{NR}z}^{-1}\mathbf{W}_{\mathrm{NR}z}\mathbf{x}_{\mathrm{NR}z} + \alpha_{\mathrm{NR}z}\left(\mathbf{x}_{\mathrm{NR}z}^T\mathbf{D}_H^T\mathbf{D}_H\mathbf{x}_{\mathrm{NR}z} + \mathbf{x}_{\mathrm{NR}z}^T\mathbf{D}_V^T\mathbf{D}_V\mathbf{x}_{\mathrm{NR}z}\right)\Big) \tag{4.19}$$

(4.14) now becomes:

$$\arg\max_{\hat{\mathbf{x}}}\ \mathscr{L} = \nabla_{\mathbf{x}}\mathscr{L} \equiv \mathbf{0} \tag{4.20}$$

$$-\frac{1}{2}\Bigg(\mathbf{0} - \mathbf{W}_{\mathrm{NR}z}^T\mathbf{C}_{\mathrm{NR}z}^{-1}\mathbf{y}_{\mathrm{NR}z} - \mathbf{W}_{\mathrm{NR}z}^T\mathbf{C}_{\mathrm{NR}z}^{-1}\mathbf{y}_{\mathrm{NR}z} + \Bigg[\left(\mathbf{W}_{\mathrm{NR}z}^T\mathbf{C}_{\mathrm{NR}z}^{-1}\mathbf{W}_{\mathrm{NR}z}\right) + \cdots$$
$$\vdots$$
$$\left(\mathbf{W}_{\mathrm{NR}z}^T\mathbf{C}_{\mathrm{NR}z}^{-1}\mathbf{W}_{\mathrm{NR}z}\right)^T\Bigg]\hat{\mathbf{x}}_{\mathrm{NR}z} + \alpha_{\mathrm{NR}z}\left[2\mathbf{D}_H^T\mathbf{D}_H\hat{\mathbf{x}}_{\mathrm{NR}z} + 2\mathbf{D}_V^T\mathbf{D}_V\hat{\mathbf{x}}_{\mathrm{NR}z}\right]\Bigg) \equiv \mathbf{0} \tag{4.21}$$

$$\mathbf{W}_{\mathrm{NR}z}^T\mathbf{C}_{\mathrm{NR}z}^{-1}\mathbf{y}_{\mathrm{NR}z} - \mathbf{W}_{\mathrm{NR}z}^T\mathbf{C}_{\mathrm{NR}z}^{-1}\mathbf{W}_{\mathrm{NR}z}\hat{\mathbf{x}}_{\mathrm{NR}z} + \alpha_{\mathrm{NR}z}\left[\mathbf{D}_H^T\mathbf{D}_H\hat{\mathbf{x}}_{\mathrm{NR}z} + 2\mathbf{D}_V^T\mathbf{D}_V\hat{\mathbf{x}}_{\mathrm{NR}z}\right] \equiv \mathbf{0} \tag{4.22}$$

$$\hat{\mathbf{x}}_{\mathrm{NR}z} = \left(\mathbf{W}_{\mathrm{NR}z}^T\mathbf{C}_{\mathrm{NR}z}^{-1}\mathbf{W}_{\mathrm{NR}z} + \alpha_{\mathrm{NR}z}\left[\mathbf{D}_H^T\mathbf{D}_H + \mathbf{D}_V^T\mathbf{D}_V\right]\right)^{-1}\mathbf{W}_{\mathrm{NR}z}^T\mathbf{C}_{\mathrm{NR}z}^{-1}\mathbf{y}_{\mathrm{NR}z} \tag{4.23}$$

$$\hat{\mathbf{x}}_{\mathrm{NR}z} = \underbrace{\left(\mathbf{W}_{\mathrm{NR}z}^T\mathbf{C}_{\mathrm{NR}z}^{-1}\mathbf{W}_{\mathrm{NR}z} + \alpha_{\mathrm{NR}z}\mathbf{Q}\right)^{-1}\mathbf{W}_{\mathrm{NR}z}^T\mathbf{C}_{\mathrm{NR}z}^{-1}}_{\mathbf{\Pi}_{\mathrm{NR}z}}\mathbf{y}_{\mathrm{NR}z} \tag{4.24}$$

For (4.21), the vector calculus identities of (2.28) and (2.29) were used which also handles the injected Tikhonov related matrices and vectors.

4.2.4.2 Assumed Covariance.

Figures 4.14, 4.15 and 4.16 display the results of a Tikhonov regularized solution assuming a covariance matrix $\mathbf{C}_{\mathrm{NR}z} = \sigma^2\mathbf{I}$. As a result, the covariance matrices drop out of the final solution through simplification. Figures 4.14, 4.15 and 4.16 also use the same impulse responses, $\mathbf{y}_{\mathrm{NR}z}$ and weighting matrices, $\mathbf{W}_{\mathrm{NR}z}$, used in the trilateration method in Subsection 4.2.3.

Figure 4.14 exhibits the result of the data capture made by NR1 with a Tikhonov regularization parameter, $\alpha = 200$. The strongest pixel shading density occurs around coordinate (3,3) away from the target at (9,7). There is however, some indication of target detection over (9,7) as well as (18,14). Figure 4.15 also exhibits the results of the data captures by NR2 (left) and NR3 (right) using a Tikhonov regularization parameter, $\alpha = 200$. Both results indicate detections over the true target coordinates, however there are also viable detections over false coordinates. Subjectively, Figures 4.14 and 4.15 do not provide clear indication of target location.

In stacking the impulse responses and weighting matrices appropriately to create $\mathbf{y}_{\mathrm{NRN}}$ and $\mathbf{W}_{\mathrm{NRN}}$ as done in (3.2), the Tikhonov regularized solution is presented in Figure 4.16, utilizing a Tikhonov regularization parameter, $\alpha = 200$. The most dense pixel shading does in fact occur around the target's location, however there are many more viable false target detections. There are similarities in comparing Figure 4.16, the Tikhonov regularized solution to the trilateration solution of Figure 4.12.

4.2.4.3 Empirical Covariance.

Here, instead of assuming an identity covariance matrix, $\mathbf{C}_{\mathrm{NR}z} = \sigma^2\mathbf{I}$ for simplicity, an empirical covariance matrix is created. Similar to Subsection 4.1.1, a covariance matrix, $\mathbf{C}_{\mathrm{NR}z}$ should be determined based on Equation 3.1. 600 triggers/collects were conducted at each location in Table 3.3. The 600 triggers/collects consists of 300 trig-

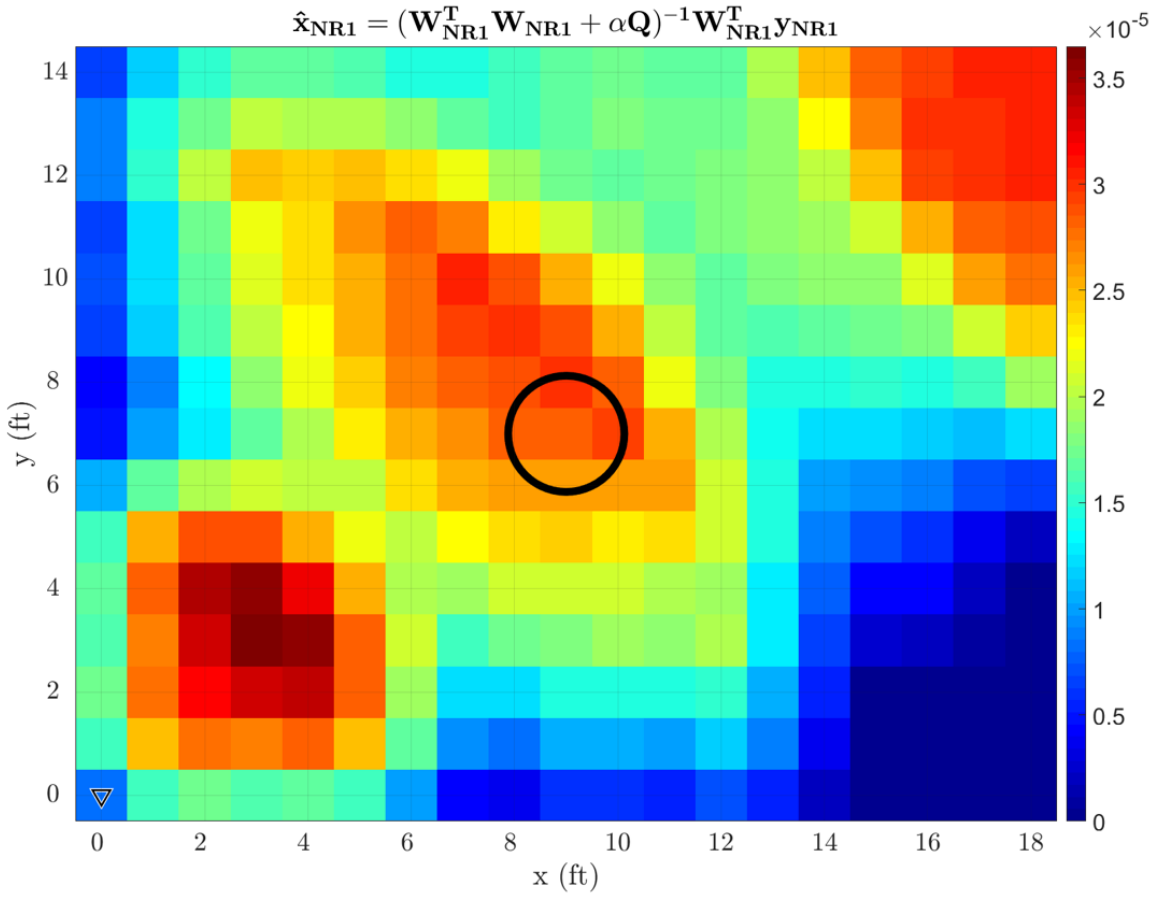

Figure 4.14. NR1 transmitting/receiving from coordinates (0,0), with target at coordinate (9,7). The regularization parameter α has subjectively been set to 200.

gers/collects of the background and 300 triggers/collects of an empty scene/no targets, with the idea that the noise, $\mathbf{n}_{\mathrm{NR}z}$, is the result of subtracting the two, i.e.

$$\mathbf{n}_{\mathrm{NR}z} = \begin{bmatrix} y_{1,\text{No Targets}} - y_{1,\text{Background}} \\ \vdots \\ y_{I,\text{No Targets}} - y_{I,\text{Background}} \end{bmatrix} = \begin{bmatrix} \mathrm{n}_{\mathrm{NR}z,1} \\ \vdots \\ \mathrm{n}_{\mathrm{NR}z,I} \end{bmatrix},$$

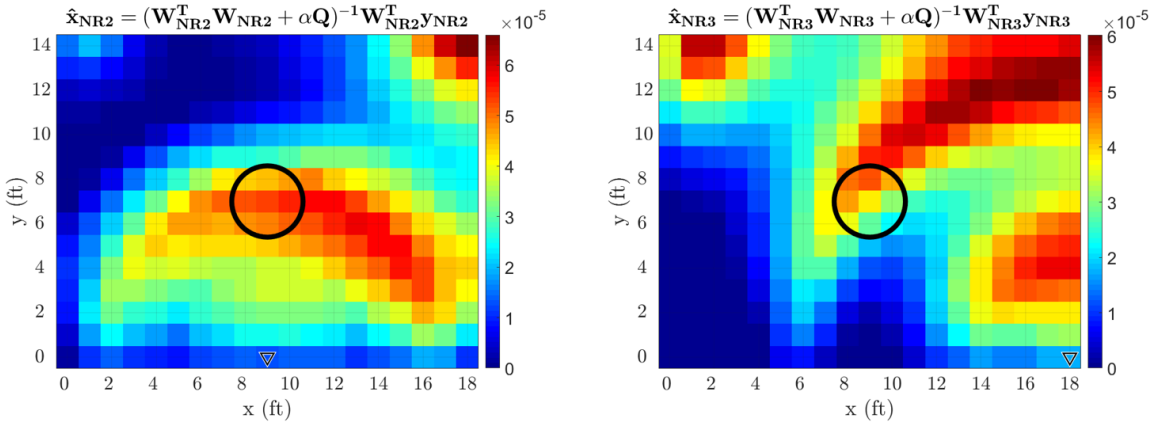

Figure 4.15. NR2 (left) and NR3 (right) transmitting/receiving from coordinates (9,0) and (18,0) respectively with target at coordinate (9,7). The regularization parameter α has subjectively been set to 200.

then the covariance matrix, $\mathbf{C}_{\mathrm{NR}z}$, is

$$
\begin{aligned}
[\mathbf{C}_{\mathrm{NR}z}]_{i,j} &= \mathbb{E}\big[\big(\mathrm{n}_{\mathrm{NR}z,i} - \mu_i\big)\big(\mathrm{n}_{\mathrm{NR}z,j} - \mu_j\big)\big] \\
&= \mathbb{E}\big[\mathrm{n}_{\mathrm{NR}z,i}\mathrm{n}_{\mathrm{NR}z,j} - \mathrm{n}_{\mathrm{NR}z,i}\mu_j - \mu_i\mathrm{n}_{\mathrm{NR}z,j} + \mu_i\mu_j\big] \\
&= \mathbb{E}\big[\mathrm{n}_{\mathrm{NR}z,i}\mathrm{n}_{\mathrm{NR}z,j}\big] - \mathbb{E}\big[\mathrm{n}_{\mathrm{NR}z,i}\mu_j\big] - \mathbb{E}\big[\mu_i\mathrm{n}_{\mathrm{NR}z,j}\big] + \mathbb{E}\big[\mu_i\mu_j\big] \\
&= \mathbb{E}\big[\mathrm{n}_{\mathrm{NR}z,i}\mathrm{n}_{\mathrm{NR}z,j}\big] - \mu_i\mu_j - \mu_i\mu_j + \mu_i\mu_j \\
&= \mathbb{E}\big[\mathrm{n}_{\mathrm{NR}z,i}\mathrm{n}_{\mathrm{NR}z,j}\big] - \mu_i\mu_j.
\end{aligned}
$$

Qualitatively, $\mathbf{C}_{\mathrm{NR}z}$ is a matrix whose element in the i,j position is the covariance of between the i-th and j-th element of the NRz noise vector, $\mathbf{n}_{\mathrm{NR}z}$.

Figure 4.17 displays two forms of the NRN covariance matrix $\mathbf{C}_{\mathrm{NRN}}$. Construction of $\mathbf{C}_{\mathrm{NRN}}$ is achieved by creating a pseudo 3×3 Block identity matrix whose diagonal consists of $\mathbf{C}_{\mathrm{NR1}}$, $\mathbf{C}_{\mathrm{NR2}}$ and $\mathbf{C}_{\mathrm{NR3}}$ as per Equation 3.1, implying the impulse responses collected from each AFIT NoNET node in Table 3.3 are independent. The version on the left of Figure 4.17 is the raw empirical NRN covariance matrix which was found to be non-invertible. Since invertibility of the covariance matrices for Tikhonov regularized solutions is mandatory, an approximation was needed to make $\mathbf{C}_{\mathrm{NRN}}$ invertible.

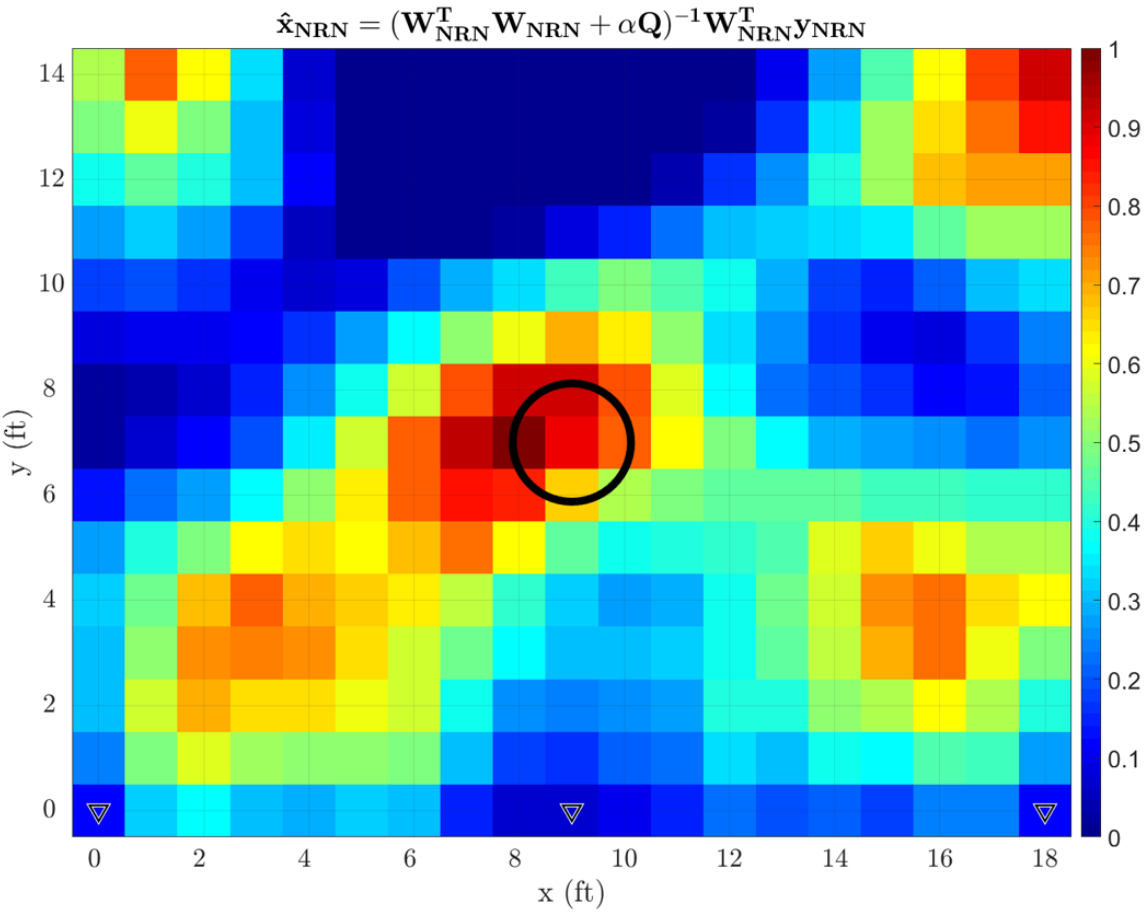

Figure 4.16. NRN transmitting/receiving from coordinates (0,0), (9,0) and (18,0) with target at coordinate (9,7). The regularization parameter α has subjectively been set to 200.

To approximate the raw empirical version of $\mathbf{C}_{\text{NRN}}$, each $\mathbf{C}_{\text{NR}z}$ matrix was made into a diagonal-constant matrix, i.e. a Toeplitz matrix. A Toeplitz matrix means all elements along a diagonal have the same value, thus, each diagonal of the "approximated" $\mathbf{C}_{\text{NR}z}$ matrix is an average of the each corresponding diagonal of the "raw" $\mathbf{C}_{\text{NR}z}$ matrix. Approximating for a Toeplitz matrix implies that the variables in the impulse responses are all correlated and wide-sense stationary (WSS). The final result is shown on the right of Figure 4.17.

The effects of introducing the empirical covariance matrix into the AFIT NoNET Tikhonov regularized solution is quite evident as displayed in Figure 4.18. Figure 4.18

presents a comparison between the result of assuming an identity covariance matrix (left) versus implementing the empirical NRN covariance matrix (right). The empirical covariance solution still has its most dense pixel shading over the target's coordinates along with reducing the uncertainty of target detections occurring in other areas within the target scene compared to that of the identity covariance solution.

4.2.4.4 Performance Metrics.

Figure 4.19 displays a 30 bin histogram of the AFIT NoNET Tikhonov regularized solution using an assumed covariance matrix as shown in Figure 4.16 as well as the location of the centroid. A normal distribution is able to be fit around the data. The performance metrics for the NRN Tikhonov regularized solution of Figure 4.16 are organized in Table 4.3.

Figure 4.20 displays a 30 bin histogram of the AFIT NoNET Tikhonov regularized solution using an empirical covariance matrix as shown in Figure 4.18 as well as the location of the centroid. Figures A.4 and B.4 display the results of the human target at (4,10) and (14,4) respectively. The performance metrics for all the NRN Tikhonov regularized solutions are organized in Table 4.4.

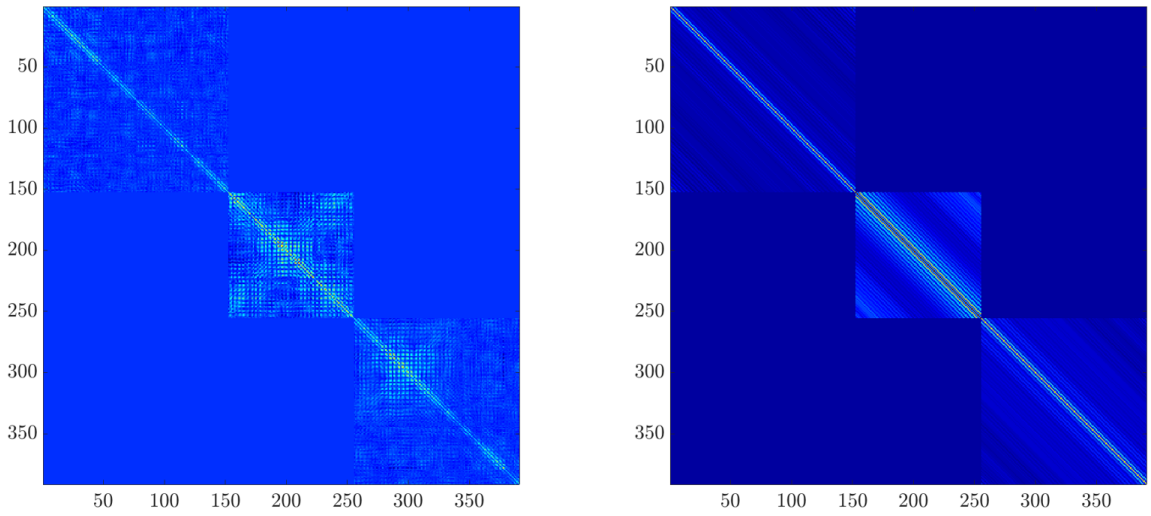

Figure 4.17. Left: The raw empirical NRN covariance matrix. Right: The approximated empirical NRN covariance matrix.

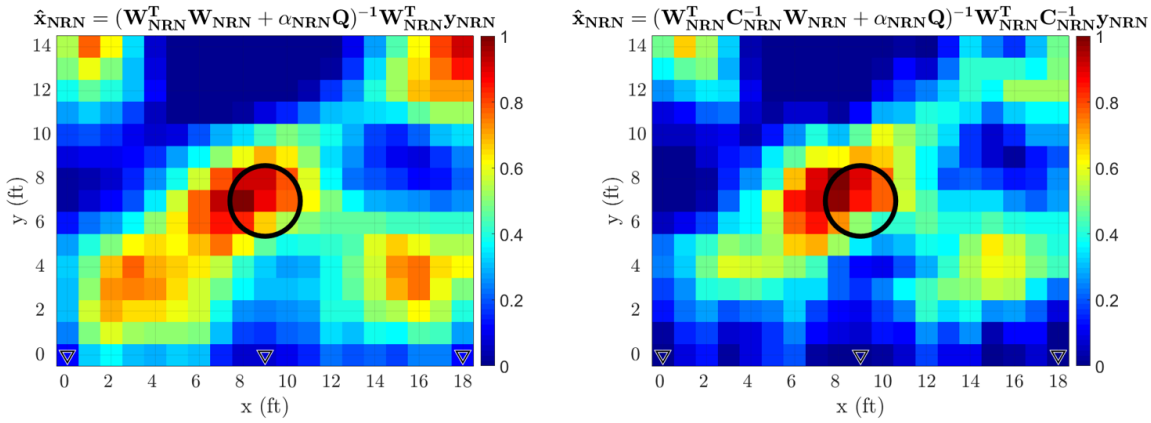

Figure 4.18. NRN transmitting/receiving from coordinates (0,0), (9,0) and (18,0) with target at coordinate (9,7). The regularization parameter α has subjectively been set to 200. Left: Utilizing the assumed covariance of the form $\mathbf{C} = \sigma^2\mathbf{I}$. Right: Utilizing the approximated empirical covariance.

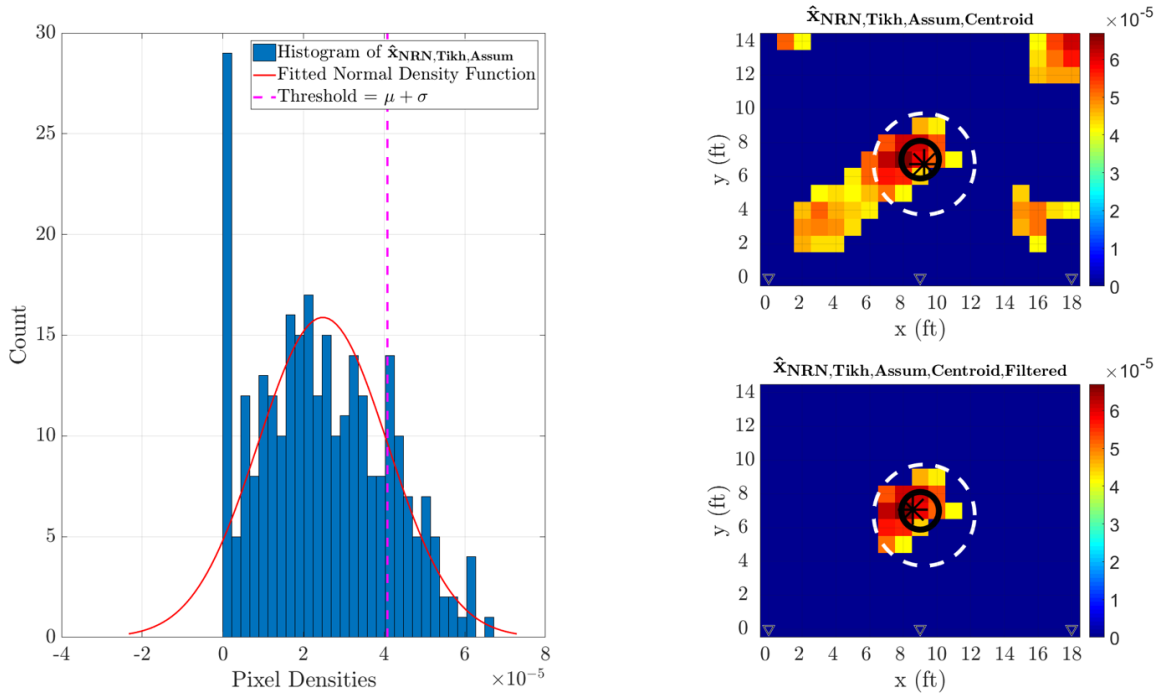

Figure 4.19. Left: Histogram of the pixel densities in $\hat{\mathbf{x}}_{\text{NRN,Tikh,Assump}}$ from Figure 4.16. Right: Top - The resultant image from thresholding $\hat{\mathbf{x}}_{\text{NRN,Tikh,Assump}}$ and the location of the centroid; Bottom - Filtering $\hat{\mathbf{x}}_{\text{NRN,Tikh,Assum,Centroid}}$ by keeping the pixels inside the circumference of the dotted circle and reapplying the k-means algorithm.

Table 4.3. Performance metrics for the NRN Tikhonov regularized solution. (Assumed covariance)

Performance Metric	**Description**	**Result**
MAP estimate	Coordinates of the most intense pixel.	(8,7) $\epsilon_{\text{MAP}} = 1$ ft
K-means clustering	Coordinates of the centroid.	*Unfiltered* (9.24,6.74) $\epsilon_{\text{Centroid}} = 0.35$ ft
		Filtered (8.56,7.06) $\epsilon_{\text{Centroid,Filt}} = 0.44$ ft
Dispersion	Pixel spread about the filtered centroid.	$\sigma_{\text{Centroid}} = 1.65$ ft
Model solution	Compared to Figure 4.1.	$\epsilon_{\text{Ideal}} = 0.43$

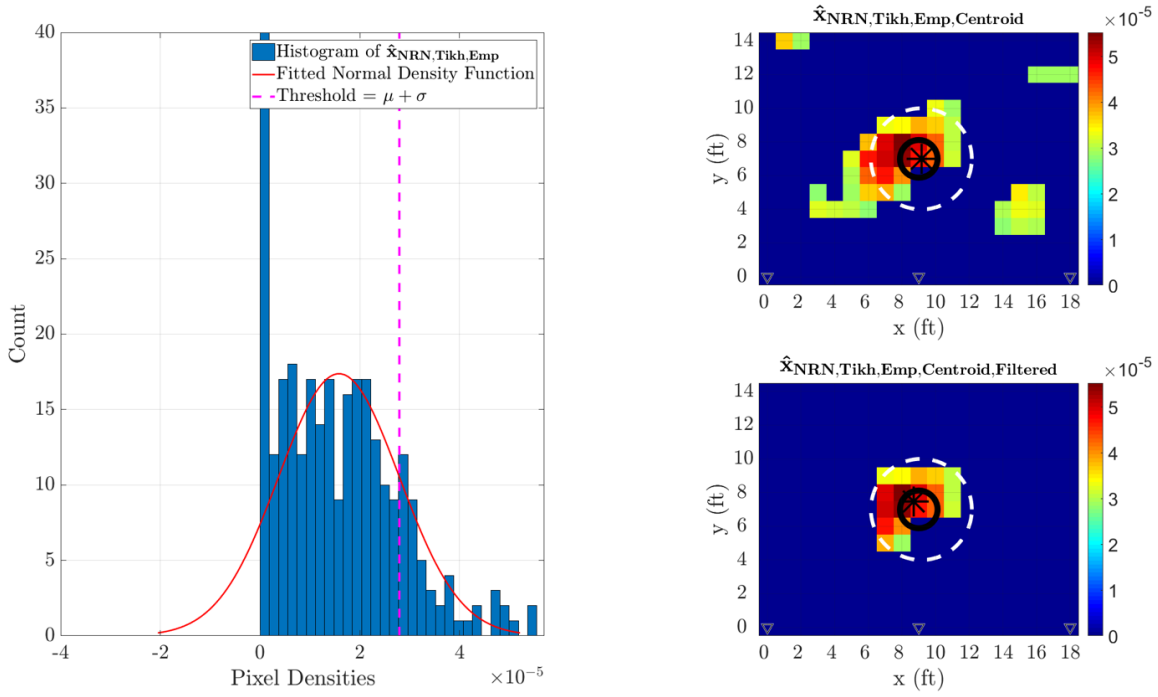

Figure 4.20. Left: Histogram of the pixel densities in $\hat{\mathbf{x}}_{\text{NRN,Tikh,Emp}}$ from the image on the right in Figure 4.18. Right: Top - The resultant image from thresholding $\hat{\mathbf{x}}_{\text{NRN,Tikh,Emp}}$ and the location of the centroid; Bottom - Filtering $\hat{\mathbf{x}}_{\text{NRN,Tikh,Emp,Centroid}}$ by keeping the pixels inside the circumference of the dotted circle and reapplying the k-means algorithm.

Table 4.4. Performance metrics for the NRN Tikhonov regularized solution with with targets at (9,7), (4,10) and (14,4).

Target Location	**Performance Metric**	**Description**	**Result**
(9,7)	MAP estimate	Coordinates of the most intense pixel.	(8,7) $\epsilon_{\text{MAP}} = 1$ ft
	K-means clustering	Coordinates of the centroid.	*Unfiltered* (9.15,7.00) $\epsilon_{\text{Centroid}} = 0.15$ ft
			Filtered (8.68,7.47) $\epsilon_{\text{Centroid,Filt}} = 0.57$ ft
	Dispersion	Pixel spread about the filtered centroid.	$\sigma_{\text{Centroid}} = 1.81$ ft
	Model solution	Compared to Figure 4.1.	$\Psi_{\text{Ideal}} = 0.35$
(4,10)	MAP estimate	Coordinates of the most intense pixel.	(6,10) $\epsilon_{\text{MAP}} = 2$ ft
	K-means clustering	Coordinates of the centroid.	*Unfiltered* (6.70,10.27) $\epsilon_{\text{Centroid}} = 2.72$ ft
			Filtered (6.40,10.12) $\epsilon_{\text{Centroid,Filt}} = 2.40$ ft
	Dispersion	Pixel spread about the filtered centroid.	$\sigma_{\text{Centroid}} = 1.93$ ft
	Model solution	Compared to Figure 4.1.	$\Psi_{\text{Ideal}} = 0.30$
(14,4)	MAP estimate	Coordinates of the most intense pixel.	(13,2) $\epsilon_{\text{MAP}} = 2.24$ ft
	K-means clustering	Coordinates of the centroid.	*Unfiltered* (13.29,4.62) $\epsilon_{\text{Centroid}} = 0.94$ ft
			Filtered (14.5,5.32) $\epsilon_{\text{Centroid,Filt}} = 0.59$ ft
	Dispersion	Pixel spread about the filtered centroid.	$\sigma_{\text{Centroid}} = 2.00$ ft
	Model solution	Compared to Figure 4.1.	$\Psi_{\text{Ideal}} = 0.24$

4.3 Multi-Sensor Data Fusion

4.3.1 Approach I: Fusing Separate Images.

Approach I of MSDF for this thesis involves creating separate images from the two disparate sensor technologies, RTI and the AFIT NoNET, and combining them in two ways

1. Averaging.

2. Kalman filtering.

4.3.1.1 Averaging.

Figure 4.21 displays the result of taking the average of the numerical pixel densities between Figure 4.4 and the right of Figure 4.18. Prior to taking the average, the images are normalized by dividing the all numerical pixel densities in each image by the maximum numerical pixel density in that image.

4.3.1.2 Kalman Filtering.

Following the Kalman filter dynamic system model format of (2.36), the model used for the MSDF Kalman filter solution is

$$\begin{aligned} \hat{\mathbf{x}}_{\mathrm{KAL},k} &= \mathbf{F}_k \hat{\mathbf{x}}_{\mathrm{KAL},k-1} + \mathbf{w}_k \\ \hat{\mathbf{x}}_{\mathrm{KAL},k} &= \hat{\mathbf{x}}_{\mathrm{KAL},k-1} + \mathbf{w}_k, \quad \mathbf{w}_k \sim \mathcal{N}(\mathbf{0}, \mathbf{Q}), \end{aligned} \tag{4.25}$$

where $\hat{\mathbf{x}}_{\mathrm{KAL}}$ is the Kalman filter solution using the image pixel densities from the RTI attenuation and NRN reflection/backscatter images generated using the ML estimate with Tikhonov regularization. Qualitatively, (4.25) represents the estimated state of the target scene with inherent process noise, $\mathbf{w}_k$. Note that we have no knowledge of the

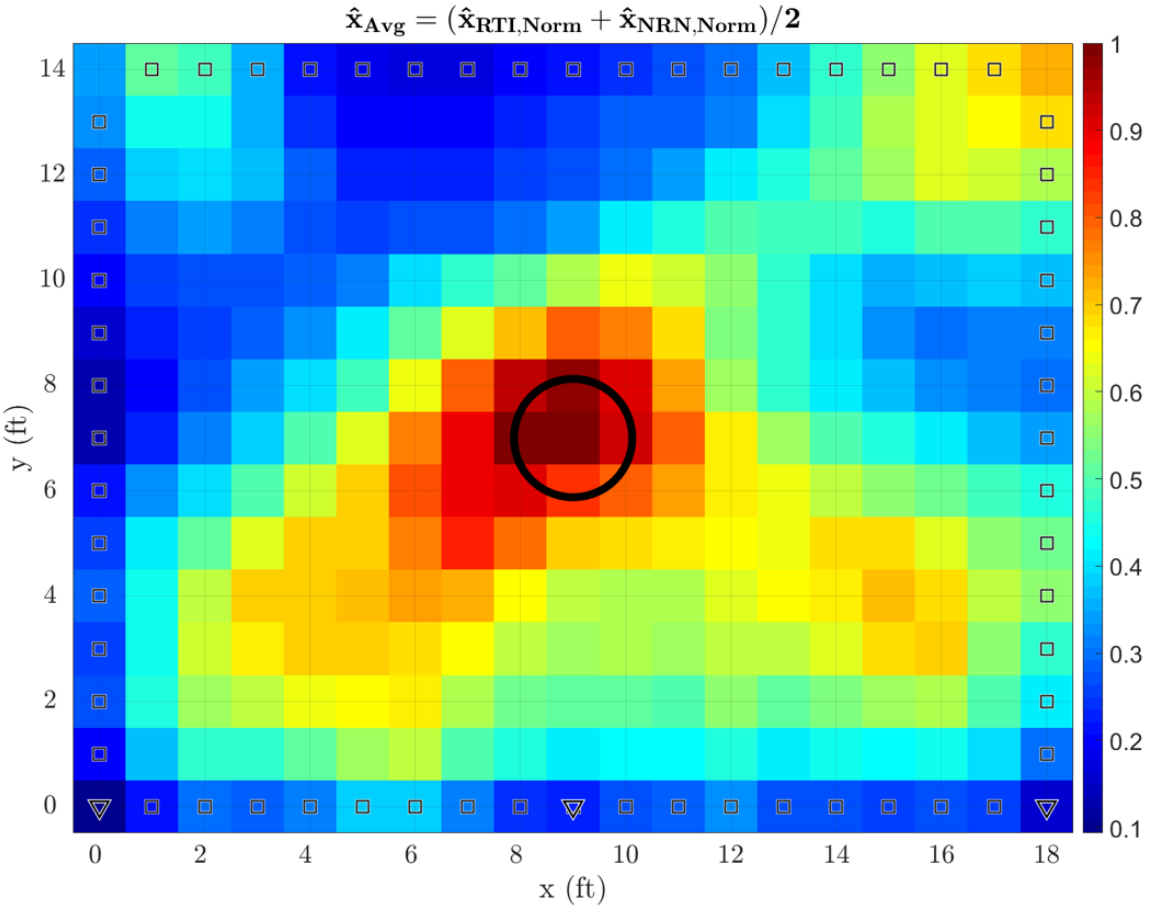

Figure 4.21. Taking the average of the Tikhonov solutions from the RTI and the AFIT NoNET sensors, i.e. Figure 4.4 and the right of Figure 4.18.

state transition model, $\mathbf{F}_k$, and are solely relying on the image pixels. For this reason, $\mathbf{F}_k$, has disappeared from (4.25). The current and prior time steps, k and $k-1$, represent only one time step, i.e., $\hat{\mathbf{x}}_{\mathrm{KAL},k}$ and $\hat{\mathbf{x}}_{\mathrm{KAL},k-1}$ are not time averaged.

Following the observation equation format of (2.37), the observation model for the

application in this Kalman filter solution will take the form of

$$\mathbf{z}_k = \mathbf{H}\mathbf{x}_k + \mathbf{v}_k$$

$$\begin{bmatrix} \hat{\mathbf{x}}_{\text{RTI}} \\ \hat{\mathbf{x}}_{\text{NRN}} \end{bmatrix}_k = \begin{bmatrix} 1 & 0 \\ 0 & 1 \end{bmatrix} \mathbf{x}_k + \mathbf{v}_k, \tag{4.26}$$

$$\mathbf{v}_k \sim \mathcal{N}(\mathbf{0}, \mathbf{R}) \tag{4.27}$$

Qualitatively, (4.26) is an observation of the pixel intensities of the RTI and NRN Tikhonov regularized images $\hat{\mathbf{x}}_{\text{RTI}}$ and $\hat{\mathbf{x}}_{\text{NRN}}$, with inherent and individualized pixel noise, $\mathbf{v}_k$. The observation model, $\mathbf{H}$, is represented by an identity matrix, which means that the contribution of the pixels from the RTI and NRN Tikhonov regularized images are only subject to their respective noise in $\mathbf{v}_k$.

Figure 4.22 displays the result of using the Kalman filter with the method of state-vector fusion as per Subsubsection 2.3.1.4. Note that Figure 4.22 is a result of just one pass through the Kalman filter.

4.3.1.3 Performance Metrics.

Figure 4.23 displays a 30 bin histogram of the MSDF averaging solution as shown in Figure 4.21 as well as the location of the centroid. Figures A.5 and B.5 display the MSDF averaging results of the human target at (4,10) and (14,4) respectively. Figure 4.24 displays a 30 bin histogram of the MSDF Kalman filter solution as shown in Figure 4.22 as well as the location of the centroid. Figures A.6 and B.6 display the MSDF Kalman filter results of the human target at (4,10) and (14,4) respectively. The performance metrics for all the MSDF averaging solutions and all the MSDF Kalman filter solutions are organized in Tables 4.5 and 4.6 respectively.

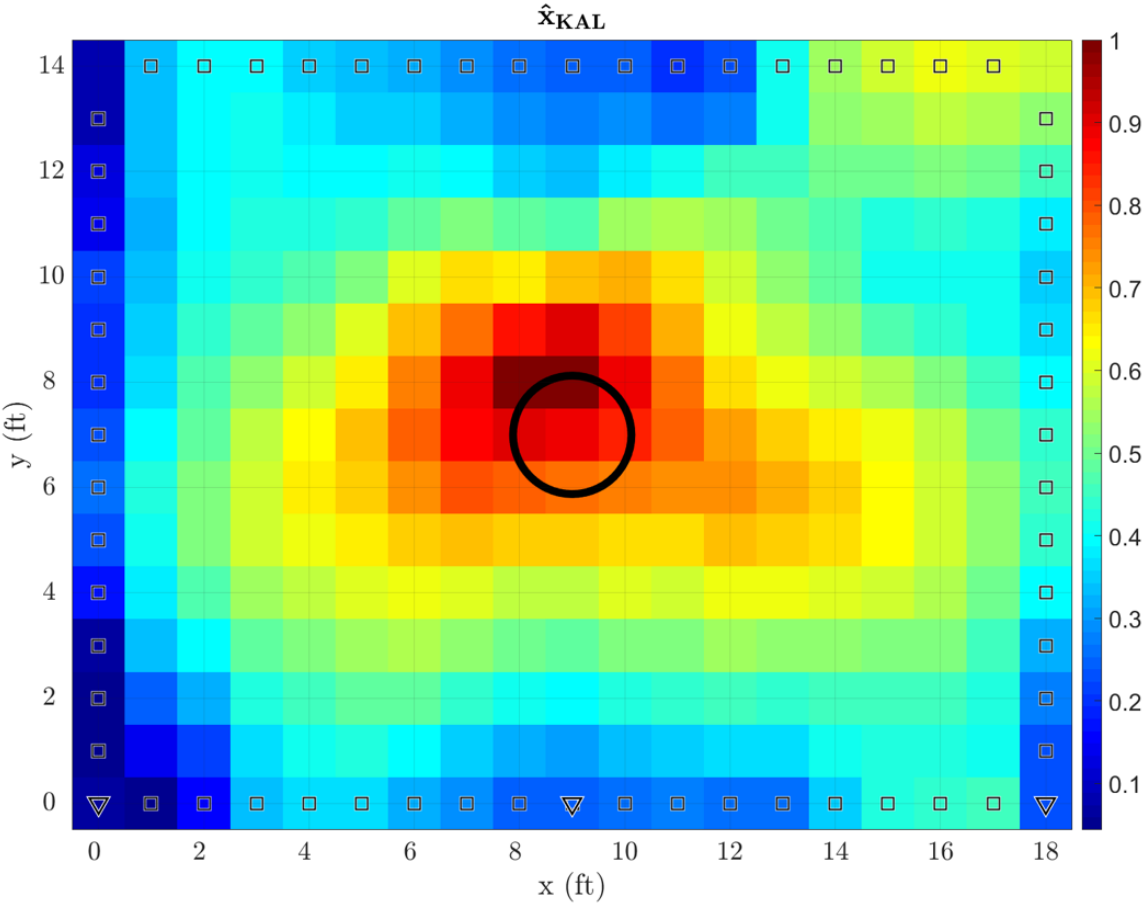

Figure 4.22. Taking the pixel densities of the Tikhonov solutions from the RTI and the AFIT NoNET sensors, i.e. Figure 4.4 and the right of Figure 4.18 and applying a Kalman filter to them using state-vector fusion.

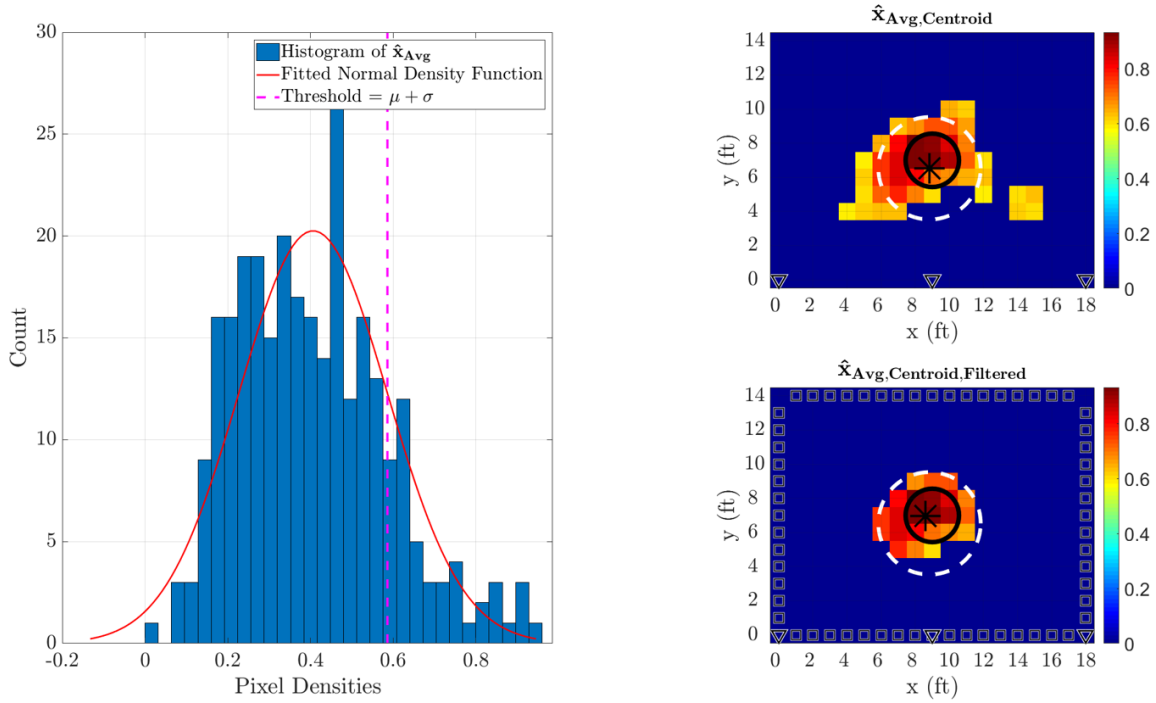

Figure 4.23. Left: Histogram of the pixel densities in $\hat{\mathbf{x}}_{\text{Avg}}$ from Figure 4.21. Right: Top - The resultant image from thresholding $\hat{\mathbf{x}}_{\text{Avg}}$ and the location of the centroid; Bottom - Filtering $\hat{\mathbf{x}}_{\text{Avg,Centroid}}$ by keeping the pixels inside the circumference of the dotted circle and reapplying the k-means algorithm.

Table 4.5. Performance metrics for the MSDF averaged solution with targets at (9,7), (4,10) and (14,4).

Target Location	**Performance Metric**	**Description**	**Result**
(9,7)	MAP estimate	Coordinates of the most intense pixel.	(9,7) $\epsilon_{\text{MAP}} = 0$ ft
	K-means clustering	Coordinates of the centroid.	*Unfiltered* (8.84,6.53) $\epsilon_{\text{Centroid}} = 0.49$ ft
			Filtered (8.61,6.96) $\epsilon_{\text{Centroid,Filt}} = 0.39$ ft
	Dispersion	Pixel spread about the filtered centroid.	$\sigma_{\text{Centroid}} = 1.90$ ft
	Model solution	Compared to Figure 4.1.	$\Psi_{\text{Ideal}} = 0.45$
(4,10)	MAP estimate	Coordinates of the most intense pixel.	(6,10) $\epsilon_{\text{MAP}} = 2$ ft
	K-means clustering	Coordinates of the centroid.	*Unfiltered* (5.33,10.05) $\epsilon_{\text{Centroid}} = 1.33$ ft
			Filtered (5.48,10.11) $\epsilon_{\text{Centroid,Filt}} = 1.49$ ft
	Dispersion	Pixel spread about the filtered centroid.	$\sigma_{\text{Centroid}} = 2.00$ ft
	Model solution	Compared to Figure 4.1.	$\Psi_{\text{Ideal}} = 0.42$
(14,4)	MAP estimate	Coordinates of the most intense pixel.	(14,5) $\epsilon_{\text{MAP}} = 1$ ft
	K-means clustering	Coordinates of the centroid.	*Unfiltered* (13.15,4.28) $\epsilon_{\text{Centroid}} = 0.89$ ft
			Filtered (13.28,4.41) $\epsilon_{\text{Centroid,Filt}} = 0.83$ ft
	Dispersion	Pixel spread about the filtered centroid.	$\sigma_{\text{Centroid}} = 2.09$ ft
	Model solution	Compared to Figure 4.1.	$\Psi_{\text{Ideal}} = 0.35$

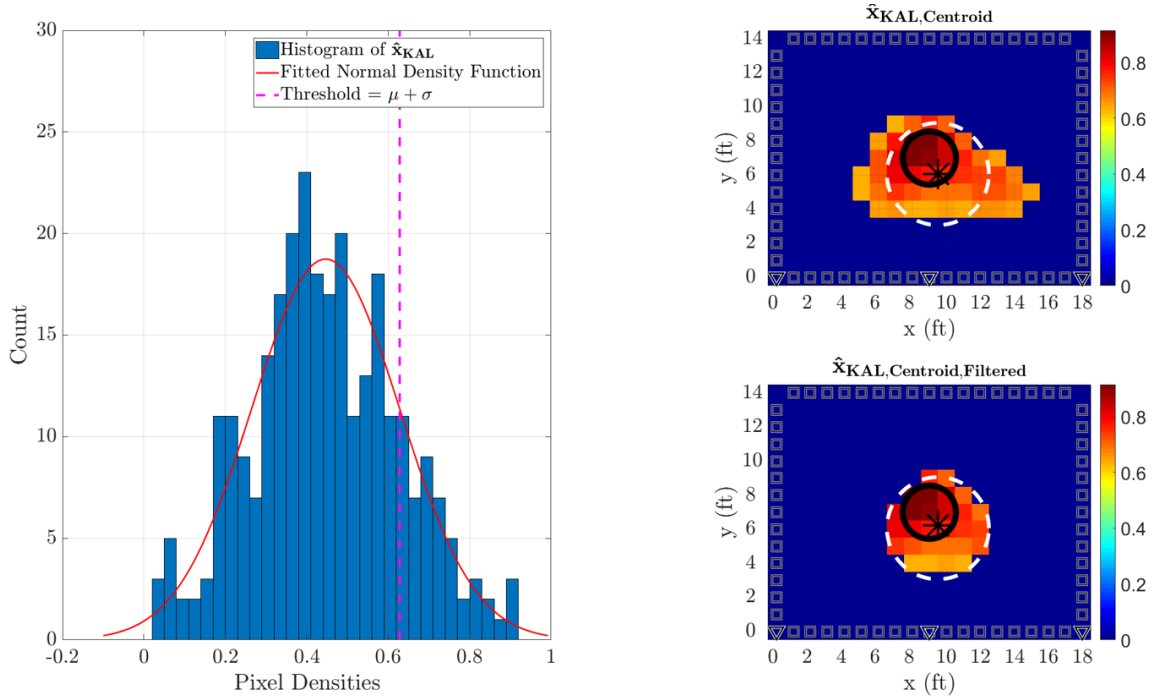

Figure 4.24. Left: Histogram of the pixel densities in $\hat{\mathbf{x}}_{\text{KAL}}$ from the image on the right in Figure 4.22. Right: Top - The resultant image from thresholding $\hat{\mathbf{x}}_{\text{KAL}}$ and the location of the centroid; Bottom - Filtering $\hat{\mathbf{x}}_{\text{KAL,Centroid}}$ by keeping the pixels inside the circumference of the dotted circle and reapplying the k-means algorithm.

Table 4.6. Performance metrics for the MSDF Kalman filter solution with targets at (9,7), (4,10) and (14,4).

Target Location	Performance Metric	Description	Result
(9,7)	MAP estimate	Coordinates of the most intense pixel.	(9,7) $\epsilon_{\text{MAP}} = 0$ ft
	K-means clustering	Coordinates of the centroid.	*Unfiltered* (9.50,6.06) $\epsilon_{\text{Centroid}} = 1.06$ ft
			Filtered (9.50,6.21) $\epsilon_{\text{Centroid,Filt}} = 0.93$ ft
	Dispersion	Pixel spread about the filtered centroid.	$\sigma_{\text{Centroid}} = 2.08$ ft
	Model solution	Compared to Figure 4.1.	$\Psi_{\text{Ideal}} = 0.50$
(4,10)	MAP estimate	Coordinates of the most intense pixel.	(4,11) $\epsilon_{\text{MAP}} = 1$ ft
	K-means clustering	Coordinates of the centroid.	*Unfiltered* (4.44,10.85) $\epsilon_{\text{Centroid}} = 0.96$ ft
			Filtered (5.48,10.11) $\epsilon_{\text{Centroid,Filt}} = 1.49$ ft
	Dispersion	Pixel spread about the filtered centroid.	$\sigma_{\text{Centroid}} = 2.05$ ft
	Model solution	Compared to Figure 4.1.	$\Psi_{\text{Ideal}} = 0.47$
(14,4)	MAP estimate	Coordinates of the most intense pixel.	(14,5) $\epsilon_{\text{MAP}} = 1$ ft
	K-means clustering	Coordinates of the centroid.	*Unfiltered* (13.76,5.40) $\epsilon_{\text{Centroid}} = 1.39$ ft
			Filtered (13.72,5.41) $\epsilon_{\text{Centroid,Filt}} = 1.44$ ft
	Dispersion	Pixel spread about the filtered centroid.	$\sigma_{\text{Centroid}} = 2.07$ ft
	Model solution	Compared to Figure 4.1.	$\Psi_{\text{Ideal}} = 0.44$

4.3.2 Approach II: Fusing Disparate Data.

Approach II mathematically involves "stacking" the vectors and matrices ($\mathbf{y}_{\text{RTI}}$, $\mathbf{y}_{\text{NRN}}$, $\mathbf{W}_{\text{RTI}}$ and $\mathbf{W}_{\text{NRN}}$) responsible for creating the images viewed in Sections 4.1 and 4.2, the MSDF vector, $\mathbf{y}_{\text{FUS}}$ and MSDF weighting matrix, $\mathbf{W}_{\text{FUS}}$, are created as per the system model definition defined by (3.5). Solving for the image, $\hat{\mathbf{x}}_{\text{FUS}}$, in accordance with the steps detailed in Section 3.3 whilst employing the empirical covariance matrices, $\mathbf{C}_{\text{RTI}}$ and $\mathbf{C}_{\text{NRN}}$ to create $\mathbf{C}_{\text{FUS}}$, a MSDF image is exhibited in Figure 4.25.

A Tikhonov regularization parameter of $\alpha = 400$ was subjectively chosen based on aesthetic. Again, the black and white squares and triangles surrounding the edge of the MSDF image represent the RTI and AFIT NoNET nodes. From Figure 4.25, the most dense pixel shading occurs just below the target's coordinates. It is visually apparent, that the ambiguity of the target's location in the MSDF image is greater than that of the RTI (Figure 4.4) and the AFIT NoNET (right of Figure 4.18) Tikhonov regularized solution.

4.3.2.1 Introducing Beta.

In order to increase the "influence" of either sensor in the creation of the MSDF image, a proposal for a second tunable parameter β, to be injected into the system model definition in (3.5), is considered. The β parameter also accounts for the disparate units used by RTI (i.e. shadowing) and the AFIT NoNET (i.e. reflectivity/backscattering). This β parameter will be applied to the RTI sensor technology and will henceforth be labeled as β_{RTI}. Mathematically, the system model definition will now effectively become

$$\begin{bmatrix} \mathbf{y}_{\text{RTI}} \\ \mathbf{y}_{\text{NRN}} \end{bmatrix} = \begin{bmatrix} \beta_{\text{RTI}}\mathbf{W}_{\text{RTI}} \\ \mathbf{W}_{\text{NRN}} \end{bmatrix} \mathbf{x}_{\text{FUS}} + \begin{bmatrix} \mathbf{n}_{\text{RTI}} \\ \mathbf{n}_{\text{NRN}} \end{bmatrix}, \quad \beta_{\text{RTI}} > 0. \tag{4.28}$$

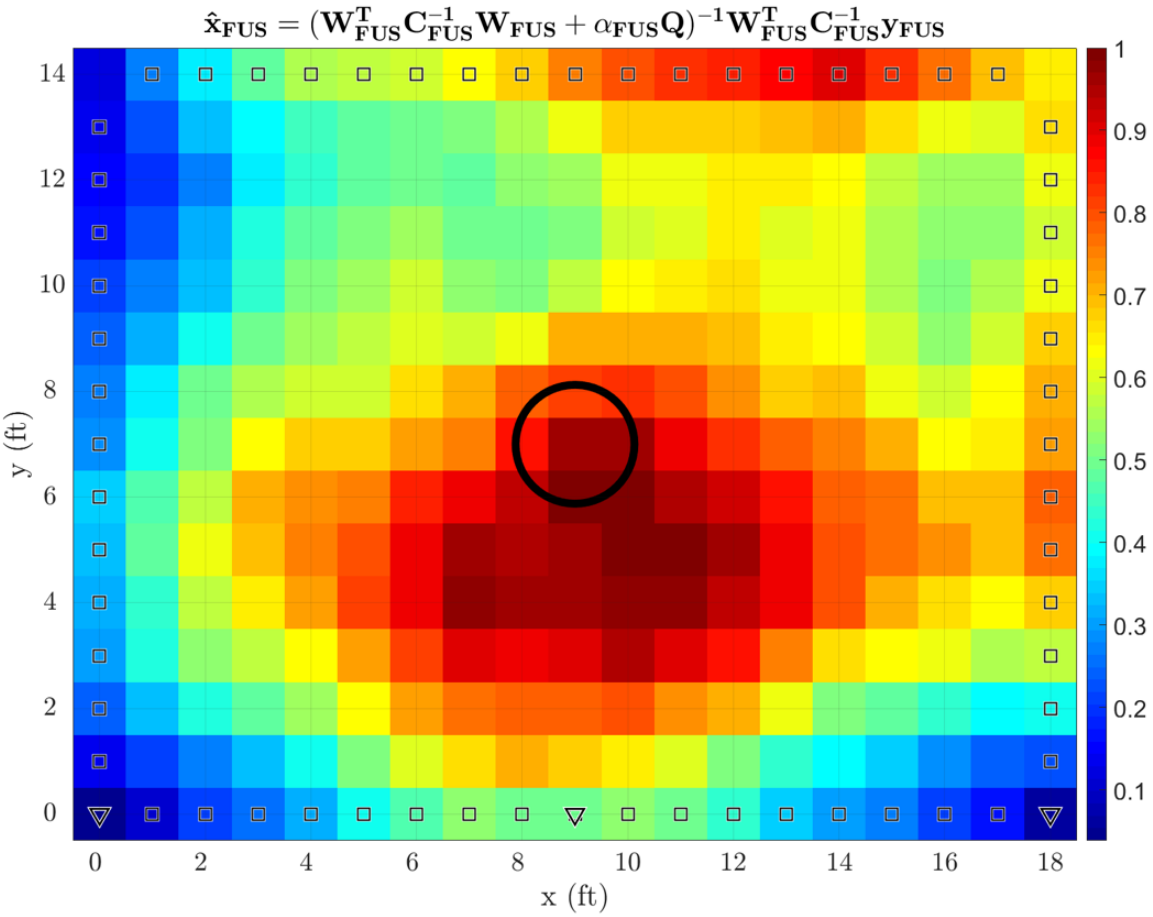

Figure 4.25. A MSDF image with a target at coordinate (9,7). The Tikhonov regularization parameter, $\alpha = 400$, was subjectively chosen based on aesthetic.

Selection of a numerical value for β_{RTI} was influenced by the performance metrics used in this research. A sweep from $\beta_{\text{RTI}} = 0.01$ to $\beta_{\text{RTI}} = 1000$ was conducted across the three target location scenarios with the resulting performance metrics combined as shown in Figure 4.26. The β_{RTI} value at which the minimum value occurs in the bottom graph of Figure 4.26 was found to be $\beta_{\text{RTI}} = 26.31$. Note that Ψ_{Ideal} was omitted from the creation of the bottom graph of Figure 4.26. This is due to a difference in units, however, ommitance of Ψ_{Ideal} does not have much effect, as Ψ_{Ideal} remains relatively constant as observed from the top graph of Figure 4.26.

Figure 4.27 displays the result of introducing the $\beta_{\text{RTI}} = 26.31$ parameter, comparing

it to the result obtained when no β_{RTI} parameter is involved, i.e. $\beta_{\text{RTI}} = 1$. The outcome of increasing the influence of the RTI sensor on the MSDF image, results in a “cleaner" image allowing for better target location and detection.

4.3.2.2 Performance Metrics.

Figure 4.28 displays a 30 bin histogram of the MSDF Tikhonov regularized solution as shown in Figure 4.25 as well as the location of the centroid. Figures A.7 and B.7 display the MSDF Tikhonov regularized results of the human target at (4,10) and (14,4) respectively. Figure 4.29 displays a 30 bin histogram of the MSDF Tikhonov regularized β solution as shown in right of Figure 4.27 as well as the location of the centroid. Figures A.8 and B.8 display the MSDF Tikhonov regularized β results of the human target at (4,10) and (14,4) respectively.

The performance metrics for all the MSDF Tikhonov regularized solutions are organized in Table 4.7. The performance metrics for all the MSDF Tikhonov regularized solutions are organized in Table 4.8.

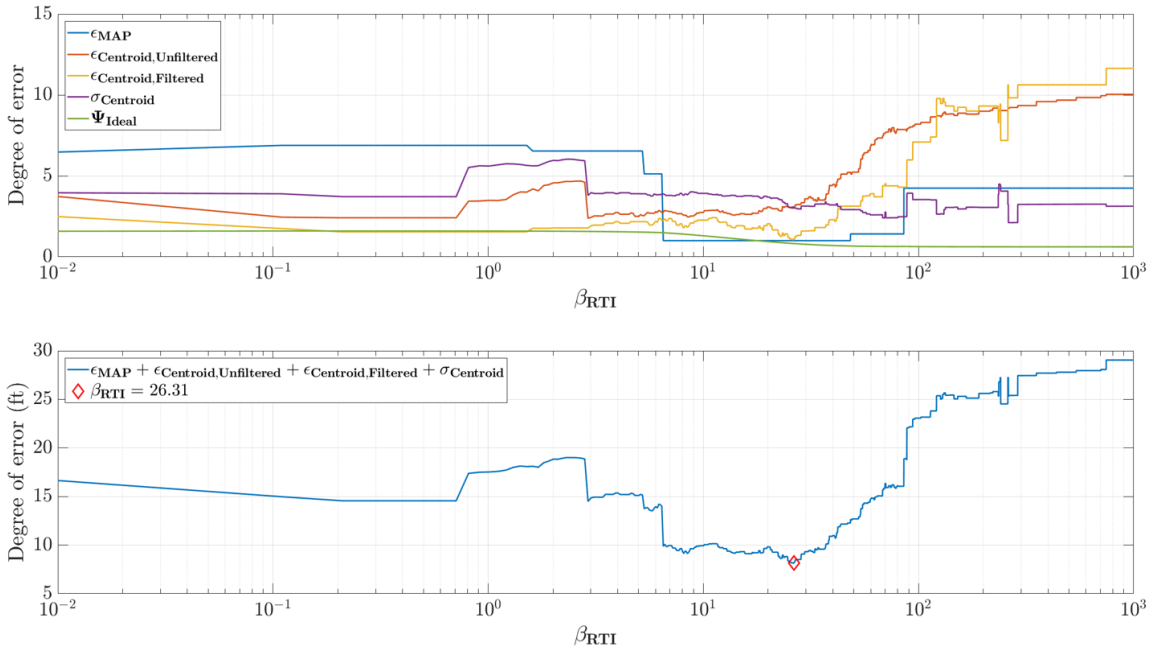

Figure 4.26. Top: Consolidated performance metrics across the three target location scenarios. Bottom: Summation of the appropriate performance metrics to determine β_{RTI}.

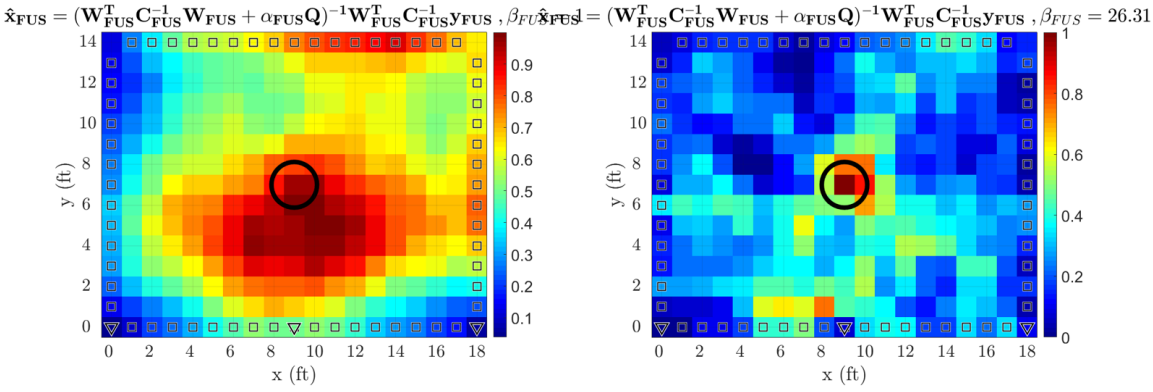

Figure 4.27. Left: $\alpha = 400, \beta_{\text{RTI}} = 1$, identical to Figure 4.25. Right: $\alpha = 400, \beta_{\text{RTI}} = 26.31$, subjectively chosen based on aesthetic.

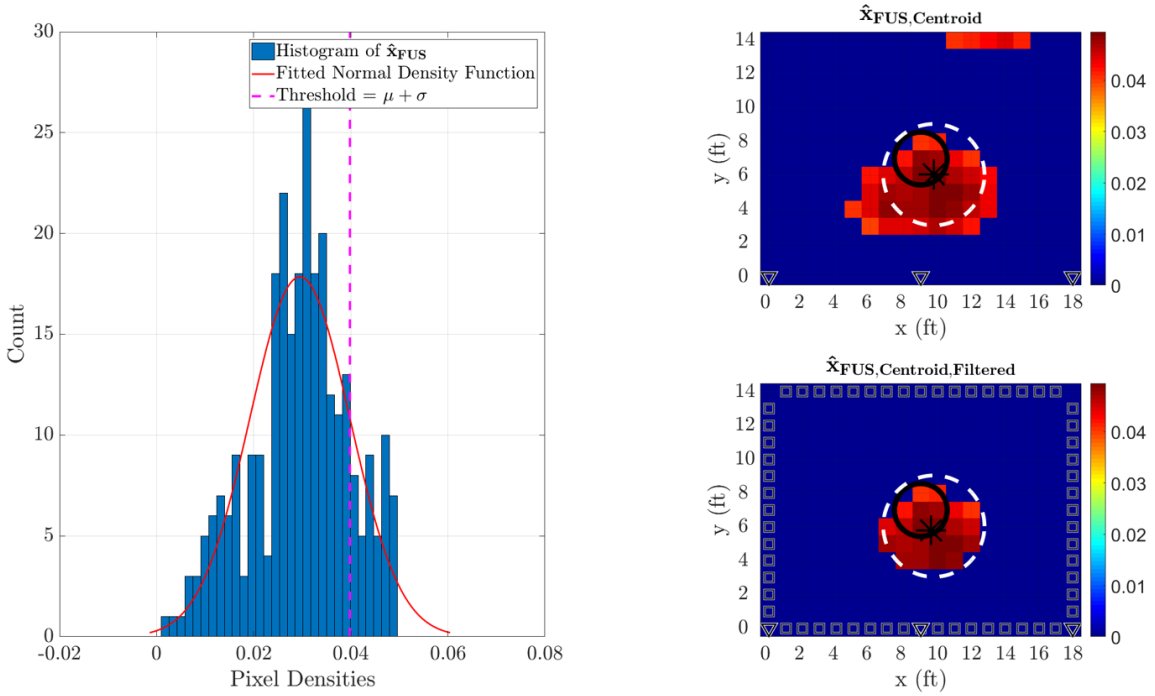

Figure 4.28. Left: Histogram of the pixel densities in $\hat{\mathbf{x}}_{\text{FUS}}$ from Figure 4.25. Right: Top - The resultant image from thresholding $\hat{\mathbf{x}}_{\text{FUS}}$ and the location of the centroid. Bottom - Filtering $\hat{\mathbf{x}}_{\text{FUS}}$ by keeping the pixels inside the circumference of the dotted circle and reapplying the k-means algorithm.

Table 4.7. Performance metrics for the MSDF Tikhonov regularized solution with targets at (9,7), (4,10) and (14,4).

Target Location	**Performance Metric**	**Description**	**Result**
(9,7)	MAP estimate	Coordinates of the most intense pixel.	(10,8) $\epsilon_{\text{MAP}} = 1.41$ ft
	K-means clustering	Coordinates of the centroid.	*Unfiltered* (9.77,6.05) $\epsilon_{\text{Centroid}} = 1.23$ ft
			Filtered (9.61,5.78) $\epsilon_{\text{Centroid,Filt}} = 1.36$ ft
	Dispersion	Pixel spread about the filtered centroid.	$\sigma_{\text{Centroid}} = 1.91$ ft
	Model solution	Compared to Figure 4.1.	$\Psi_{\text{Ideal}} = 0.62$
(4,10)	MAP estimate	Coordinates of the most intense pixel.	(6,14) $\epsilon_{\text{MAP}} = 4.47$ ft
	K-means clustering	Coordinates of the centroid.	*Unfiltered* (6.70,10.27) $\epsilon_{\text{Centroid}} = 1.40$ ft
			Filtered (4.79,10.11) $\epsilon_{\text{Centroid,Filt}} = 0.80$ ft
	Dispersion	Pixel spread about the filtered centroid.	$\sigma_{\text{Centroid}} = 1.77$ ft
	Model solution	Compared to Figure 4.1.	$\Psi_{\text{Ideal}} = 0.47$
(14,4)	MAP estimate	Coordinates of the most intense pixel.	(13,4) $\epsilon_{\text{MAP}} = 1$ ft
	K-means clustering	Coordinates of the centroid.	*Unfiltered* (13.17,4.48) $\epsilon_{\text{Centroid}} = 0.96$ ft
			Filtered (13.33,4.33) $\epsilon_{\text{Centroid,Filt}} = 0.80$ ft
	Dispersion	Pixel spread about the filtered centroid.	$\sigma_{\text{Centroid}} = 0.75$ ft
	Model solution	Compared to Figure 4.1.	$\Psi_{\text{Ideal}} = 0.50$

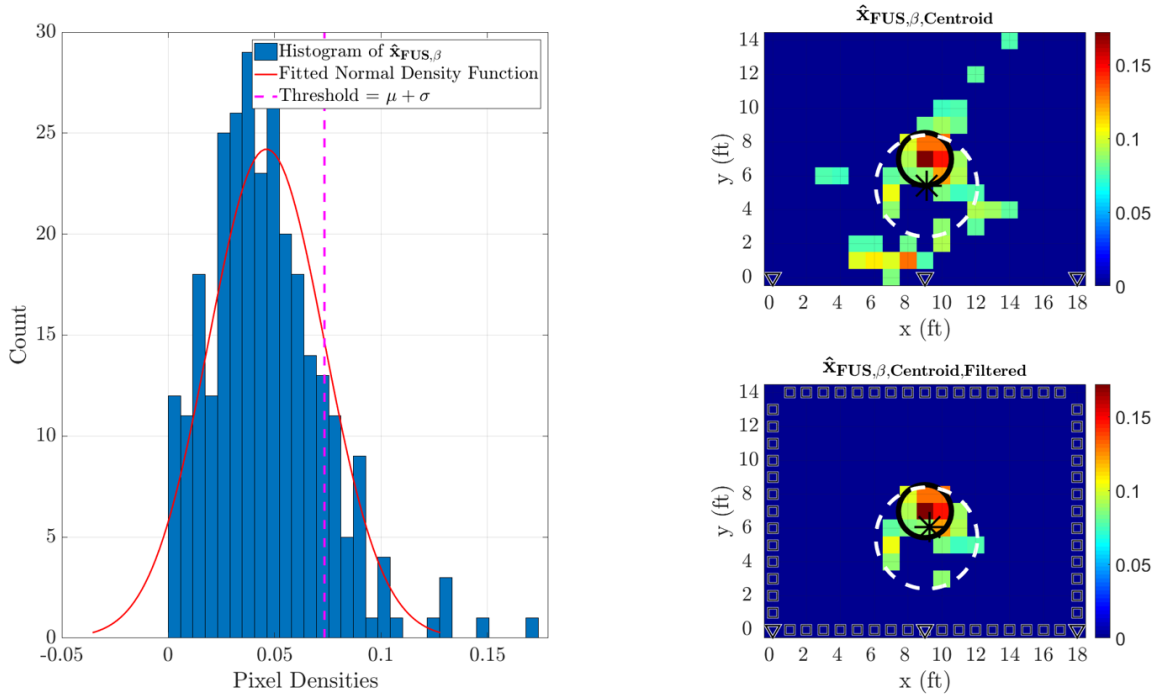

Figure 4.29. Left: Histogram of the pixel densities in $\hat{\mathbf{x}}_{\text{FUS},\beta}$ from the image on the right in Figure 4.27. Right: Top - The resultant image from thresholding $\hat{\mathbf{x}}_{\text{FUS},\beta}$ and the location of the centroid; Bottom - Filtering $\hat{\mathbf{x}}_{\text{FUS},\beta,\text{Centroid}}$ by keeping the pixels inside the circumference of the dotted circle and reapplying the k-means algorithm.

Table 4.8. Performance metrics for the MSDF Tikhonov regularized solution with targets at (9,7), (4,10) and (14,4). ($\beta_{\text{RTI}} = 21$)

Target Location	**Performance Metric**	**Description**	**Result**
(9,7)	MAP estimate	Coordinates of the most intense pixel.	(9,7) $\epsilon_{\text{MAP}} = 0$ ft
	K-means clustering	Coordinates of the centroid.	*Unfiltered* (9.10,5.41) $\epsilon_{\text{Centroid}} = 1.59$ ft
			Filtered (9.28,6.06) $\epsilon_{\text{Centroid,Filt}} = 0.98$ ft
	Dispersion	Pixel spread about the filtered centroid.	$\sigma_{\text{Centroid}} = 1.93$ ft
	Model solution	Compared to Figure 4.1.	$\Psi_{\text{Ideal}} = 0.30$
(4,10)	MAP estimate	Coordinates of the most intense pixel.	(4,10) $\epsilon_{\text{MAP}} = 0$ ft
	K-means clustering	Coordinates of the centroid.	*Unfiltered* (5.03,8.92) $\epsilon_{\text{Centroid}} = 1.49$ ft
			Filtered (4.36,9.50) $\epsilon_{\text{Centroid,Filt}} = 0.61$ ft
	Dispersion	Pixel spread about the filtered centroid.	$\sigma_{\text{Centroid}} = 1.53$ ft
	Model solution	Compared to Figure 4.1.	$\Psi_{\text{Ideal}} = 0.26$
(14,4)	MAP estimate	Coordinates of the most intense pixel.	(14,5) $\epsilon_{\text{MAP}} = 1$ ft
	K-means clustering	Coordinates of the centroid.	*Unfiltered* (12.39,4.05) $\epsilon_{\text{Centroid}} = 1.61$ ft
			Filtered (13.50,4.00) $\epsilon_{\text{Centroid,Filt}} = 0.50$ ft
	Dispersion	Pixel spread about the filtered centroid.	$\sigma_{\text{Centroid}} = 1.50$ ft
	Model solution	Compared to Figure 4.1.	$\Psi_{\text{Ideal}} = 0.27$

V. Conclusion & Future Work

A proof of concept for a Multi-Sensor Data Fusion (MSDF) technique using two disparate sensor technologies, namely Radio Tomographic Imaging (RTI) and a Noise Radar Network (NRN), has been presented in this thesis. The surveillance images delivered by the fusion of these sensors is intended to be of greater accuracy and reliability versus operating the sensors independently. To reiterate the motivation for this research, in accordance with Royal Australian Air Force (RAAF) doctrine, the fundamental principles by which military forces guide their actions to achieve desired objectives, situational understanding is the awareness, analysis, knowledge, comprehension and judgment facilitating and enabling timely and accurate decision-making.

Various solutions for the surveillance image, $\hat{\mathbf{x}}$, were created in order to evaluate its quality. Solutions for $\hat{\mathbf{x}}$ are organized in Table 5.1. A summary of the performance metrics for each solution of $\hat{\mathbf{x}}$ are displayed accordingly in Table 5.2. It can be concluded from the performance metrics of Table 5.2 that out of all the Tikhonov influenced images, it is the MSDF solution of $\hat{\mathbf{x}}_{\text{FUS},\beta_{\text{RTI}}}$ that ranks first when considering all of the performance metrics and the three cases for target location. The best case for $\hat{\mathbf{x}}_{\text{FUS},\beta_{\text{RTI}}}$ was for target location (4,10), Figure A.8, where the performance metrics reveal up to a 100% error decrease in target pixel location (ϵ_{MAP}), a 75% error decrease in target centroid location ($\epsilon_{\text{Centroid}}$), a 28% size decrease in target pixel dispersion (σ_{Centroid}) and a 72% improvement in an ideal solution comparison (Ψ_{Ideal}).

Ultimately, the results of the research presented in this thesis prove that MSDF images are of greater quality than that of the images generated by the disparate sensors independently, $\hat{\mathbf{x}}_{\text{RTI}}$ and $\hat{\mathbf{x}}_{\text{NRN}}$. Follow on work that can develop the state of MSDF with RTI and a NRN include

- Explore a bistatic/multistatic configuration of the AFIT NoNET versus the mono-

Table 5.1. A summary of the various solutions for $\hat{\mathbf{x}}$.

Solution	Description	(9,7)	(4,10)	(14,4)
		Figure Reference No.		
$\hat{\mathbf{x}}_{\text{RTI}}$	The RTI Tikhonov regularized solution	4.4	A.2	B.2
$\hat{\mathbf{x}}_{\text{NRN,Trilateration}}$	The Air Force Institute of Technology (AFIT) Noise Network (NoNET) trilateration solution	4.12	A.3	B.3
$\hat{\mathbf{x}}_{\text{NRN,Tikhonov}}$	The AFIT NoNET Tikhonov regularized solution	4.16	A.4	B.4
$\hat{\mathbf{x}}_{\text{Avg}}$	A MSDF image created by averaging $\hat{\mathbf{x}}_{\text{RTI}}$ and $\hat{\mathbf{x}}_{\text{NRN,Tikhonov}}$	4.21	A.5	B.5
$\hat{\mathbf{x}}_{\text{KAL}}$	A MSDF image created by Kalman filtering $\hat{\mathbf{x}}_{\text{RTI}}$ and $\hat{\mathbf{x}}_{\text{NRN,Tikhonov}}$	4.22	A.6	B.6
$\hat{\mathbf{x}}_{\text{FUS}}$	A MSDF Tikhonov regularized solution	4.25	A.7	B.7
$\hat{\mathbf{x}}_{\text{FUS},\beta_{\text{RTI}}}$	A MSDF Tikhonov regularized solution with an additional parameter β_{RTI}	4.27	A.8	B.8

static configuration.

- Investigations into the use of different weight models with RTI on accuracy and performance of the final MSDF image.
- Incorporation of antenna pattern in the noise radar weighting matrix, $\mathbf{W}_{\text{NR}z}$.
- Exploration of the best tuning parameters α and β in the MSDF Tihkonov algorithm.
- Real time MSDF implementation of multiple target tracking (MTT).
- Number and sensor placement analysis of RTI and/or NRN nodes.
- Employing two receive antennas into the configuration of an AFIT NoNET node to introduce angular samples in collected radar data.

Table 5.2. A summary of performance metrics for the various solutions for $\hat{\mathbf{x}}$ with target at (9,7), (4,10) and (14,4).

Target Location	Solution	Performance Metric				
		ϵ_{MAP}	$\epsilon_{\text{Centroid,Unfiltered}}$	$\epsilon_{\text{Centroid,Filtered}}$	σ_{Centroid}	Ψ_{Ideal}
(9,7)	$\hat{\mathbf{x}}_{\text{RTI}}$	0 ft	0.83 ft	0.83 ft	2.09 ft	0.53
	$\hat{\mathbf{x}}_{\text{NRN,Trilateration}}$	1 ft	1.32 ft	1.48 ft	1.73 ft	0.47
	$\hat{\mathbf{x}}_{\text{NRN,Tikhonov}}$	1 ft	0.15 ft	0.57 ft	1.81 ft	0.35
	$\hat{\mathbf{x}}_{\text{Avg}}$	0 ft	0.49 ft	0.39 ft	1.90 ft	0.45
	$\hat{\mathbf{x}}_{\text{KAL}}$	0 ft	1.06 ft	0.93 ft	2.08 ft	0.50
	$\hat{\mathbf{x}}_{\text{FUS}}$	1.41 ft	1.23 ft	1.36 ft	1.91 ft	0.62
	$\hat{\mathbf{x}}_{\text{FUS},\beta_{\text{RTI}}}$	0 ft	1.59 ft	0.98 ft	1.93 ft	0.30
(4,10)	$\hat{\mathbf{x}}_{\text{RTI}}$	0 ft	1.88 ft	1.77 ft	2.12 ft	0.92
	$\hat{\mathbf{x}}_{\text{NRN,Trilateration}}$	3.16 ft	2.00 ft	1.88 ft	1.85 ft	0.13
	$\hat{\mathbf{x}}_{\text{NRN,Tikhonov}}$	2 ft	2.72 ft	2.40 ft	1.93 ft	0.30
	$\hat{\mathbf{x}}_{\text{Avg}}$	2 ft	1.33 ft	1.49 ft	2.00 ft	0.42
	$\hat{\mathbf{x}}_{\text{KAL}}$	1 ft	0.96 ft	0.93 ft	2.05 ft	0.47
	$\hat{\mathbf{x}}_{\text{FUS}}$	4.47 ft	1.40 ft	0.80 ft	1.77 ft	0.47
	$\hat{\mathbf{x}}_{\text{FUS},\beta_{\text{RTI}}}$	0 ft	1.49 ft	0.61 ft	1.53 ft	0.26
(14,4)	$\hat{\mathbf{x}}_{\text{RTI}}$	1 ft	1.19 ft	1.27 ft	1.99 ft	0.99
	$\hat{\mathbf{x}}_{\text{NRN,Trilateration}}$	0 ft	0.26 ft	0.75 ft	1.78 ft	0.13
	$\hat{\mathbf{x}}_{\text{NRN,Tikhonov}}$	2.24 ft	0.94 ft	0.59 ft	2.00 ft	0.24
	$\hat{\mathbf{x}}_{\text{Avg}}$	1 ft	0.89 ft	0.83 ft	2.09 ft	0.35
	$\hat{\mathbf{x}}_{\text{KAL}}$	1 ft	1.39 ft	1.44 ft	2.07 ft	0.44
	$\hat{\mathbf{x}}_{\text{FUS}}$	1 ft	0.96 ft	0.80 ft	0.75 ft	0.50
	$\hat{\mathbf{x}}_{\text{FUS},\beta_{\text{RTI}}}$	1 ft	1.61 ft	0.50 ft	1.50 ft	0.27
Average across Target Locations						
	$\hat{\mathbf{x}}_{\text{RTI}}$	0.33 ft	1.30 ft	1.29 ft	2.07 ft	0.81
	$\hat{\mathbf{x}}_{\text{NRN,Trilateration}}$	1.39 ft	1.93 ft	1.37 ft	1.79 ft	0.24
	$\hat{\mathbf{x}}_{\text{NRN,Tikhonov}}$	1.75 ft	1.27 ft	1.19 ft	1.91 ft	0.30
	$\hat{\mathbf{x}}_{\text{Avg}}$	1 ft	0.90 ft	0.90 ft	2.00 ft	0.35
	$\hat{\mathbf{x}}_{\text{KAL}}$	0.67 ft	1.14 ft	1.10 ft	2.06 ft	0.47
	$\hat{\mathbf{x}}_{\text{FUS}}$	2.29 ft	1.20 ft	0.99 ft	1.48 ft	0.53
	$\hat{\mathbf{x}}_{\text{FUS},\beta_{\text{RTI}}}$	0.33 ft	1.56 ft	0.70 ft	1.65 ft	0.28

Appendix A. Figures with target at (4,10)

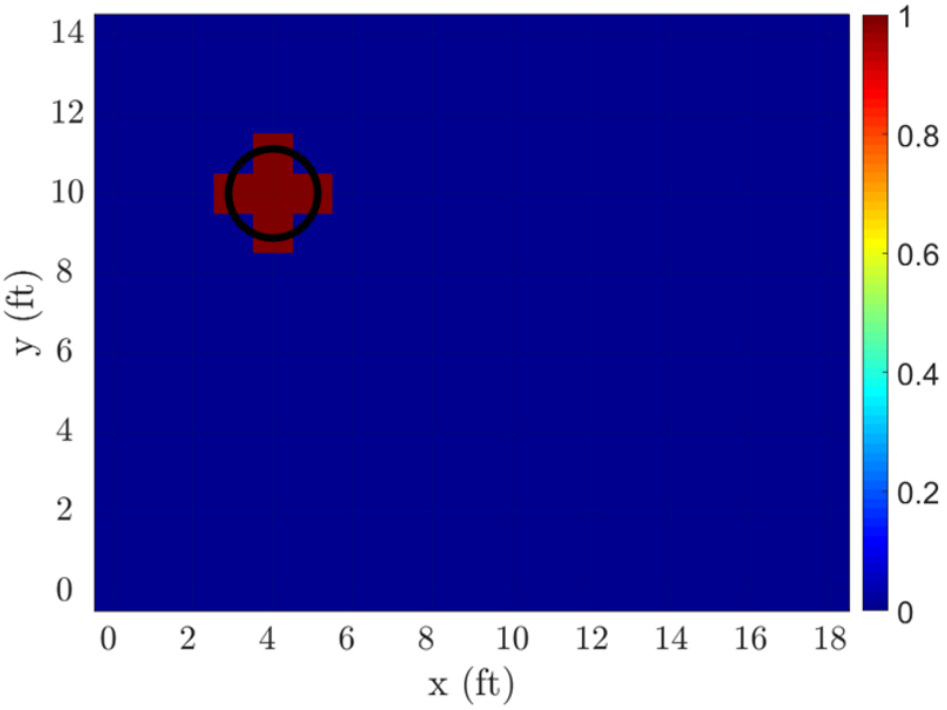

Figure A.1. A model solution to be used for the performance metric, Ψ_{Ideal}, with target at (4,10).

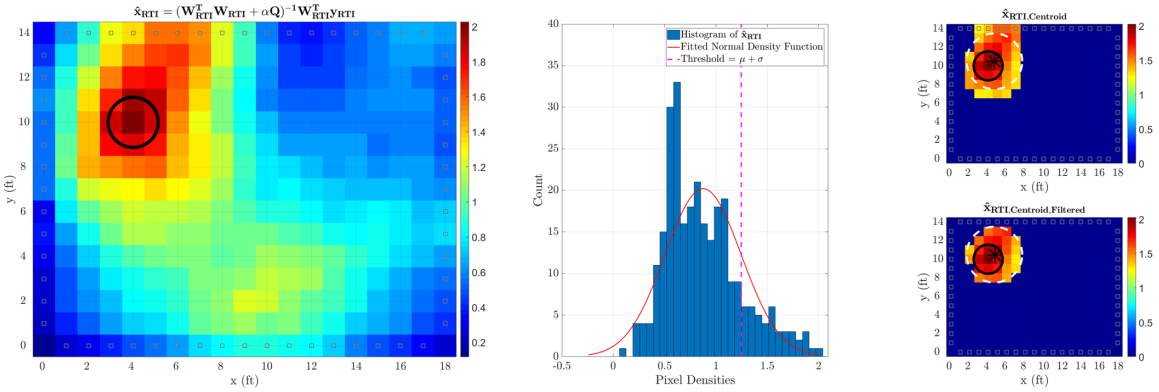

Figure A.2. The AFIT RTI image with target at coordinate (4,10). The regularization parameter α has subjectively been set to 8. Unfiltered and filtered centroid locations are also shown

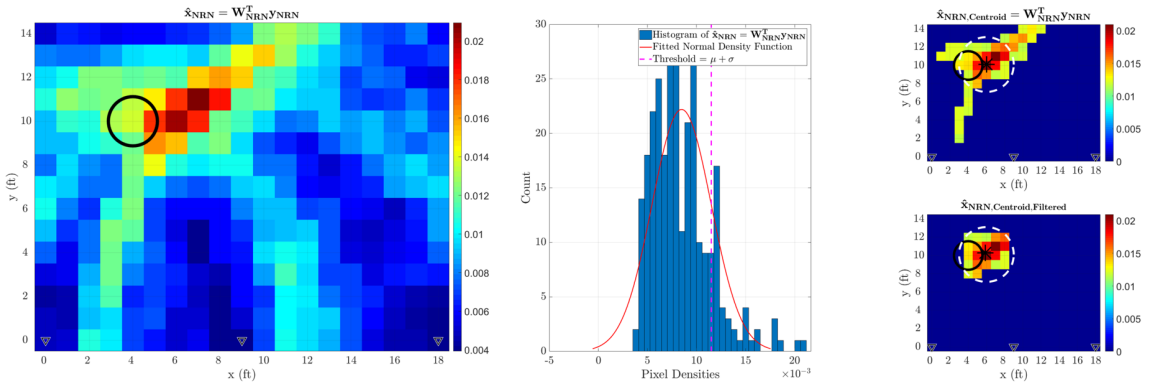

Figure A.3. NRN transmitting/receiving from coordinates (0,0), (9,0) and (18,0) with target at coordinate (4,10). Unfiltered and filtered centroids are also shown.

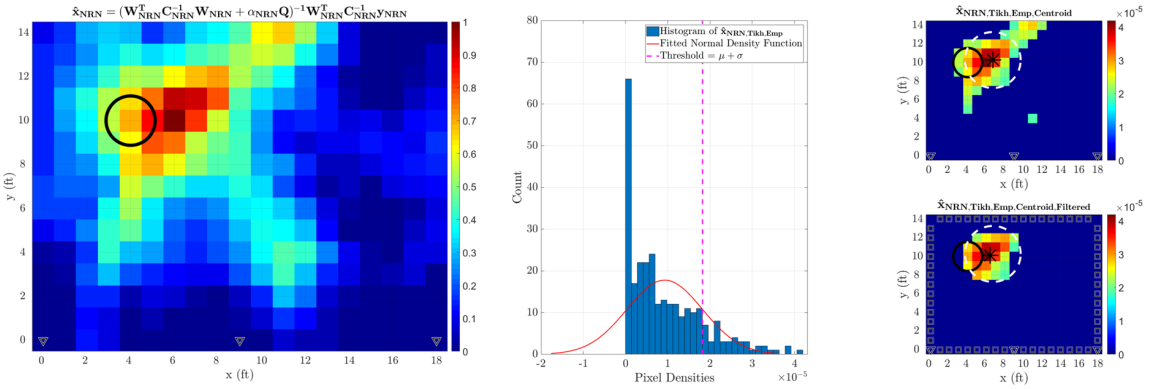

Figure A.4. NRN transmitting/receiving from coordinates (0,0), (9,0) and (18,0) with target at coordinate (4,10). The regularization parameter α has subjectively been set to 200. Unfiltered and filtered centroids are also shown.

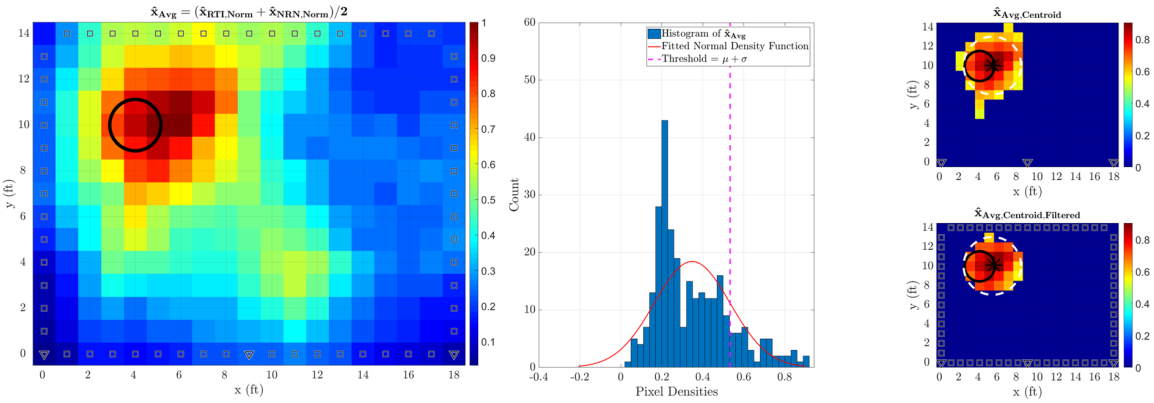

Figure A.5. Taking the average of the Tikhonov solutions from the RTI and the AFIT NoNET sensors. Unfiltered and filtered centroid locations are also shown.

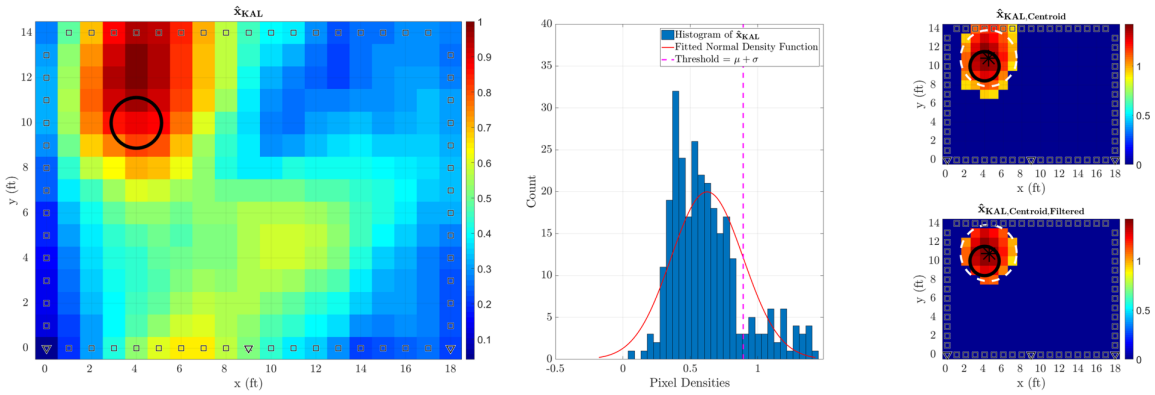

Figure A.6. Taking the pixel densities of the Tikhonov solutions from the RTI and the AFIT NoNET sensors and applying a Kalman filter to them using state-vector fusion. Unfiltered and filtered centroid locations are shown.

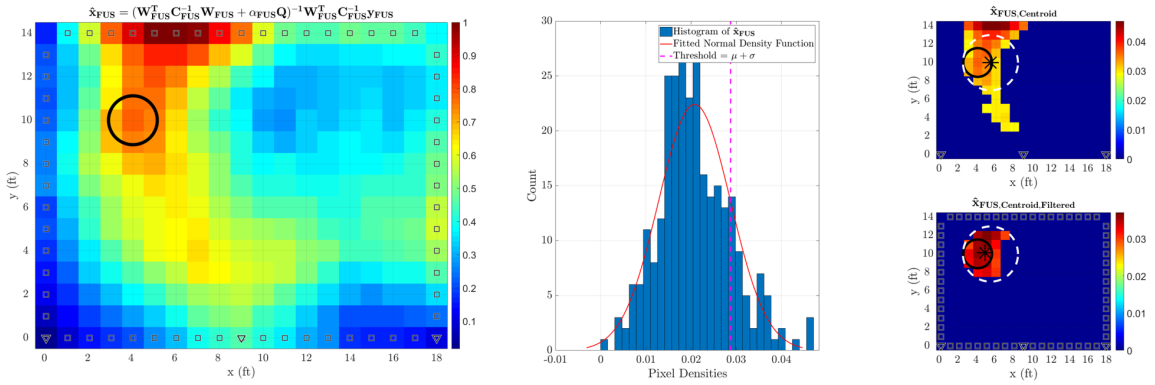

Figure A.7. A MSDF image with a target at coordinate (4,10). The Tikhonov regularization parameter, $\alpha = 400$, was subjectively chosen based on aesthetic. Unfiltered and filtered centroid locations are also shown.

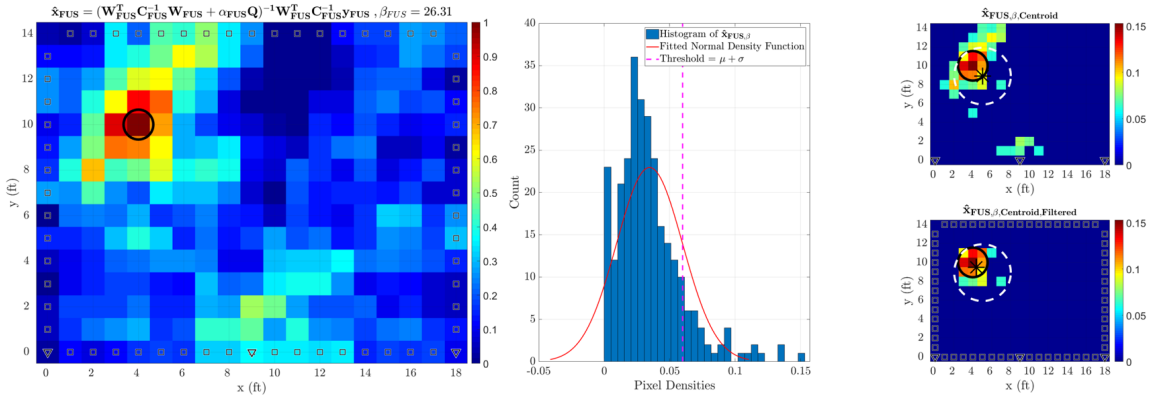

Figure A.8. $\beta_{\text{RTI}} = 26.31$. Unfiltered and filtered centroid locations are also shown.

Appendix B. Figures with target at (14,4)

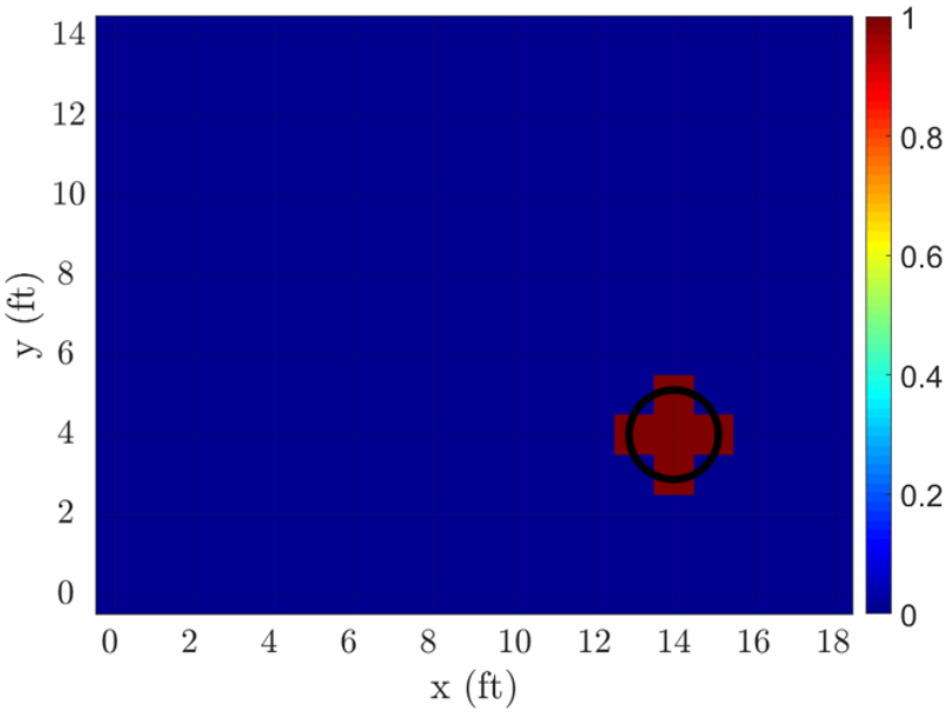

Figure B.1. A model solution to be used for the performance metric, Ψ_{Ideal}, with target at (14,4).

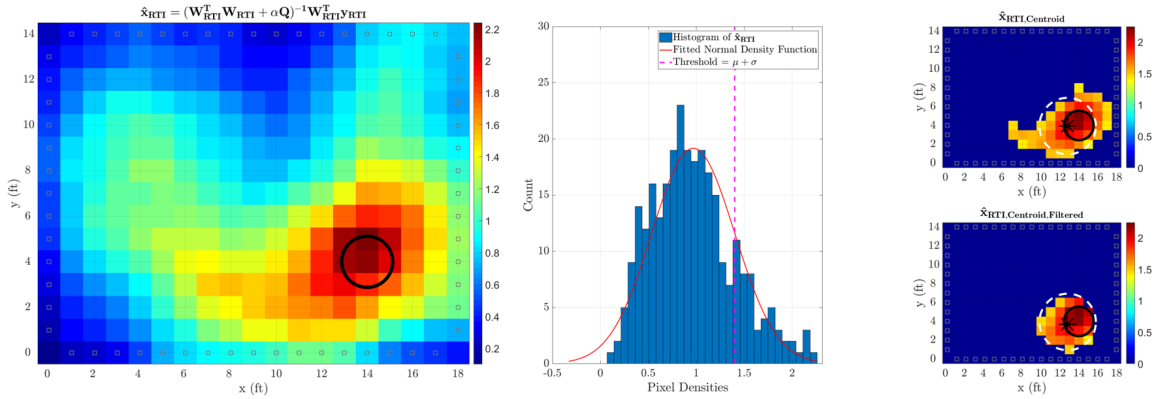

Figure B.2. The AFIT RTI image with target at coordinate (14,4). The regularization parameter α has subjectively been set to 8. Unfiltered and filtered centroids are also shown.

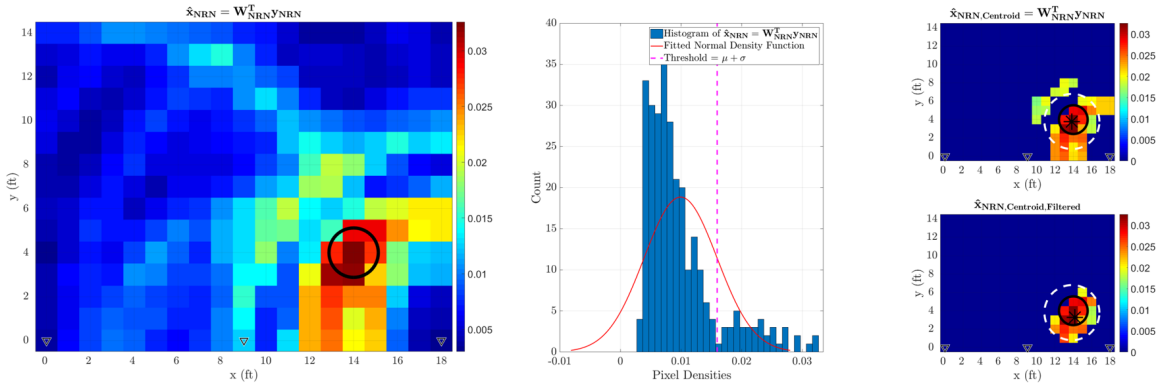

Figure B.3. NRN transmitting/receiving from coordinates (0,0), (9,0) and (18,0) with target at coordinate (14,4). Unfiltered and filtered centroids are also shown.

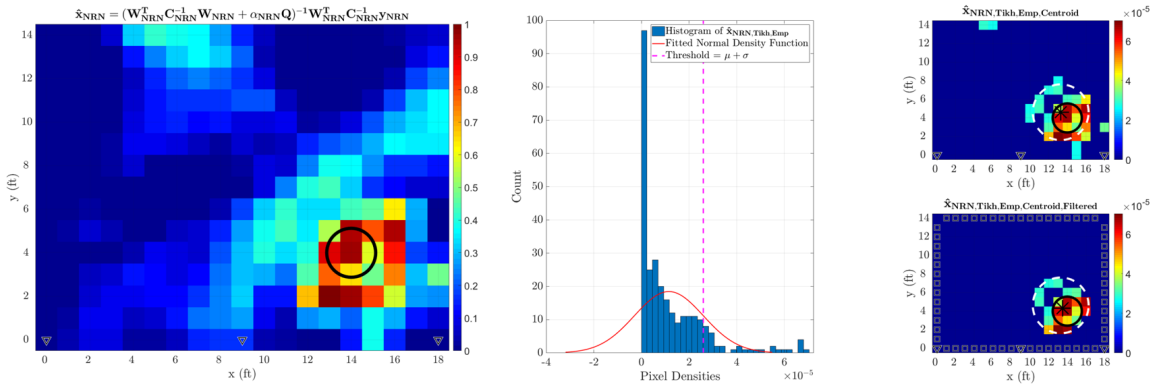

Figure B.4. NRN transmitting/receiving from coordinates (0,0), (9,0) and (18,0) with target at coordinate (14,4). The regularization parameter α has subjectively been set to 200. Unfiltered and filtered centroids are also shown.

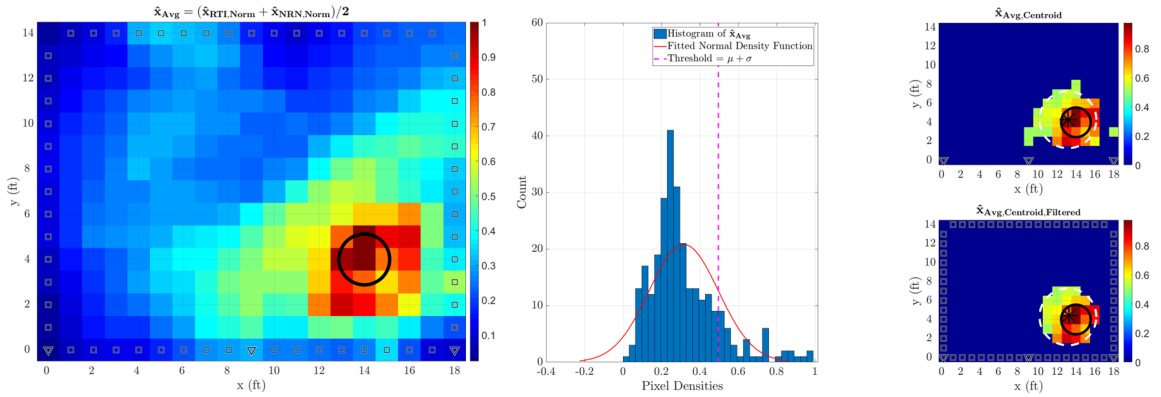

Figure B.5. Taking the average of the Tikhonov solutions from the RTI and the AFIT NoNET sensors. Unfiltered and filtered centroid locations are also shown.

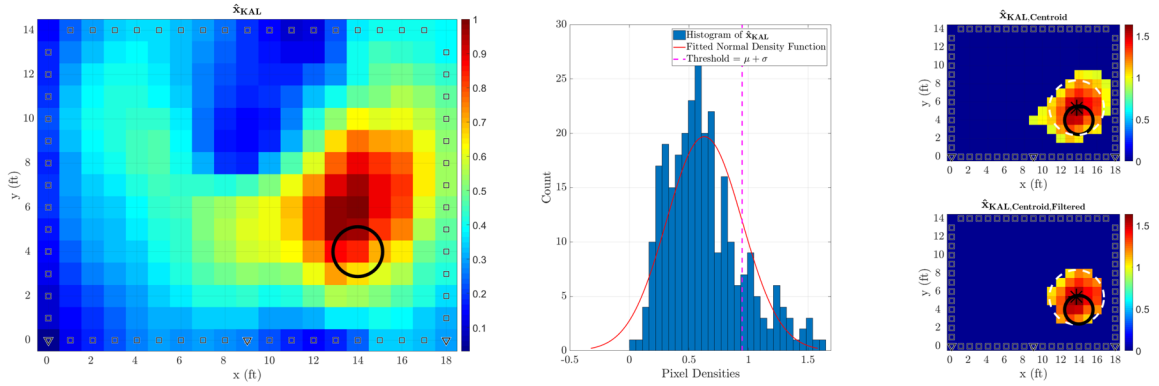

Figure B.6. Taking the pixel densities of the Tikhonov solutions from the RTI and the AFIT NoNET sensors and applying a Kalman filter to them using state-vector fusion. Unfiltered and filtered centroid locations are shown.

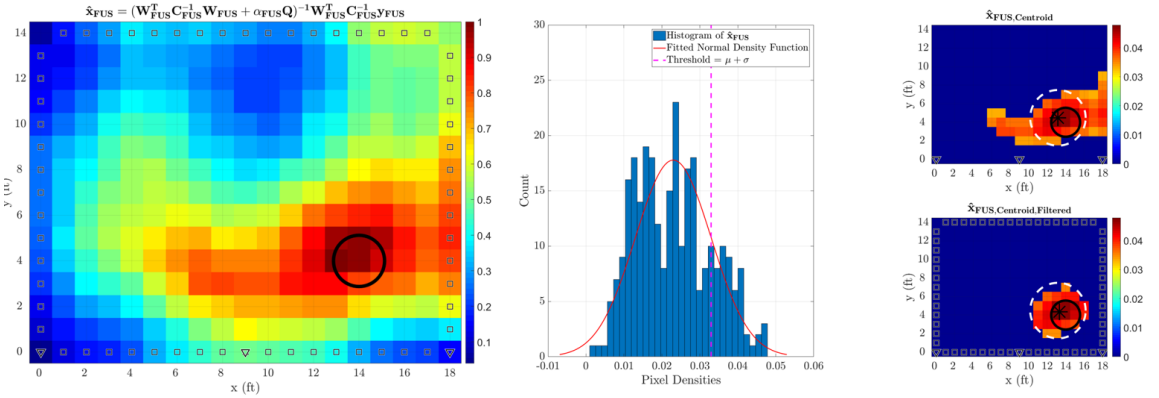

Figure B.7. A MSDF image with a target at coordinate (14,4). The Tikhonov regularization parameter, $\alpha = 400$, was subjectively chosen based on aesthetic. Unfiltered and filtered centroid locations are also shown.

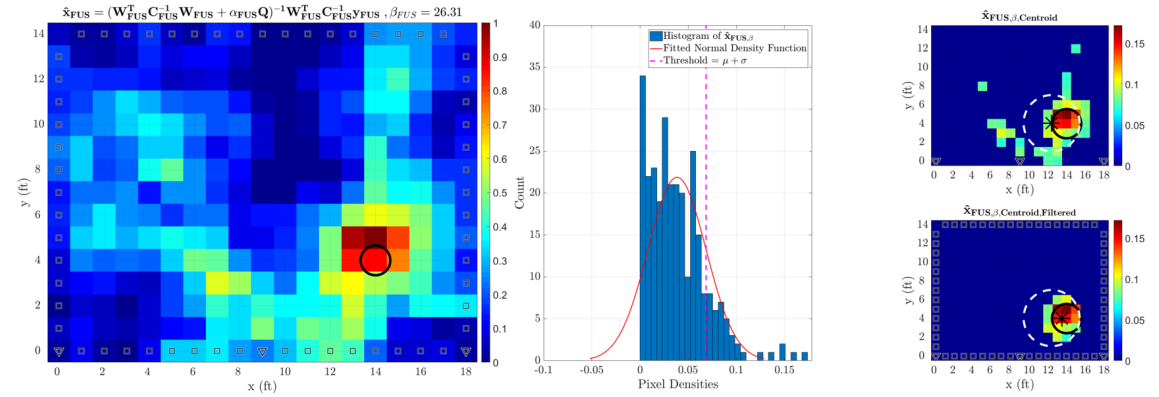

Figure B.8. $\beta_{\text{RTI}} = 26.31$. Unfiltered and filtered centroid locations are also shown.

Bibliography

1. N. Patwari and J. Wilson, "RF sensor networks for device-free localization: Measurements, models, and algorithms," *Proceedings of the IEEE*, vol. 98, pp. 1961–1973, Jul 2010.

2. S. Nannuru, Y. Li, Y. Zeng, M. Coates, and B. Yang, "Radio-frequency tomography for passive indoor multitarget tracking," *IEEE Transactions on Mobile Computing*, vol. 12, pp. 2322–2333, Sep 2012.

3. J. Wilson and N. Patwari, "See-through walls: Motion tracking using variance-based radio tomography networks," *IEEE Transactions on Mobile Computing*, vol. 10, pp. 612–621, May 2011.

4. R. S. Kshetrimayum, "An introduction to UWB communication systems," *IEEE Potentials*, vol. 28, pp. 9–13, Mar 2009.

5. J. D. Taylor, *Introduction to ultra-wideband radar systems*. CRC press, 1994.

6. R. M. Narayanan, "Through-wall radar imaging using UWB noise waveforms," *Journal of the Franklin Institute*, vol. 345, pp. 659–678, Sep 2008.

7. C. Alippi, M. Bocca, G. Boracchi, N. Patwari, and M. Roveri, "RTI goes wild: Radio tomographic imaging for outdoor people detection and localization," *IEEE Transactions on Mobile Computing*, vol. 15, pp. 2585–2598, Oct 2016.

8. R. Narayanan, X. Xu, and J. Henning, "Radar penetration imaging using ultra-wideband (UWB) random noise waveforms," *IEE Proceedings-Radar, Sonar and Navigation*, vol. 151, pp. 143–148, Jun 2004.

9. J. Wilson and N. Patwari, "Radio tomographic imaging with wireless networks," *IEEE Transactions on Mobile Computing*, vol. 9, pp. 621–632, May 2010.

10. R. K. Martin, C. Anderson, R. W. Thomas, and A. S. King, "Modelling and analysis of radio tomography," in *2011 4th IEEE International Workshop on Computational Advances in Multi-Sensor Adaptive Processing (CAMSAP)*, pp. 377–380, Dec 2011.

11. R. K. Martin, A. Folkerts, and T. Heinl, "Accuracy vs. resolution in radio tomography," *IEEE Transactions on Signal Processing*, vol. 62, pp. 2480–2491, May 2014.

12. P. Agrawal and N. Patwari, "Correlated link shadow fading in multi-hop wireless networks," *IEEE Transactions on Wireless Communications*, vol. 8, pp. 4024–4036, Aug 2009.

13. R. Bultitude, "Measurement, characterization and modeling of indoor 800/900 MHz radio channels for digital communications," *IEEE communications magazine*, vol. 25, pp. 5–12, Jun 1987.

14. R. Ganesh and K. Pahlavan, "Effects of traffic and local movements on multipath characteristics of an indoor radio channel," *Electronics Letters*, vol. 26, pp. 810–812, Jun 1990.

15. M. A. Richards, J. Scheer, W. A. Holm, and W. L. Melvin, *Principles of modern radar*. SciTech Publishing, Inc, 2010.

16. A. Farina and E. Hanle, "Position accuracy in netted monostatic and bistatic radar," *IEEE Transactions on Aerospace and Electronic Systems*, pp. 513–520, Jul 1983.

17. A. L. Schmitt, "Radar imaging with a network of digital noise radar systems," Master's thesis, Air Force Institute of Technology, Mar 2009.

18. M. E. Nelms, "Development and Evaluation of a Multistatic Ultrawideband Random Noise Radar," Master's thesis, Air Force Institute of Technology, Mar 2010.

19. J. R. Lievsay, "Simultaneous Range/Velocity Detection with an Ultra-Wideband Random Noise Radar Through Fully Digital Cross-Correlation in the Time Domain," Master's thesis, Air Force Institute of Technology, Mar 2011.

20. Q. Gan and C. J. Harris, "Comparison of two measurement fusion methods for kalman-filter-based multisensor data fusion," *IEEE Transactions on Aerospace and Electronic systems*, vol. 37, pp. 273–279, Jan 2001.

21. Y. Gao, W.-J. Jia, X.-J. Sun, and Z.-L. Deng, "Self-tuning multisensor weighted measurement fusion kalman filter," *IEEE Transactions on Aerospace and Electronic Systems*, vol. 45, pp. 179–191, Jan 2009.

22. J. Roecker and C. McGillem, "Comparison of two-sensor tracking methods based on state vector fusion and measurement fusion," *IEEE Transactions on Aerospace and Electronic Systems*, vol. 24, pp. 447–449, Jul 1988.

23. K. C. Chang, T. Zhi, and R. K. Saha, "Performance evaluation of track fusion with information matrix filter," *IEEE Transactions on Aerospace and Electronic Systems*, vol. 38, pp. 455–466, Apr 2002.

24. Y. Bar-Shalom and L. Campo, "The effect of the common process noise on the two-sensor fused-track covariance," *IEEE Transactions on Aerospace and Electronic Systems*, pp. 803–805, Nov 1986.

25. K.-C. Chang, R. K. Saha, and Y. Bar-Shalom, "On optimal track-to-track fusion," *IEEE Transactions on Aerospace and Electronic Systems*, vol. 33, pp. 1271–1276, Oct 1997.

26. E. Foxlin, "Inertial head-tracker sensor fusion by a complementary separate-bias kalman filter," in *Proceedings of the IEEE 1996 Virtual Reality Annual International Symposium*, pp. 185–194, Apr 1996.

27. L. Jetto, S. Longhi, and G. Venturini, "Development and experimental validation of an adaptive extended kalman filter for the localization of mobile robots," *IEEE Transactions on Robotics and Automation*, vol. 15, pp. 219–229, May 1999.

28. T. S. Danella, "Identifying High-Traffic Patterns In The Workplace With Radio Tomographic Imaging in 3D Wireless Sensor Networks," Master's thesis, Air Force Institute of Technology, Mar 2014.

29. A. R. Gallagher, "Radio Tomographic Imaging Using a Modified Maximum Likelihood Estimator for Image Reconstruction in Various Environments," Master's thesis, Air Force Institute of Technology, Mar 2018.

30. T. Instruments, "2.4-GHz Inverted F Antenna." http://www.ti.com/lit/pdf/swru120, 2017. [Online; accessed 17-November-2018].

31. T. Instruments, "2.4 GHz IEEE 802.15.4 / ZigBee-Ready RF Transceiver datasheet (Rev. C)." http://www.ti.com/lit/gpn/cc2420, 2013. [Online; accessed 17-November-2018].

32. J. T. Thorson, "Simultaneous Range and Doppler Processing and Signal-to-Noise Ratio Analysis of the AFIT Random Noise Radar," Master's thesis, Air Force Institute of Technology, Mar 2012.

33. J. A. Hardin, "Information Encoding on a Pseudo Random Noise Radar Waveform," Master's thesis, Air Force Institute of Technology, Mar 2013.

34. A. T. Myers, "The Miniaturization of the AFIT Random Noise Radar," Master's thesis, Air Force Institute of Technology, Mar 2013.

35. R. D. Wilson, "Adaptations and Analysis of the AFIT Noise Radar Network for Indoor Navigation," Master's thesis, Air Force Institute of Technology, Mar 2013.

36. J. R. B. Cruz, "Comparison of Image Processing Techniques using Random Noise Radar," Master's thesis, Air Force Institute of Technology, Mar 2014.

37. B. Earl, "Two Point Calibration." https://learn.adafruit.com/calibrating-sensors/two-point-calibration, 2018. [Online; accessed 20-November-2018].

38. N. Patwari, A. O. Hero, M. Perkins, N. S. Correal, and R. J. O'dea, "Relative location estimation in wireless sensor networks," *IEEE Transactions on Signal Processing*, vol. 51, pp. 2137–2148, Aug 2003.

39. J. K. Nishida, "Estimating Single and Multiple Target Locations using K-means Clustering with Radio Tomographic Imaging in Wireless Sensor Networks," Master's thesis, Air Force Institute of Technology, Mar 2015.

40. M. Bocca, O. Kaltiokallio, N. Patwari, and S. Venkatasubramanian, "Multiple target tracking with RF sensor networks," *IEEE Transactions on Mobile Computing*, pp. 1787–1800, Aug 2013.

41. M. Andersson, J. Rydell, L. St-Laurent, D. Prévost, and F. Gustafsson, "Crowd analysis with target tracking, k-means clustering and hidden markov models," in *2012 15th International Conference on Information Fusion (FUSION)*, pp. 1903–1910, IEEE, Jul 2012.

42. C. Zhang and S. Xia, "K-means clustering algorithm with improved initial center," in *2009 Second International Workshop on Knowledge Discovery and Data Mining*, pp. 790–792, IEEE, Jan 2009.

43. S. Lloyd, "Least squares quantization in PCM," *IEEE transactions on information theory*, vol. 28, pp. 129–137, Mar 1982.

44. Fathima Shareena K.P., "An efficient approach for multi-target tracking in sensor networks using ant colony optimization," *International Journal for Scientific Research and Development*, vol. 1, Mar 2013.

45. D. Arthur and S. Vassilvitskii, "k-means++: The advantages of careful seeding," in *Proceedings of the eighteenth annual ACM-SIAM symposium on Discrete algorithms*, pp. 1027–1035, Society for Industrial and Applied Mathematics, Nov 2007.

REPORT DOCUMENTATION PAGE

Form Approved
OMB No. 0704–0188

1. REPORT DATE *(DD–MM–YYYY)*	2. REPORT TYPE	3. DATES COVERED *(From — To)*
21–03–2019	Master's Thesis	Sept 2017 — Mar 2019

4. TITLE AND SUBTITLE

Multi-Sensor Data Fusion between Radio Tomographic Imaging and Noise Radar.

5a. CONTRACT NUMBER

5b. GRANT NUMBER

5c. PROGRAM ELEMENT NUMBER

6. AUTHOR(S)

Vergara, Christopher, FLTLT, RAAF

5d. PROJECT NUMBER

5e. TASK NUMBER

5f. WORK UNIT NUMBER

7. PERFORMING ORGANIZATION NAME(S) AND ADDRESS(ES)

Air Force Institute of Technology
Graduate School of Engineering and Management (AFIT/EN)
2950 Hobson Way
WPAFB OH 45433-7765

8. PERFORMING ORGANIZATION REPORT NUMBER

AFIT-ENG-MS-19-M-064

9. SPONSORING / MONITORING AGENCY NAME(S) AND ADDRESS(ES)

Intentionally Left Blank

10. SPONSOR/MONITOR'S ACRONYM(S)

11. SPONSOR/MONITOR'S REPORT NUMBER(S)

12. DISTRIBUTION / AVAILABILITY STATEMENT

Distribution Statement A.
Approved for Public Release; Distribution Unlimited.

13. SUPPLEMENTARY NOTES

14. ABSTRACT

Radio Tomographic Imaging (RTI) and noise radar are two proven surveillance technologies. The novelty of fusing data from RTI and noise radar is achieved with the derivation of a fusion technique utilizing Tikhonov regularization. Analyzing the results of the Tikhonov influenced techniques reveals up to a 100% error decrease in target pixel location, a 75% error decrease in target centroid location, a 28% size decrease in target pixel dispersion and a 72% improvement in an ideal solution comparison. Results provide the RTI and noise radar communities a proof of concept for the fusion of data from two disparate sensor technologies.

15. SUBJECT TERMS

Data Fusion, Radio Tomographic Imaging, Noise Radar

16. SECURITY CLASSIFICATION OF:			17. LIMITATION OF ABSTRACT	18. NUMBER OF PAGES	19a. NAME OF RESPONSIBLE PERSON
a. REPORT	b. ABSTRACT	c. THIS PAGE			Dr. R. K. Martin, AFIT/ENG
U	U	U	UU	130	19b. TELEPHONE NUMBER *(include area code)* (937) 255-3636, x4625; richard.martin@afit.edu